

Espen Hovland

Optimization and Fabrication of Multiplexed Mach-Zehnder Interferometer-Assisted Ring Resonator Configuration (MARC) Photonic Sensors

Master's thesis in Nanotechnology

Supervisor: Astrid Aksnes

June 2022

Espen Hovland

Optimization and Fabrication of Multiplexed Mach-Zehnder Interferometer-Assisted Ring Resonator Configuration (MARC) Photonic Sensors

Master's thesis in Nanotechnology
Supervisor: Astrid Aksnes
June 2022

Norwegian University of Science and Technology
Faculty of Information Technology and Electrical Engineering
Department of Electronic Systems

Problem Description

The silicon-on-insulator (SOI)-platform, due to its large refractive index contrast, allows for highly compact photonic integrated circuits (PICs). These circuits in turn enable the implementation of sensitive photonic sensors, suitable for lab-on-chip (LOC) applications. One example of such a photonic sensor, is the Mach-Zehnder interferometer-assisted ring resonator configuration (MARC) photonic sensor. MARC sensors consist of a ring resonator coupled with a Mach-Zehnder interferometer, which allows for greatly increased dynamic measurement range combined with a unique optical transmission response.

In this master's project, multiple MARC sensors will be designed and simulated using the finite-elements method (FEM)-based COMSOL Multiphysics 5.4 / 6.0 (COMSOL), with the aim of creating a single, *multiplexed* MARC sensor. The main focus is the device design and simulations, however the finalized design will be realized through fabrication at NTNU NanoLab in the later stages of the thesis work, in order to verify the feasibility of the simulated design.

The simulations will focus on creating a compact MARC device that is able to multiplex three different signals, while still allowing for precise measurements and simple de-multiplexing of the constituent signals. Once the design is finalized, the device will be realized using fabrication techniques such as plasma-enhanced chemical vapor deposition (PECVD), electron beam lithography (EBL), photolithography, and inductively coupled plasma-reactive ion etching (ICP-RIE), coupled with characterization techniques such as optical microscopy and scanning electron microscopy (SEM). Lastly, the fabricated MARC devices will be characterized using a transmission characterization setup for waveguide devices, and the results will be compared to the simulated MARC transmission spectra.

Abstract

Photonic devices based on the silicon-on-insulator (SOI)-platform have gained increased interest in the recent years due to their applicability in photonic integrated circuits (PICs). PICs are a good foundation for diagnostics-oriented lab-on-chip (LOC) applications exploiting interferometric biosensing capabilities, and the Mach-Zehnder interferometer-assisted ring resonator configuration (MARC) photonic sensor is one example of such a device. A MARC sensor combines the resonant behavior of an add-drop ring resonator, with the phase-intensity conversion functionality of a Mach-Zehnder interferometer. This extends the dynamic measurement range of the ring resonator, while simultaneously shaping the transmission response of the device, providing a unique spectral fingerprint suitable for multiplexing.

The finite-elements method (FEM)-based simulation software COMSOL Multiphysics 5.4 / 6.0 (COMSOL) has been used to design, optimize and simulate three "conventional" single-ring MARC devices, as well as combining these three configurations into a multiplexed MARC. The three MARCs comprise different angular separations in their ring resonators (135°, 90°, and 240°), and their transmission characteristics (including transmission response, quality factor (Q), full-width at half-maximum (FWHM) and overall interferometer balance) have been discussed.

After optimizations to the COMSOL models were made, the single-ring MARCs as well as the multiplexed MARC were fabricated (at NTNU NanoLab) on an SOI platform using plasma-enhanced chemical vapor deposition (PECVD), electron beam lithography (EBL), inductively coupled plasma-reactive ion etching (ICP-RIE) and near-UV photolithography. Scanning electron microscopy (SEM) was performed during and after the fabrication process to verify and characterize the MARC devices.

The simulation models show Q of approximately 9500, 7700, and 6900, for the 135°, 90°, and the 240° MARCs, respectively. While the 135° and 240° MARCs display excellent balance over the simulated wavelength range of 1510-1550 nm, the 90° MARC suffers from significant imbalance. The transmission spectrum of the multiplexed MARC, while not being of particularly good quality, still displays the device's ability to multiplex signals: A refractive index change of $\Delta n = 0.010$ was introduced to the 240° ring, and this caused a shift in the resonant wavelength of $\Delta \lambda \approx 5.3$ nm in the peaks corresponding to that ring.

The transmission spectra of the fabricated MARCs were characterized using a tunable laser source, butt-coupled into inverted taper couplers on the waveguide structures. Wavelength sweeps (1540-1560 nm) were performed, and the 135° and 240° MARCs provided high-quality transmission responses, characterized by low noise and narrow peaks. While the 135° MARC displays very good balance, the 240° and 90° MARCs are quite unbalanced. The 90° MARC was heavily characterized by noise, but the multiplexed MARC displayed excellent features and low noise levels from all constituent rings. For all MARCs, the free spectral range (FSR) was measured to be approximately 62% of the simulated FSR. This illuminates shortcomings in the simulated MARC models, however other possible reasons for the discrepancy are discussed as well.

Due to time constraints, actual sensor measurements were not performed in this project, however the quality of the acquired multiplexed spectrum may indicate that the sensor configuration presented in this work is indeed a good candidate for a high-precision, multiplexed MARC device used for LOC applications.

Sammendrag

Fotoniske enheter basert på silisium-på-isolator (SOI)-plattformen har sett en økt interesse de siste årene, grunnet deres anvendelighet i fotoniske integrerte kretser (PICer). PICer er et godt utgangspunkt for applikasjoner basert på diagnostikk-orienterte brikkelaboratorier (*lab-on-chip* (LOC)), der interferometriske biosensorkapabiliteter benyttes. Et eksempel på en slik teknologi er såkalte Mach-Zehnder interferometer-assisterte ringresonatorkonfigurasjoner (MARC), som kombinerer resonansoppførselen til en *add-drop* ringresonator med fase-intensitetskonverteringen til et Mach-Zehnder interferometer. Dette forlenger den dynamiske målerekkevidden til ringresonatoren, samtidig som at transmisjonsresponsen til MARC-enheten får et unikt spektralt fingeravtrykk som åpner opp for multipleksing.

Simuleringsprogramvaren COMSOL Multiphysics 5.4 / 6.0 (COMSOL), som er basert på endelige elementmetoder (FEM), er blitt benyttet til å designe, optimere og simulere tre ”konvensjonelle” enkeltring-MARC-strukturer, så vel som til å kombinere disse tre konfigurasjonene til én multiplekset MARC. De tre MARCene har ulike vinkelseparasjoner i sine respektive ringresonatorer (135°, 90° og 240°), og deres transmisjonskarakteristikker (inkludert transmisjonsrespons, kvalitetsfaktor (Q), fullbredde ved halvmaksimum (FWHM) og overordnet ubalanse i interferometer) er blitt diskutert.

Etter optimaliseringer var utført på COMSOL-modellene, ble enkeltring-MARCene og den multipleksede MARC-strukturen fabrikkert (hos NTNU NanoLab) på en SOI-plattform. Plasmaforsterket kjemisk dampavsetning (PECVD), elektronstrålelitografi (EBL), reaktiv ioneetsing med induktivt koplet plasma (ICP-RIE) og nær-UV fotolitografi er benyttet, i tillegg til at MARC-fabrikasjonen ble verifisert og karakterisert ved hjelp av sveipelektronmikroskopi (SEM).

De simulerte modellene viser en Q på omtrentlig 9500, 7700, 6900, for henholdsvis 135°, 90° og 240°-MARCene. Både 135°- og 240°-MARCene viser utmerket balanse over hele bølgelengdeområdet på 1510-1550 nm, hvorimot 90°-MARCen er preget av betydelig ubalanse. Til tross for den lave kvaliteten på det simulerte transmisjonsspekteret til den multipleksede MARCen, viser spekteret likefullt sensorens evne til å multiplekse signaler: En endring i brytningsindeksen på $\Delta n = 0.010$ ble introdusert i 240°-ringen, noe som førte til en forskyvning i resonansbølgelengden på $\Delta \lambda \approx 5.3$ nm til de tilhørende transmisjonstopperne til ringen.

Transmisjonsspekterne til de fabrikerte MARCene ble karakterisert ved hjelp av en justerbar laserkilde, endekoplet til omvendte kilekoplere (*inverted taper couplers*) på bølgelederstrukturene. Sveip over ulike bølgelengder (1540-1560 nm) ble utført, og 135°- og 240°-MARCene ga transmisjonsspekter av høy kvalitet, preget av lite støy og smale transmisjonstopper. Der 135°-MARCen viser meget god balanse over bølgelengdeområdet, er derimot 240°- og 90°-MARCene sterkt påvirket av ubalanse. 90°-MARCen er således også sterkt preget av støy. På den annen side er den multipleksede MARCen eksemplarisk i sin oppførsel og er preget av skarpe topper og generelt lite støy, for alle ringene i strukturen. For alle MARCene ble det målt en fri spektralvidde (FSR) på omtrentlig 62% av den simulerte verdien for FSR. Dette belyser begrensninger i de simulerte MARC-modellene, men andre mulige grunner for dette avviket diskuteres også.

På grunn av tidsbegrensninger ble ikke sensoren testet på faktiske målinger, men kvaliteten på det multipleksede spekteret kan indikere at konfigurasjonen som er presentert i dette arbeidet er en god kandidat for en høypresisjons multiplekset MARC-enhet, som i fremtiden kan brukes til LOC-applikasjoner.

Preface

The submission of this thesis completes my degree as a Master of Science (M.Sc.) in Nanotechnology at the Department of Electrical Systems (IES), at the Norwegian University of Science and Technology (NTNU) in Trondheim. The work presented in this thesis is a continuation of my project work conducted last semester, in the autumn of 2021[1], which also dealt with simulations of MARC structures, albeit in a simpler configuration. Chapters 1 (Introduction), 2 (Theory) and 3 (Methods) are therefore largely based on that report, however they have been expanded to include sections covering waveguide loss, in-coupling, and fabrication techniques.

This work is thematically related to previous work at IES[2–4], and the fabrication techniques used are based on their work. It is however worth noting that the work and results presented in this thesis are in their entirety my own work.

All illustrations are, unless otherwise stated, made by me using Adobe Illustrator 2021¹.



Trondheim, June 20th, 2022

¹<https://www.adobe.com/products/illustrator.html>

Acknowledgements

Firstly, I would like to thank my supervisor, professor Astrid Aksnes. Her enthusiasm and optimism have been highly motivating throughout the two preceding semesters. Despite her busy schedule, she has always had the time to care for her master's students.

My co-supervisors, Jong Wook Noh, Jens Høvik and Mukesh Yadav also deserves appreciation: Jong has been of great help with all things regarding the transmission characterization lab. Jens has been invaluable for the fabrication process and the usage of NanoLab tools and equipment, while Mukesh has been superbly helpful in the early fabrication stages of this project.

Big thanks to my classmates Erik Møller Steen, Amund Stensrud Normann, and Nikolai Stensø, who took time out of their own thesis writing to help me through the fabrication and characterization processes. Erik took brilliant SEM images for me as part of the EBL dose testing, while Amund helped me with the fabrication of the inverted taper polymer waveguides, sharing his experiences with SU-8 photoresist and the maskless aligner. Nikolai has experience with the transmission measurement setup, and he helped me greatly with taking measurements of the fabricated MARC device.

Moreover, I would like to thank Timini, the student association for nanotechnology students at NTNU, for giving me the opportunity to meet truly wonderful people and for organizing fun and festive events, making these five years in Trondheim my best yet. Also, a special shout-out to my classmates in the study hall in A2, for providing fruitful discussions, great tips on report writing, late nights in the study hall, and very long lunch breaks.

Thank you NTNU NanoLab (and its staff), for providing me with the facilities, tools, training and support required to perform the experimental work in this thesis.

Lastly, a big thanks is given to The Research Council of Norway, for their support to the Norwegian Micro- and Nano-Fabrication Facility, NorFab, project number 295864.

Contents

Problem Description	i
Abstract	iii
Sammendrag	v
Preface	vii
Acknowledgements	ix
List of Figures	xvi
List of Tables	xvii
List of Abbreviations	xix
1 Introduction	1
2 Theory	3
2.1 Electromagnetic Theory of Light	3
2.2 Wave Interference	5
2.2.1 Interferometry	5
2.3 Guided Waves	6
2.3.1 Planar Mirror Waveguides	7
2.3.2 Dielectric Waveguides	9
2.3.3 Input Coupling	12
2.3.4 Loss in Waveguides	13
2.4 Optical Resonators	14
2.4.1 Fabry-Perot Resonator	15
2.4.2 Ring Resonators	15
2.5 MARC Devices	19
2.5.1 Resonance Lineshapes	20
2.6 Multiplexing MARC Sensors	21
2.7 Ring Resonators as Sensors	22
3 Methods	23
3.1 Python Programming	23
3.2 COMSOL Simulations	24
3.2.1 Effective Mode Index Approximations	25
3.3 Fabrication Tools	25
3.3.1 Plasma-Enhanced Chemical Vapor Deposition	26
3.3.2 Electron Beam Lithography	27

3.3.3	Inductively Coupled Plasma-Reactive Ion Etching	28
3.3.4	Photolithography	28
3.4	Characterization Tools	29
3.4.1	Optical Microscope	29
3.4.2	Scanning Electron Microscope	29
4	Experimental Procedures	31
4.1	COMSOL Simulation Work	31
4.1.1	Physics and Study	31
4.1.2	Effective Mode Index Analysis	31
4.1.3	Implementing Waveguide Losses	32
4.1.4	Key Parameters	33
4.1.5	Mesh Setup	34
4.1.6	Component Design and Optimization	34
4.1.7	Balancing of Individual MARCs	35
4.2	Lithography Mask Design	36
4.3	Fabrication	37
4.3.1	Wafer Preparation	37
4.3.2	Silicon Deposition	38
4.3.3	Wafer Dicing	38
4.3.4	Waveguide Patterning	39
4.3.5	Etching	39
4.3.6	Inverted Taper Fabrication	40
4.4	Characterization	40
4.4.1	Optical Microscopy	40
4.4.2	Scanning Electron Microscopy	40
4.5	Transmission Characterization Setup	41
5	Results and Discussion	43
5.1	Individual Component Simulations	43
5.1.1	3dB Coupler	43
5.1.2	Ring Resonators	43
5.1.3	Mach-Zehnder Interferometer	43
5.2	MARC Simulations	45
5.2.1	Individual MARC simulations	45
5.2.2	Multiplexed MARC Simulations	48
5.3	Fabrication Results	51
5.4	MARC Measurements	54
5.4.1	240° MARC	54
5.4.2	90° MARC	55
5.4.3	135° MARC	56
5.4.4	Multiplexed MARC	56
5.5	Simulations vs. Fabricated MARCs	59
6	Conclusion	61
6.1	Simulations	61

6.2 Fabrication	61
6.3 Future Work	62
Appendices	63
A Theoretical MARC Spectra	63
B Python Code	65
C Lithography Mask Design	69
C.1 Extracting Model Parameters	69
C.2 Building the Mask Layout	69
D Notes on COMSOL Resource Usage	71
D.1 Storage Usage	71
D.2 Memory Usage	71
E Additional COMSOL Parameters	73
E.1 Boundary Mode Analyses	73
F Additional MARC Measurements	75
References	81

List of Figures

2.1	Boundary conditions at the interface between two dielectrics	4
2.2	a) Schematic of a Mach-Zehnder interferometer. b) The transmission response of an MZI	6
2.3	a) Schematic of a planar mirror waveguide. b) Field distribution in a planar mirror waveguide	7
2.4	a) The principle of self-consistency. b) Illustration of how higher bounce angles lead to a lower propagation constant	8
2.5	Snell's law of refraction	9
2.6	Field distribution in a planar dielectric waveguide	9
2.7	Asymmetric planar waveguide	10
2.8	a) Schematic of waveguide coupling. b) Mode distribution in coupling waveguides .	12
2.9	Different waveguide configurations	13
2.10	Schematic of an inverted taper input coupler	14
2.11	Illustration of the effects of sidewall roughness in waveguides	14
2.12	The working principles of ring resonators	16
2.13	Transmission response of add-drop ring resonator	19
2.14	Schematic showing the angular separation θ between through-port and drop-port .	19
2.15	Simple schematic of a single-ring MARC sensor	20
2.16	Schematic of a three-ring (multiplexed) MARC device	21
2.17	a) Lorentzian lineshape. b) Fano lineshape	21
2.18	All-pass ring resonator transmission response before and after a measurement . . .	22
3.1	Illustration of a typical COMSOL workflow	24
3.2	Schematic of a general PECVD chamber	26
3.3	a) Schematic of an EBL, b) Beam cross-section at write field boundaries	27
3.4	Schematic of a generic ICP-RIE	29
4.1	The effective mode index method COMSOL model	32
4.2	Transmittance through 100 μm waveguide core, as a function of the imaginary refractive index	32
4.3	Waveguide loss as a function of the bending radius of the waveguide.	33
4.4	Overview of the mesh applied to the COMSOL model	34
4.5	COMSOL model of the 3dB (input) coupler	35
4.6	COMSOL model of the multiplexed, 3-ring MARC	36
4.7	Overview of the lithography mask used in the fabrication of the MARCs	37
4.8	Waveguide fabrication process overview	38
4.9	Schematic of the transmission characterization setup used in the lab	41
5.1	Intensity transmission of the 3dB directional coupler	44

5.2	a) Absorption for different wavelengths in the MZI of the COMSOL MARC model. b) COMSOL model of the MZI	45
5.3	a) Simulated transmission response of the 240° MARC sensor. b) COMSOL model of the 240° MARC sensor	46
5.4	a) Simulated transmission response of the 90° MARC sensor. b) COMSOL model of the 90° MARC sensor	47
5.5	a) Simulated transmission response of the 135° MARC sensor. b) COMSOL model of the 135° MARC sensor	48
5.6	Simulated transmission response of the multiplexed MARC sensor	49
5.7	Simulated transmission response before (solid red) and after (dashed green) the fictitious measurand	50
5.8	SEM overview of MARC #16	52
5.9	Cross-sectional SEM images of waveguide structures	52
5.10	Top-down view SEM images of the various coupling regions of the fabricated MARCs	53
5.11	Transmission spectrum from the fabricated 240° MARC	54
5.12	Transmission spectrum from the fabricated 90° MARC	55
5.13	Transmission spectrum from the fabricated 135° MARC	57
5.14	Transmission spectrum from the fabricated 3-ring MARC	58
5.15	IR photography of MARC #20 at three resonant wavelengths	58
A.1	Theoretical transmission spectrum of a single-ring 135° MARC	63
A.2	Theoretical transmission spectrum of a single-ring 90° MARC	64
A.3	Theoretical transmission spectrum of a single-ring 240° MARC	64
E.1	Applied settings for the boundary mode analysis of Port 1	73
F.1	Wide transmission spectrum of the fabricated 240° single-ring MARC	75
F.2	Wide transmission spectrum of the fabricated 90° single-ring MARC	75
F.3	Wide transmission spectrum of the fabricated 135° single-ring MARC	76
F.4	Wide transmission spectrum of the fabricated multiplexed MARC	76

List of Tables

4.1	Refractive indices of air, Si and SiO ₂ as used in the effective mode analysis	31
4.2	General parameters used in the COMSOL simulation of the MARC sensors	33
4.3	COMSOL mesh size parameters used in the simulations	34
4.4	Process parameters for the PECVD deposition of a-Si	38
4.5	Spin coat deposition and EBL operating parameters used for waveguide patterning	39
4.6	ICP-RIE parameters for etching a-Si	40
4.7	Spin coat and photolithography processing parameters used for inverted taper pat- ttering	41
5.1	Optimized ring parameters used in single-ring and multiplexed MARCs	44
5.2	Dimensional measurements of the fabricated MARC #16	51

List of Abbreviations

a-Si	Amorphous Silicon
a.u.	Arbitratry Units
BSE	Backscattered Electrons
c-Si	Crystalline Silicon
CAD	Computer-Aided Design
CMOS	Complementary Metal-Oxide Semiconductor
COMSOL	COMSOL Multiphysics 5.4 / 6.0
CSAR 62	Allresist AR-P 6200
CVD	Chemical Vapor Deposition
DAQ	Data Acquisition Device
EBL	Electron Beam Lithography
FEM	Finite-Elements Method
FP	Fabry-Perot
FSR	Free Spectral Range
FWHM	Full-Width at Half-Maximum
ICP-RIE	Inductively Coupled Plasma-Reactive Ion Etching
IES	Department of Electronic Systems
IR	Infrared
IPA	Isopropanol
LOC	Lab-on-chip
MARC	Mach Zehnder Interferometer-Assisted Ring Resonator Configuration
MZI	Mach-Zehnder Interferometer
NTNU	Norwegian University of Science and Technology
PEB	Post-Exposure Bake
PECVD	Plasma-Enhanced Chemical Vapor Deposition
PIC	Photonic Integrated Circuit
PML	Perfectly Matched Layer
RF	Radio Frequency
RIE	Reactive Ion Etching
sccm	Standard cubic centimeters per minute
SE	Secondary Electrons
SEM	Scanning Electron Microscope
SiH₄	Silane
SiO₂	Silicon Dioxide
SOI	Silicon-on-Insulator
SU-8	MicroChem SU-8 2000
TE	Transverse Electric
TEM	Transverse Electromagnetic
TIR	Total Internal Reflection
TM	Transverse Magnetic

Chapter 1

Introduction

Medicine as a science is a continuously evolving field, and progress is constantly being made in both treatment and diagnostics. The last few years, particularly with the global Covid-19 pandemic still fresh in memory, have shown the importance of rapid testing and diagnosing[5, 6], however this is not something unique to pandemics – in fact, early detection is important in all forms of disease. Developing a readily available, low-cost and rapid way of detecting biomarkers may therefore prove valuable in improving the public’s health, all over the world.

Silicon-on-insulator (SOI) based photonic sensor devices have recently seen increased interest, as they can be produced at a low-cost in high volumes, and with good reliability[7]. This is due to the compatibility with complementary metal-oxide semiconductor (CMOS)-based processing techniques. Moreover, as Si is transparent to wavelengths in the telecommunications band (1200-1700 nm)[8], SOI technology also allows for the use of inexpensive components like light sources and detectors originally designed for use in telecommunications systems. The possibility of having a high density of devices on a small wafer area, with high refractive index contrast, also make SOI based devices good candidates for comprising photonic integrated circuits (PICs)[9]. These circuits may very well be the foundation of lab-on-chip (LOC) device integration for diagnostics purposes.

A Mach-Zehnder interferometer-assisted ring resonator configuration (MARC) sensor is essentially a Mach-Zehnder interferometer (MZI) coupled with an add-drop ring resonator, which gives the sensor a unique and tailorable transmission spectrum[3]. This not only increases the dynamic measurement range compared to a conventional ring resonator configuration, but it also allows for the multiplexing of several MARC sensors[4]. Each individual MARC may be tailored for a specific measurand or for a certain measurement range and given a distinct spectral fingerprint. The multiplexed MARC sensor thus allows for a very useful device capable of measuring several factors simultaneously, enabling a higher measurement throughput beneficial for rapid LOC applications.

The ongoing research project that this work is a part of, has as its goal to develop an LOC platform for diagnostics, based on the MARC sensor design[2]. In order to allow this device to perform multiple measurements at once, multiplexing individual MARC sensors naturally is of interest to the research group.

In this project, three different single-ring MARC sensor devices have been modeled, simulated and optimized using the finite-elements method (FEM)-based COMSOL Multiphysics 5.4 / 6.0 (COMSOL) simulation software^{1,2}, before being combined into a single, multiplexed 3-ring MARC sensor. Idealized, theoretical MARCs have also been simulated using the programming language Python³, for comparison with the COMSOL simulations. The final design of the single-ring MARCs and the multiplexed MARC were then fabricated at NTNU NanoLab⁴, as a proof-of-concept of the sensor design. The resulting measurements from these realized devices were then compared to their simulated counterparts.

The basic theory and the principles behind electromagnetic waves, waveguiding and coupling, optical resonators, and MARC devices will be introduced in chapter 2. In chapter 3, the relevant methods for the programming and the simulation work will be presented, along with brief de-

¹<https://www.comsol.com/comsol-multiphysics>

²COMSOL Multiphysics 6.0 was also used in the later stages of this project

³<https://www.python.org/>

⁴<https://www.ntnu.edu/nano/nanolab>

scriptions of the experimental methods and tools used. In chapter 4, the experimental procedures will be presented, both for the simulation work and the fabrication work. The results from both simulations and the realized MARC structure will be presented and discussed in chapter 5, before the final conclusion is provided in chapter 6, along with some notes on the possibilities for future work.

Additional details and technicalities are included as appendices: Appendix A presents some theoretical MARC transmission spectra, as calculated using the theoretical MARC script for Python, which is presented in full in Appendix B. Some more information on how the lithographic mask design was performed is presented in Appendix C. Appendix D discusses more details regarding optimizations to the COMSOL simulation procedures, and Appendix E presents a few more parameters used in the COMSOL simulations. Appendix F presents some additional results from the fabricated MARC transmission measurements.

Chapter 2

Theory

This chapter will introduce the relevant theory that forms the basis for the operation of the photonic sensor considered in this thesis. The foundations will be laid with basic electromagnetic theory, before wave optics and waveguide principles are considered. Optical resonators are then introduced, before the working principles of so-called Mach-Zehnder interferometer-assisted ring resonator configuration (MARC) devices are described. Finally, a short note on how ring resonators can be used as sensor devices is provided, to aid the reader in understanding how the MARC sensor is able to perform measurements.

2.1 Electromagnetic Theory of Light

In a source-free medium with no surface charges, Maxwell's equations are given as[10]

$$\nabla \times \mathbf{E} = -\frac{\partial \mathbf{B}}{\partial t} \quad (2.1)$$

$$\nabla \times \mathbf{H} = \frac{\partial \mathbf{D}}{\partial t} \quad (2.2)$$

$$\nabla \cdot \mathbf{D} = 0 \quad (2.3)$$

$$\nabla \cdot \mathbf{B} = 0, \quad (2.4)$$

where $\mathbf{E} = \mathbf{E}(\mathbf{r}, t)$ is the electric field and $\mathbf{H} = \mathbf{H}(\mathbf{r}, t)$ is the magnetic field, both as functions of position \mathbf{r} and time t . If no external fields are applied, the electric flux density can be represented by $\mathbf{D} = \epsilon \mathbf{E}$, and the magnetic flux density by $\mathbf{B} = \mu \mathbf{H}$, in which ϵ and μ are the electric permittivity and magnetic permeability, respectively.

The proper boundary conditions are needed for solving eqns. 2.1-2.4. These are illustrated in fig. 2.1, and stated mathematically as [11]

$$E_{1t} = E_{2t} \quad (2.5)$$

$$H_{1t} = H_{2t} \quad (2.6)$$

$$D_{1n} = D_{2n} \quad (2.7)$$

$$B_{1n} = B_{2n}, \quad (2.8)$$

given that there are no surface currents or charges. The subscripts t and n denote the tangential and normal components, respectively.

All components of the four fields discussed so far are thus continuous functions of position. It is also required that all components of both \mathbf{E} and \mathbf{H} satisfy the wave equation

$$\nabla^2 u - \frac{1}{c^2} \frac{\partial^2 u}{\partial t^2} = 0, \quad (2.9)$$

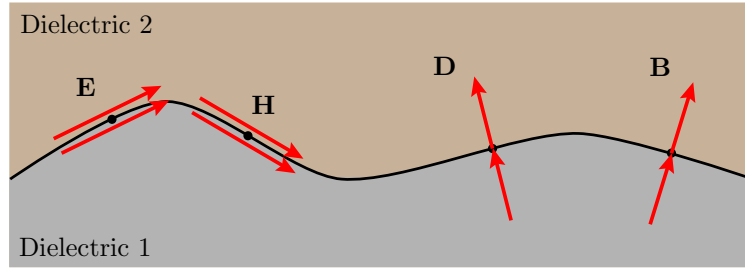


Figure 2.1: Boundary conditions at the interface between two dielectrics, in the absence of surface currents and -charges. Figure adapted from [10].

in which c denotes the speed of light in the medium and is given as

$$c = \frac{1}{\sqrt{\epsilon\mu}}. \quad (2.10)$$

u is the real wavefunction representing the wave in question, and it is convenient to represent this via a complex wavefunction U , such that

$$U(\mathbf{r}, t) = a(\mathbf{r}) \exp[j\varphi(\mathbf{r})] \exp(j2\pi\nu t), \quad (2.11)$$

where ν is the frequency of the wave, such that

$$u(\mathbf{r}, t) = \text{Re} \{U(\mathbf{r}, t)\} = \frac{1}{2} [U(\mathbf{r}, t) + U^*(\mathbf{r}, t)], \quad (2.12)$$

and U will still satisfy eqn. 2.9. The optical intensity of the wave is given as

$$I(\mathbf{r}) = |U(\mathbf{r})|^2. \quad (2.13)$$

Assuming the complex wavefunction can be written on the form

$$U(\mathbf{r}, t) = U(\mathbf{r}) \exp(j2\pi\nu t), \quad (2.14)$$

the wave equation from eqn. 2.9 turns into

$$\nabla^2 U + k^2 U = 0, \quad (2.15)$$

where

$$k = \frac{2\pi\nu}{c} = \frac{\omega}{c} = \frac{2\pi}{\lambda} \quad (2.16)$$

is the so-called wavenumber (also commonly referred to as the *wavevector*). Eqn. 2.15 is commonly referred to as the **Helmholtz equation**. $\omega = 2\pi\nu$ is the angular frequency, while λ is the wavelength of the wave in the medium. The wavenumber relates the phase ϕ of the wave to the propagated distance z as

$$\phi = kz. \quad (2.17)$$

The speed of light in a medium differs from that in free space by a factor called the **refractive index**, n . The refractive index is dependent on the medium in question – it may very well depend on external fields as well – and is given as

$$n = \frac{c_0}{c} = \sqrt{\frac{\epsilon}{\epsilon_0}}, \quad c_0 = \frac{1}{\sqrt{\epsilon_0\mu_0}}, \quad (2.18)$$

where ϵ_0 and μ_0 are the electric vacuum permittivity and the magnetic vacuum permeability (both

constants), respectively, and thus c_0 is the speed of light in free space, analogous to eqn. 2.10. Two other useful relations featuring n include

$$\lambda = \frac{\lambda_0}{n}, \quad k = nk_0, \quad (2.19)$$

where λ_0 denotes the free-space wavelength and k_0 denotes the free-space wavenumber.

If the medium in question is lossy, the refractive index takes a complex value and can be written as

$$\tilde{n} = n - ik_i, \quad (2.20)$$

where n is the usual refractive index, and k_i is the extinction coefficient [12] (also typically referred to as the absorption coefficient).

Electromagnetic light can take on three different modes, depending on the direction of the electric- and magnetic fields relative to the propagation direction. Transverse electromagnetic (TEM) waves have both the electric- and magnetic field orthogonal to both the propagation direction and to each other. In transverse electric (TE) waves, only the electric field is transverse to the propagation direction and have no components in the propagation direction. For transverse magnetic (TM) waves, this is the case for the magnetic field, and not the electric field.

2.2 Wave Interference

When two (or more) monochromatic waves combine at the same point in time and space, the total wavefunction of the system is simply the sum of the individual wavefunctions [10]. For a multi-wave system of N superposed waves, we thus have

$$U(\mathbf{r}) = U_1(\mathbf{r}) + U_2(\mathbf{r}) + \cdots + U_N(\mathbf{r}), \quad (2.21)$$

in which U_i denotes the complex amplitude of wave i .

The intensity of the total wavefunction is however not subject to the superposition principle, as the intensity depends on the relationship between the phases of the superposed waves. From eqn. 2.13, we thus get

$$I = |U|^2 = |U_1 + U_2|^2 = |U_1|^2 + |U_2|^2 + U_1^*U_2 + U_1U_2^*, \quad (2.22)$$

for a two-wave system. If we then rewrite U_1 and U_2 as

$$U_1 = \sqrt{I_1} \exp(j\varphi_1), \quad U_2 = \sqrt{I_2} \exp(j\varphi_2), \quad (2.23)$$

where φ_1 and φ_2 are the phases of the waves, we arrive at the **interference equation**,

$$I = I_1 + I_2 + 2\sqrt{I_1I_2} \cos \varphi, \quad \varphi = \varphi_2 - \varphi_1. \quad (2.24)$$

If both waves have the same intensity $I_1 = I_2 = I_0$, it is clear that for zero (or any integer multiple of 2π) phase difference φ , the combined intensity is $I = 4I_0$, whereas for φ being any odd integer multiple of π , the intensity is completely canceled out. The phase difference φ is thus manifested through the intensity of the light after a combination of the two waves, and this is the foundation of **interferometry**.

2.2.1 Interferometry

Interferometers come in a wide variety, however the principle remains the same: Light enters the interferometer where it is (equally) divided into two paths. One of the paths is altered (in some

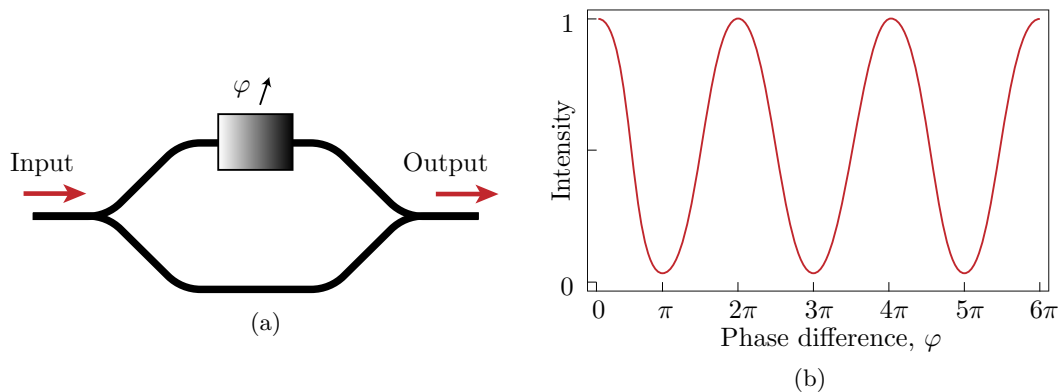


Figure 2.2: a) Schematic of a Mach-Zehnder interferometer. The input light is split into two beams, where one of the beams experiences a phase delay (denoted by the variable φ). Interference effects arise when the two beams recombine at the output. b) The transmission response of an MZI as a function of the phase difference in the arms.

way, this depends on the actual application), and the induced phase shift is detected as a change in intensity as the separated waves recombine at the output of the interferometer.

Interferometers are highly sensitive measurement devices, and they can be used in a wide range of applications, ranging from electro-optic modulators used in telecommunications systems[13], to large facilities used to detect gravitational waves[14]. Interferometers may very well also be used for biological sensor applications[15], which is the aim of the device considered in this project.

Three common types of interferometers include the Mach-Zehnder, Michelson and Sagnac interferometers. In this section we will look more closely at the Mach-Zehnder configuration, as this is the basis of the Mach-Zehnder assisted ring resonator configuration (MARC) device that this project considers.

2.2.1.1 Mach-Zehnder Interferometers

The working principle of the Mach-Zehnder interferometer (MZI) is shown in fig. 2.2a. The input light is split into two beams at the input of the MZI. Due to external factors (e.g. applied electric fields, temperature, or simply length differences between the interferometer arms) the two beams will experience different optical path lengths, and thus the light in one arm will be delayed relative to the light in the other arm. This phase delay leads to interference effects at the output of the MZI as the two beams recombine, resulting in a change in intensity. As dictated by the interference equation (eqn. 2.24), the output intensity spectrum has a periodicity of 2π . This transmission response is shown in fig. 2.2b.

2.3 Guided Waves

A waveguide is a structure capable of guiding waves[11], i.e. being able to confine the electric (and magnetic) energy of a wave within the structure itself, while still enabling propagation of the wave. In order to gain an understanding of the working principles behind waveguides, we will first consider planar mirror waveguides, as they provide valuable insights to the mechanisms behind propagating waves. Afterwards, planar dielectric waveguides will be considered. Dielectric waveguides are a key component in integrated photonic circuits and will be the main focus of this section.

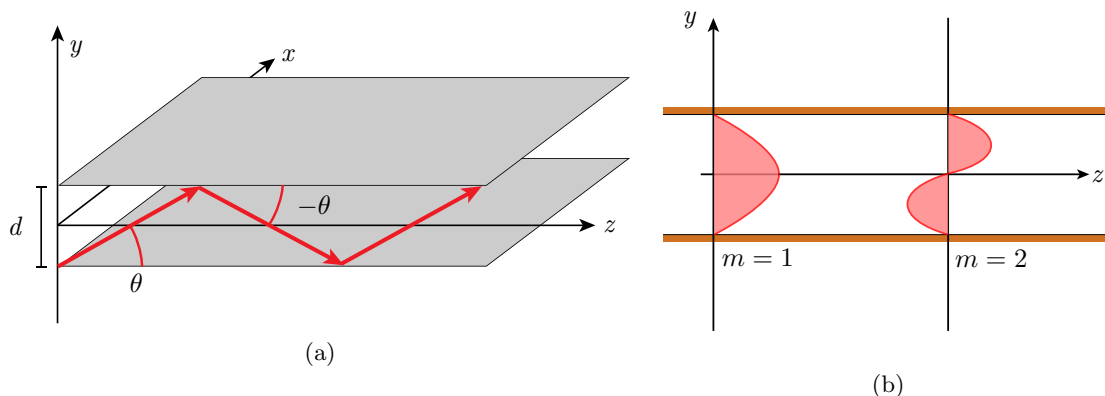


Figure 2.3: a) Schematic of a planar mirror waveguide in which the light "bounces" between two perfect mirrors. b) Field distribution of the two lowest-order modes in a planar mirror waveguide. Figures a) and b) are adapted from [10].

2.3.1 Planar Mirror Waveguides

Planar mirror waveguides are comprised of two parallel (infinite) planar mirrors, separated by some distance d . The mirrors are typically assumed to be lossless and perfect reflectors, and the wave of light propagates through the waveguide by "bouncing" between the mirrors at an angle θ , see fig. 2.3a. Due to the high cost and difficulty of making high quality mirrors, planar mirror waveguides do not see much practical use [10].

The wavenumber k describes the propagation of the wave in a waveguide, and can be decomposed into two orthogonal components, namely

$$\begin{aligned} k_z &= nk_0 \cos \theta \equiv \beta, \\ k_y &= nk_0 \sin \theta, \end{aligned} \quad (2.25)$$

where β typically is referred to as the *propagation constant*, and n is the refractive index of the medium between the mirrors.

An important concept in waveguide theory is the so-called **self-consistency** condition, which is illustrated in fig. 2.4a. This condition requires that after two reflections, the wave reproduces itself. As a consequence, the waves propagating in the waveguide are a superposition of two distinct plane waves. If self-consistency is not satisfied, the resulting destructive interference will not allow for the propagation of the wave.

Mathematically, the self-consistency condition requires that any phase delay for a wave experiencing two reflections must be equal to an integer number of 2π . We can consider the wave component traveling in the y -direction only, and require that this wave forms a standing wave between the parallel mirrors. The wave propagation itself between the mirrors causes the first part of this phase delay, given as [16]

$$\phi_d = 2k_y d = 2nk_0 d \sin \theta. \quad (2.26)$$

Due to the two reflections, another two phase shifts are introduced, namely ϕ_{\downarrow} and ϕ_{\uparrow} , representing the phase shifts from the lower and upper reflections, respectively. This total phase shift must then equal an integer number of 2π , i.e.

$$2nk_0 d \sin \theta - \phi_{\downarrow} - \phi_{\uparrow} = 2\pi m, \quad m = 1, 2, 3, \dots, \quad (2.27)$$

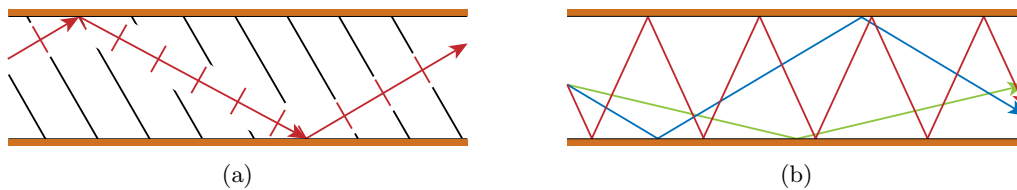


Figure 2.4: a) The principle of self-consistency. The wavefronts of one of the two plane waves comprising the propagating mode are shown as solid black lines. After two reflections, the wave reproduces itself. b) Illustration of how higher bounce angles lead to a lower propagation constant. The green wave travels a shorter distance than the blue and red waves, and thus the propagation constant β_m is higher.

which for a perfect-mirror waveguide is reduced to

$$\sin \theta_m = m \frac{\lambda}{2d}, \quad m = 1, 2, 3, \dots, \quad (2.28)$$

since reflections from perfect mirrors give a phase shift of π [10].

From eqn. 2.28 it is clear that not all bounce angles will support self-consistency. The angles that do, however, give rise to the so-called *modes* of the waveguide. The modes are the fields that are allowed to propagate in the waveguide, with identical transverse distribution and polarization at all points in the waveguide [10]. Eqn. 2.28 also demonstrates that higher order modes (i.e. higher m) experience steeper bounce angles, which means that higher-order modes propagate more slowly through the waveguide than lower-order modes, see fig. 2.4b. The field distribution of the two lowest order modes in a planar mirror waveguide is shown in fig. 2.3b.

The total number of modes, M , supported by the waveguide is given by

$$\sin \theta_m = m \frac{\lambda}{2d} < 1, \quad \implies M = \left\lfloor \frac{2d}{\lambda} \right\rfloor, \quad (2.29)$$

where $\lfloor \dots \rfloor$ denotes rounding down to the nearest integer, i.e. $0.8 \rightarrow 0, 1 \rightarrow 1, 1.1 \rightarrow 1$, etc.

As the bounce angles are quantized, so too are the wavevector components, i.e.

$$k_{ym} = nk_0 \sin \theta_m = m \frac{\pi}{d}, \quad (2.30)$$

and

$$\beta_m = k_{zm} = nk_0 \cos \theta_m \implies \beta_m^2 = k^2 - \frac{m^2 \pi^2}{d^2}, \quad (2.31)$$

where we have used eqn. 2.28 and the trigonometric identity $\cos^2 \alpha = 1 - \sin^2 \alpha$. Eqn. 2.31 clearly reaffirms the claim that higher-order modes propagate more slowly in the waveguide, which is also imminent from fig. 2.4b.

An important parameter for a waveguide is the so-called cutoff frequency, ν_c , which is the lowest frequency allowed to propagate in the waveguide. This is given by eqn. 2.29, if used in conjunction with the relation between wavelength and frequency, $\lambda = c/\nu$. The cutoff frequency is then given for the case when $M < 1$, i.e.

$$\frac{2d\nu}{c} < 1 \implies \nu_c = \frac{c}{2d}. \quad (2.32)$$

In the special case of $M = 1$, the waveguide is often referred to as being a **single-mode waveguide**.

We have only considered TE waves thus far and will continue to do so in this project. A TE wave is here defined as an electromagnetic wave having the electric field oscillating in the

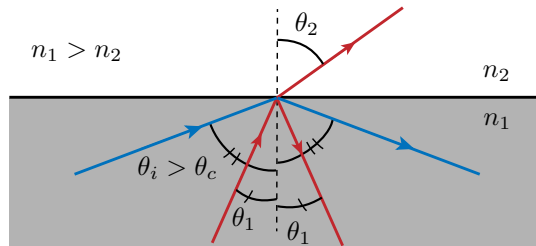


Figure 2.5: Snell's law of refraction. The blue wave is incident to the boundary at an angle $\theta_i > \theta_c$ and thus experiences total internal reflection. Figure adapted from [16].

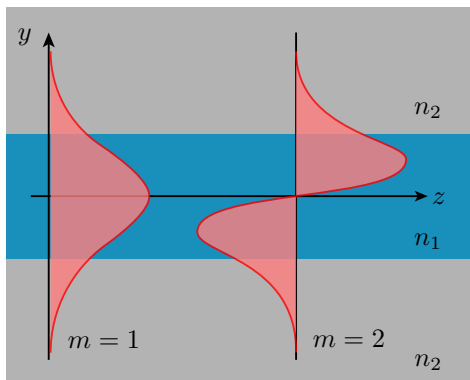


Figure 2.6: Field distributions of the two lowest order modes in a planar dielectric waveguide. Notice the evanescent field reaching outside the waveguiding structure denoted in blue. The figure is adapted from [10].

x-direction with propagation in the z-direction, as according to the coordinate system shown in fig. 2.3a.

2.3.2 Dielectric Waveguides

The first part of this section will cover *planar* dielectric waveguides as an intermediate step before moving on to discussing *rectangular* waveguides.

2.3.2.1 Planar Dielectric Waveguides

Many of the principles for planar mirror waveguides also apply to planar dielectric waveguides, albeit typically in a more elaborate form. One of the most immediate differences, is the concept of a critical angle, θ_c . The critical angle is the largest angle θ that allows for total internal reflection (TIR) within the waveguide, which is governed by Snell's law [10],

$$n_1 \sin \theta_1 = n_2 \sin \theta_2, \quad (2.33)$$

see fig. 2.5 for an illustration. When no transmission occurs across the boundary, i.e. when $\theta_2 = \pi/2$ and only reflection is the case, TIR occurs. The incident angle θ_1 is then denoted the critical angle θ_c , and

$$\sin \theta_c = \frac{n_2}{n_1}. \quad (2.34)$$

The propagation itself is also different for dielectric waveguides, due to the fact that the reflection-induced phase delays ϕ_\downarrow and ϕ_\uparrow become dependent on the refractive index contrasts at the boundaries of the waveguide core. For completeness, it can be shown that for a TE-wave, the

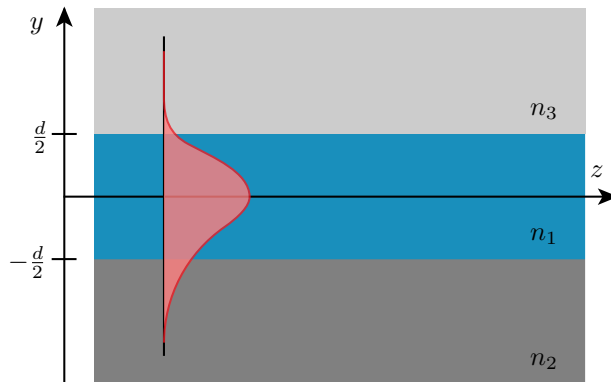


Figure 2.7: Asymmetric planar waveguide, in which the blue area denotes the waveguide structure, the dark gray area denotes the bottom cladding (substrate), and the light gray area denotes the top cladding (e.g. air). In the figure, $n_1 > n_2 > n_3$, and a schematic of the field distribution of the first mode is inserted. Notice how the evanescent field does not penetrate as far into the top cladding, due to the larger index contrast.

induced phase shift from a reflection is given by [16]

$$\phi_{\text{TE}} = 2 \arctan \left[\frac{\sqrt{\sin^2 \theta' - (n_2/n_1)^2}}{\cos \theta'} \right], \quad (2.35)$$

where $\theta' = \pi/2 - \theta$ is the complement of θ (as θ is given in fig. 2.3a), n_1 is the refractive index of the core, and n_2 is the refractive index of the cladding.

Given a symmetric waveguide, the reflection phase shifts at both boundaries are equal, and the self-consistency requirement from eqn. 2.27 becomes

$$2n_1 k_0 d \sin \theta - 2\phi_{\text{TE}} = 2\pi m, \quad (2.36)$$

which can be solved for θ in order to find the propagating modes.

2.3.2.2 Evanescence

The boundary conditions for the electric field, as described by eqns. 2.5 and 2.7, require that the field is continuous. However, as the dielectric media surrounding the waveguide is not a perfect conductor (for which the tangential electric field would vanish, as depicted in fig. 2.3b), field components still exist even outside the waveguide structure itself, as depicted in fig. 2.6. These fields do however rapidly decay with the distance from the waveguide boundary, and are therefore referred to as **evanescent fields**.

2.3.2.3 Asymmetric Waveguides

The waveguide structure used in this project is a Si-on-SiO₂ (or silicon-on-insulator, SOI) type waveguide, with no particular top cladding (i.e. air). Because SiO₂ and air have different refractive indices, the waveguide may in fact be categorized as an **asymmetric waveguide**, as depicted in fig. 2.7. The field distribution of an asymmetric waveguide will differ from that of a symmetric one (see fig. 2.6), as the higher index contrast between Si and air will lead to a greater confinement of the field at the air-Si interface, as compared to the Si-SiO₂ interface.

The asymmetry between the boundaries in the waveguide also has an effect on the supported propagation modes. Since the boundary conditions are different, so too are the requirements for

TIR at the boundaries. The self-consistency equation thus gets a little more complicated[16];

$$2n_1 k_0 d \sin \theta - \phi_{\text{TE},12} - \phi_{\text{TE},13} = 2\pi m, \quad (2.37)$$

where

$$\phi_{\text{TE},ij} = 2 \arctan \left[\frac{\sqrt{\sin^2 \theta' - (n_j/n_i)^2}}{\cos \theta'} \right] \quad (2.38)$$

is the phase shift due to reflections at the boundary between medium i and j . Eqn. 2.37 can be solved to find the supported modes, and, naturally, the largest critical angle θ_c of the two boundaries will determine the critical angle of the waveguide in total.

2.3.2.4 Effective Refractive Index

The propagation constant β describes the rate of propagation in the z -direction, and as such, an *effective refractive index* n_{eff} might be defined as

$$\beta = n_1 k_0 \cos \theta = n_{\text{eff}} k_0, \quad n_{\text{eff}} = n_1 \cos \theta. \quad (2.39)$$

In essence, this models the propagating mode as one that does not bounce, but rather travels only in the z -direction. The value of n_{eff} is determined by the refractive indices of the surrounding media, and in the case of air being the top cladding (see fig. 2.7), it can be shown that [16]

$$n_1 \geq n_{\text{eff}} \geq n_2. \quad (2.40)$$

2.3.2.5 Coupling Between Waveguides

The evanescent field enables a highly useful feature in waveguide optics, namely **waveguide coupling**; two waveguides in proximity (such that the evanescent fields are able to extend into the adjacent waveguide core) may be able to transfer optical power between the waveguides. This effect can be used to create optical couplers, splitters, switches and more[17, 18], and is a key component to optical ring resonators, as will be discussed in section 2.4. The principle behind waveguide coupling is shown in fig. 2.8b.

Coupled mode theory describes the (weak) coupling between two waveguides, assuming that the mode in each waveguide is "oblivious" of the modes in the other waveguides. This coupling can be described by a set of equations considering the amplitudes in (subscript i) and out (subscript o) of the coupling region (see fig. 2.8a), which can be written as [10]

$$\begin{bmatrix} E_{o1} \\ E_{o2} \end{bmatrix} = \mathbf{T} \begin{bmatrix} E_{i1} \\ E_{i2} \end{bmatrix}, \quad (2.41)$$

where \mathbf{T} denotes the transmission matrix of the system, which for identical waveguides (as depicted in fig. 2.8b) is given as

$$\mathbf{T} = \begin{bmatrix} A(z) & B(z) \\ C(z) & D(z) \end{bmatrix} = \begin{bmatrix} \cos \mathcal{C}z & -j \sin \mathcal{C}z \\ -j \sin \mathcal{C}z & \cos \mathcal{C}z, \end{bmatrix} \quad (2.42)$$

in which \mathcal{C} is the coupling coefficient. The power exchange between the two waveguides is periodic in z .

An important parameter regarding coupling, is the coupling length L_0 . L_0 is defined as the propagation distance over which the optical power has transferred completely from one waveguide to another. A 50/50 beam splitter (often referred to as a 3dB coupler) may for example be made by two parallel waveguides that are allowed to couple over a distance of $L_0/2$.

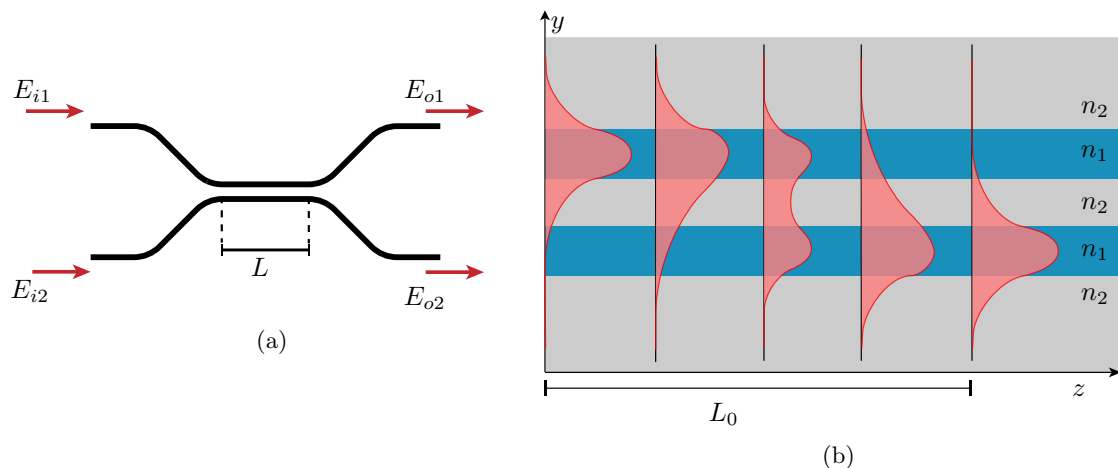


Figure 2.8: a) Schematic of waveguide coupling. The distance L may be adjusted to provide e.g. full transfer of power between the waveguides, or a 50/50 split in power. b) Mode distribution in two coupling waveguides. After a distance L_0 the field distribution has completely coupled into the other waveguide. L_0 is referred to as the coupling length. The power transfer is periodic, so after an additional L_0 of propagation, the field will have coupled back into the upper waveguide. Figure b) is adapted from [10].

2.3.2.6 Rectangular Dielectric Waveguides

A rectangular dielectric waveguide is a waveguiding structure comprised of a dielectric material (core) with a rectangular cross-section, typically immersed or partially covered by another dielectric medium (cladding) of a lower refractive index. Three common configurations are shown in fig. 2.9. As the waveguide no longer can be considered infinite in the x -direction, restrictions in the supported modes also arise due to the finite width in x . Thus, a supported mode in a rectangular waveguide is described by two indices, m and n , and any particular TE mode would be denoted TE_{mn} . The cut-off frequency of a TE wave in a rectangular waveguide is given by [11]

$$\nu_{c,mn} = \frac{c}{2} \sqrt{\left(\frac{m}{a}\right)^2 + \left(\frac{n}{b}\right)^2}, \quad (2.43)$$

in which a is the width of the waveguide, and b is the height. For TE-modes, *either* m or n can be zero, but not both at the same time.

For a waveguide whose width a is greater than its height b , the dominating mode will be the TE_{10} mode, as it has the lowest cut-off frequency. This mode also has the lowest attenuation, which is why it is beneficial to use single-mode waveguides in low-loss applications. From eqn. 2.43, it is clear that $\nu_{c,10}$ reduces to eqn. 2.32 as a denotes the thickness of the waveguide core in the y -direction. The TE_{20} mode has the second-lowest cut-off frequency, given as $\nu_{c,20} = c/d = 2\nu_{c,10}$. Single-mode operation of the waveguide is achieved by tailoring the thickness (height) of the waveguide structure in such a way that $\nu_{c,10} < \nu_{sig} < \nu_{c,20}$.

2.3.3 Input Coupling

For an optical waveguide to be useful (i.e. guide any light signal), light must be coupled into the waveguide structure. There exists a variety of different techniques for achieving this, the conceptually simplest being so-called *butt coupling*. Butt coupling simply involves directly focusing light into one end of the waveguide, typically using a focusing lens. The transverse distribution of the incident light must match that of a supported mode in the waveguide, as must the polarization [10].

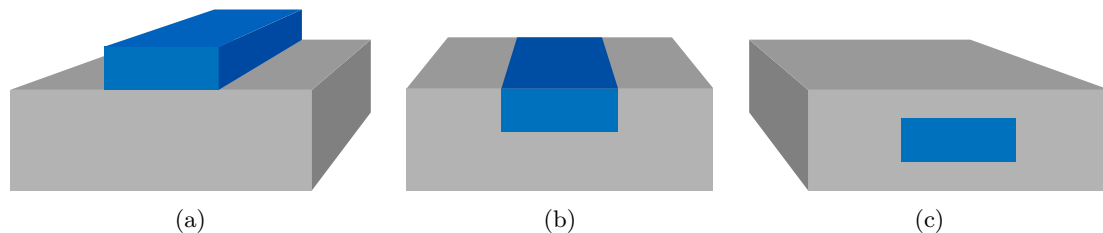


Figure 2.9: Different waveguide configurations: a) strip (or ridge) waveguide, b) embedded-strip waveguide and c) immersed-strip waveguide. The core is denoted by the blue color, while the cladding is shown in gray.

While butt coupling is simple in principle, the technique is rather difficult in practice, due to the precise alignment required. Since the waveguide cross-section has very small dimensions, it is challenging to perfectly match the incident light distribution to the waveguide, and as a result, the coupling using this technique is rather inefficient. *Insertion loss* can be defined as the total loss that occurs between insertion and extraction of light from an optical device[19], and can be modeled as

$$\alpha_{\text{insertion}} = \alpha_{\text{coupling}} + \alpha_{\text{prop}}L, \quad (2.44)$$

where α_{coupling} is the loss due to the coupling, and $\alpha_{\text{prop}}L$ is the propagation loss over an optical path length L , due to the waveguide itself.

For a typical single-mode fiber waveguide to strip waveguide coupling, the coupling efficiency is in the order of only 0.1 % [20]. In laboratory settings, where the input laser power may be far higher than what is required, this poor efficiency does not necessarily matter for the function of the waveguide itself. It does however play an important part in the design of an eventual end-user product, where the capabilities of the laser source could be a major factor in the overall price of the product.

2.3.3.1 Inverted Tapers

A special technique called *inverted tapering* can be used to increase the coupling into the waveguide. This technique is based on using a very narrow waveguide, slowly increasing in width, while being clad in a polymer material with a relatively large cross-sectional area, see fig. 2.10. The narrowing tip of the waveguide slowly causes the mode to expand into the polymer cover[21], thus matching better with the mode size from the input fiber. Inverted tapers also assist in the alignment of the input light, as the polymer has a significantly larger cross-sectional area than the waveguide core itself. Inverted tapers have shown good performance[22] with low coupling losses[23], and some even reporting losses lower than 1 dB[24].

2.3.4 Loss in Waveguides

Waveguide structures suffer from multiple sources of loss; some being inherent in the waveguide materials themselves, while others are due to the fabrication process involved in the making of the waveguide. Moreover, the design of the waveguide structures itself may also have an effect on the loss, as the changing geometry of the waveguide might induce e.g. undesirable reflections.

Bulk material absorption can be caused by many mechanisms, including band-to-band transitions and so-called dangling bond absorption[25]. Silicon is transparent to light in the telecommunications wavelength range (1300–1600 nm), and particularly crystalline Si provides very low loss[26, 27]. Amorphous Si (a-Si) is also transparent, however due to the non-crystalline structure, a-Si suffers from losses due to dangling bonds[19]. Dangling bonds are non-satisfied bonds of Si-atoms, which act as sites in which photon absorption may occur. The effects of these dangling bonds can be mitigated by hydrogenating the silicon (i.e. introducing hydrogen in the fabrication

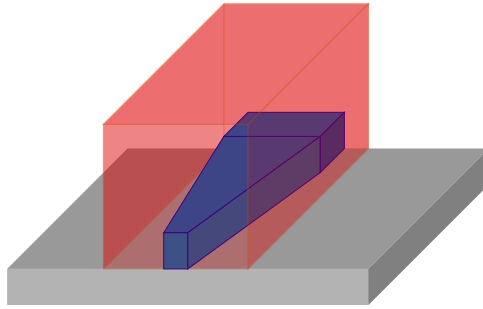


Figure 2.10: Schematic of an inverted taper input coupler. The tapered waveguide is colored in blue, while the polymer overlay is colored red. The cross-section of the polymer is a significantly larger area than the waveguide endface, and thus simplifies the input alignment and subsequent in-coupling.

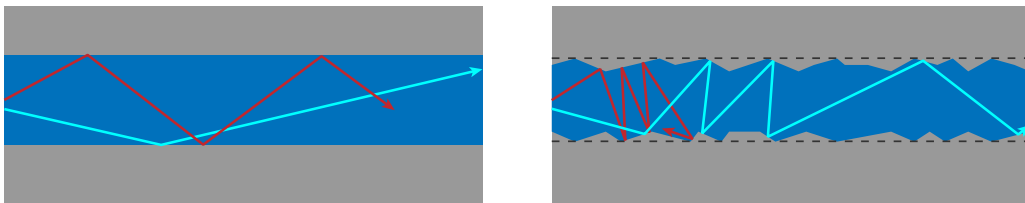


Figure 2.11: Illustration of the effects of sidewall roughness in waveguides. Left: Perfect sidewalls provide no scattering of the propagating light. Right: The uneven sidewalls scatter the light propagating in the waveguide, causing increased loss. The roughness in this figure is greatly exaggerated for illustrative purposes.

process)[28].

In SOI waveguides, the two main sources of loss are sidewall roughness and leakage into the SiO_2 substrate[29, 30]. Sidewall roughness is illustrated in fig. 2.11, and is typically a result of the lithography patterning process and/or the subsequent etching process. Sidewall roughness may be reduced by various optimizations, both to the patterning as well as to the post-processing methods[31, 32], where thermal oxidation is a common approach of the latter kind. Substrate leakage is inevitable in SOI waveguides due to the extent of the evanescent field into the SiO_2 substrate, as is illustrated in fig. 2.7. The leakage is a function of the waveguide width[33], with smaller widths typically leading to increased loss.

The waveguide structure design itself may also affect the loss in waveguide structures, as multiple sharp bends can induce undesirable radiation loss. In general, the propagation losses related to a waveguide bend is greatly linked to the radius of the bend itself[30], so extra care must be taken when designing photonic integrated circuits (PICs) with multiple bends. However, for SOI structures, the large light confinement allows for very sharp turns, which enables the fabrication of highly compact PICs. Low-loss waveguide bends (90° turns with loss < 0.1 dB/cm) with radii of as small as $1 \mu\text{m}$ have been fabricated and described in the literature[34].

2.4 Optical Resonators

Optical resonators confine and store light, and come in a wide variety of configurations[35], with equally varying properties. Resonators can be used for measurement applications as well as for storing and/or delaying light, e.g. in laser applications.

In this section, we will investigate the simplest form of resonator, namely the Fabry-Perot resonator, as many of the principles are simple to comprehend in this configuration. Following this, we will take a look at ring resonators, as they play a key role in the operation of the MARC

sensor in this project.

2.4.1 Fabry-Perot Resonator

The Fabry-Perot (FP) resonator is arguably the simplest form of 1-dimensional optical resonator, as it only consists of two parallel mirrors. The light is reflected back and forth between the mirrors, and thus optical energy is stored within the resonator.

Analogously to the y -component of the modes of a planar parallel-mirror waveguide, the modes supported by the resonator will be standing waves within the resonator cavity, with the field being zero at the mirror boundaries. Thus, for a resonator with a fixed distance d between the mirrors, only certain frequencies/wavelengths are supported in the resonator. This gives rise to a frequency spacing of the supported modes, which is called the **free spectral range**, FSR, and is given as [10]

$$\text{FSR}_\nu = \frac{c_0}{2nd}. \quad (2.45)$$

The free spectral range can also be expressed in terms of wavelength, i.e.

$$\text{FSR}_\lambda = \frac{\lambda_0^2}{2nd}. \quad (2.46)$$

n denotes the refractive index of the medium in the FP resonator. The free spectral range is a useful parameter for a resonator, and from the expressions it is clear that a shorter distance d results in a larger FSR. The desired FSR depends upon the actual application of the resonator in question.

For an ideal FP resonator, the mirrors are lossless, and only the exact resonance frequencies denoted by eqn. 2.45 are sustained in the resonator. In a real case, however, losses in the resonator introduce broadening of the resonances that are supported. This broadening is determined by the so-called **finesse**, \mathcal{F} , which is given as

$$\mathcal{F} = \frac{\pi\sqrt{|\alpha|}}{1-|\alpha|}, \quad (2.47)$$

in which $|\alpha| \in [0, 1]$ is the magnitude of the round-trip attenuation factor [10]. The connection to the broadening is given by

$$\delta\nu \approx \frac{\text{FSR}_\nu}{\mathcal{F}}, \quad (2.48)$$

as long as \mathcal{F} is sufficiently large. The full width at half maximum (FWHM) value is a measure of the broadness of the peaks, and is given as

$$\text{FWHM}_\nu = 2\delta\nu. \quad (2.49)$$

A third parameter called the **quality factor** (or simply Q-factor) is a measure of the resonator's ability to store energy. The Q-factor is thus related to the losses in the resonator, and also to the finesse. An approximation for the Q-factor is given by

$$Q \approx \frac{\nu_0}{\text{FSR}_\nu} \mathcal{F}, \quad (2.50)$$

where ν_0 is the resonance frequency of the resonator.

2.4.2 Ring Resonators

In essence, a ring resonator is simply a closed-loop (circular) waveguide in which electromagnetic waves can propagate. This structure would however not be particularly useful on its own, and

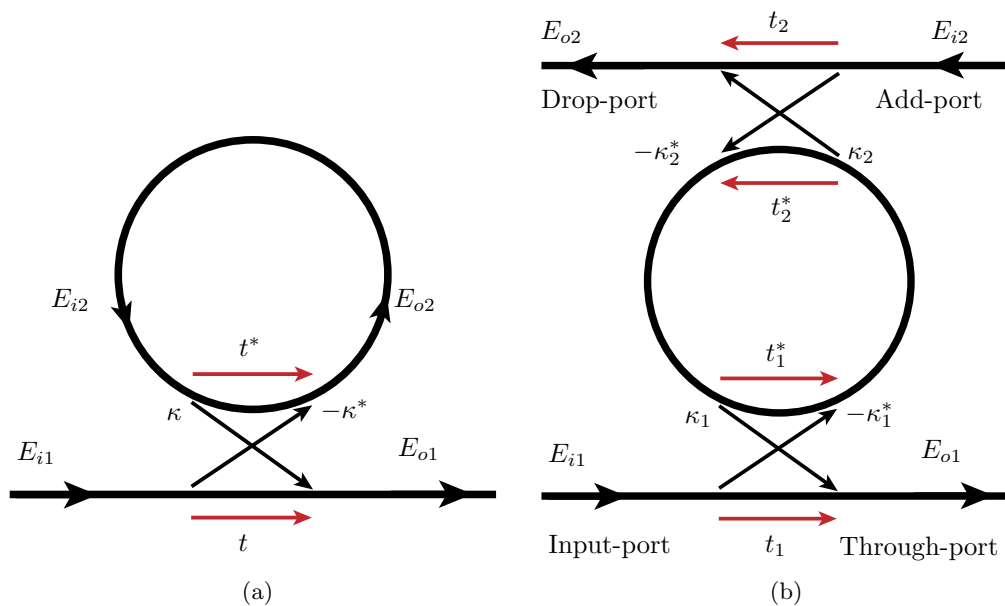


Figure 2.12: The working principles of a) an all-pass ring resonator and b) an add-drop ring resonator. The figures are adapted from [36].

typically one or two straight waveguides are placed in proximity to the ring waveguide, enabling in- and out-coupling of light. Large portions of the following argumentation follow that of [36].

2.4.2.1 All-Pass Ring Resonators

In the case of a single ring and one (bus) waveguide, the configuration is typically referred to as an *all-pass* resonator, or a *notch filter*, due to its filter characteristics. The following mathematical analysis of the ring resonator assumes that the coupling is lossless, and only a single polarization is considered.

The working principle of the all-pass configuration is shown in fig. 2.12a. The coupling from the waveguide to the ring is described by the complex parameter $-\kappa^*$, where the asterisk denotes the complex conjugate of κ , which is the complex coupling parameter describing the coupling from the ring into the bus waveguide. t is the coupling parameter describing the self-coupling of the waveguides. Mathematically the situation can be described by the matrix equation

$$\begin{bmatrix} E_{o1} \\ E_{o2} \end{bmatrix} = \begin{bmatrix} t & \kappa \\ -\kappa^* & t^* \end{bmatrix} \begin{bmatrix} E_{i1} \\ E_{i2} \end{bmatrix}, \quad (2.51)$$

which is on the same general form as eqn. 2.41. The parameters κ and t depend on the exact nature of the coupling mechanism (where particularly the distance between ring and bus waveguide plays an important role), and under the assumption of lossless coupling, we have

$$|\kappa|^2 + |t|^2 = 1. \quad (2.52)$$

For simplicity, attenuation has been assumed to be zero in fig. 2.12, but a *round-trip* attenuation factor¹ α can easily be introduced by letting

$$E_{i2} = \alpha e^{j\phi} E_{o2}, \quad (2.53)$$

where $e^{j\phi}$ represents the phase shift induced by the propagation through the ring (i.e. round-trip

¹I.e. the attenuation factor of one complete trip along the ring waveguide

phase shift), such that

$$\phi = n_{\text{eff}}k_0 \cdot 2\pi r, \quad (2.54)$$

in which r is the radius of the ring. n_{eff} is the effective refractive index of the ring.

For an all-pass filter, the most important aspect is arguably the transmission of the light that is input to the resonator structure. It can be shown[36] that solving eqn. 2.51 using eqn. 2.53 yields an expression for the output electric field as

$$E_{o1} = \frac{-\alpha + te^{-j\phi}}{-\alpha t^* + e^{-j\phi}} E_{i1}, \quad (2.55)$$

which leads to the intensity response

$$P_{o1} = |E_{o1}|^2 = \frac{\alpha^2 + |t|^2 - 2\alpha|t| \cos(\phi + \varphi_t)}{1 + \alpha^2|t|^2 - 2\alpha|t| \cos(\phi + \varphi_t)}, \quad (2.56)$$

under the assumption of $E_{i1} = 1$.

In this last equation, $t = |t|e^{j\varphi_t}$, where $|t|$ represents the coupling loss and φ_t denotes the phase imposed by the coupling. Resonance occurs when $\phi + \varphi_t = 2\pi m$, where m is an integer, at which point the cosines of eqn. 2.56 evaluate to 1. If the coupling has no phase term (i.e. $\varphi_t = 0$), resonance can also be seen as the condition of having the optical path length along the ring ($L_{op} = n_{\text{eff}}d$, where d is the circumference of the ring) equal an integer number of wavelengths, leading to constructive interference within the ring resonator.

A peculiar case occurs at resonance when $\alpha = |t|$ (i.e. the loss in the ring is equal to the coupling losses) in eqn. 2.56; the intensity transmission drops to zero. This phenomenon is called **critical coupling**, and occurs because of destructive interference between the field in the bus waveguide and the field coupled from the ring back into the waveguide. This is the reason all-pass ring resonators are called notch filters; they effectively filter out very narrow frequency bands (notches) from the input signal.

Free spectral range, finesse and quality factor are also applicable to ring resonator filters. Similarly to the Fabry-Perot resonator, we have [36]

$$\text{FSR}_\lambda = \frac{\lambda_0^2}{n_{\text{eff}}L}, \quad (2.57)$$

where $L = 2\pi r$ is the circumference of the ring (r being the radius of the ring). It is worth noting that this is only valid under the assumption that the effective refractive index is wavelength-independent², i.e. $n_g = n_{\text{eff}}$.

It can moreover be shown that, assuming weak coupling ($\kappa \ll 1$) [36]

$$\text{FWHM}_\lambda = \frac{\kappa^2 \lambda_0^2}{\pi L n_{\text{eff}}}, \quad (2.58)$$

and the finesse may be found as

$$\mathcal{F} = \frac{\text{FSR}_\lambda}{\text{FWHM}_\lambda} \approx \frac{\pi}{\kappa^2}, \quad (2.59)$$

where the last approximation is valid under the assumption of weak coupling. It is clear that a weaker waveguide-ring coupling coefficient κ (i.e. a higher waveguide self-coupling coefficient t), leads to a greater finesse. Finally, the Q-factor is given by \mathcal{F} as

$$Q = \frac{n_{\text{eff}}L}{\lambda_0} \mathcal{F}. \quad (2.60)$$

²In general, a more correct expression for the free spectral range is $\text{FSR} = \lambda_0^2/n_gL$, where $n_g(\lambda) = n_{\text{eff}}(\lambda_0) - \lambda_0 \partial n_{\text{eff}}/\partial \lambda$ is the *group refractive index*[37]

2.4.2.2 Add-Drop Ring Resonators

The same principles as above also apply to so-called add-drop ring resonators. An add-drop ring resonator consists of two straight waveguides coupled to a ring between the waveguides. This configuration has four ports, referred to as the input-, through-, add- and drop-ports, see fig. 2.12b. At resonance, signals may be "added" to the through-port signal via the add-port, and simultaneously "dropped" from the input-port via the drop-port.

For this project, the most interesting ports are the through-port and the drop-port, and the following analyses will consider no input to the add-port. The derivations are similar to those for the all-pass filter, although another coupler needs to be added in the analysis. It can be shown[36] that the through-port amplitude response is given by

$$E_{o1} = \frac{t_1 - t_2^* \alpha e^{j\phi}}{1 - t_1^* t_2^* \alpha e^{j\phi}} E_{i1}, \quad (2.61)$$

and that the drop-port amplitude response is given by

$$E_{o2} = \frac{-\kappa_1^* \kappa_2 \alpha_{\frac{1}{2}} e^{j\phi_{\frac{1}{2}}}}{1 - t_1^* t_2^* \alpha e^{j\phi}} E_{i1}. \quad (2.62)$$

$\alpha_{\frac{1}{2}}$ and $\phi_{\frac{1}{2}}$ denote the attenuation factor and phase delay, respectively, caused by propagating half of the ring resonator circumference.

The phase response of the add-drop configuration is readily extracted via calculating the argument ($\arg(A) = \arctan(\text{Im}\{A\}/\text{Re}\{A\})$) of the complex-valued amplitude responses from these two equations, i.e. the phase response at the through-port is

$$\Phi_{\text{tp}} = \arg(E_{o1}), \quad (2.63)$$

and similarly the phase response at the drop-port is

$$\Phi_{\text{dp}} = \arg(E_{o2}). \quad (2.64)$$

Critical coupling is achieved when $\alpha = |t_1/t_2|$ [36], and thus for symmetrical coupling, a lossless ring is required ($\alpha = 1$). If critical coupling is fulfilled at resonance, the intensity at the through-port drops to zero, while at the drop-port the intensity increases to unity. See fig. 2.13 for an illustration of this transmission response.

2.4.2.3 Non-Parallel Add-Drop Ring Resonators

Conventional add-drop ring resonators typically have parallel bus waveguides, however that need not be the case. The drop-port waveguide may very well have an arbitrary angular separation θ , as is displayed in fig. 2.14. In the case of identical and symmetrical coupling with no phase term, i.e., $t = t_1 = t_2 \in \mathbb{R}$, eqns. 2.61 and 2.62 simplify somewhat into

$$E_{o1} = \frac{t - t\alpha e^{j\phi}}{1 - t^2 \alpha e^{j\phi}} E_{i1} \quad (2.65)$$

and

$$E_{o2} = \frac{-(1 - t^2)\alpha_{\theta} e^{j\phi_{\theta}}}{1 - t^2 \alpha e^{j\phi}} E_{i1}, \quad (2.66)$$

where we have employed eqn. 2.52. α_{θ} and ϕ_{θ} denote the attenuation factor and the phase delay respectively, arising from the actual traversed proportion of the ring circumference, as decided by

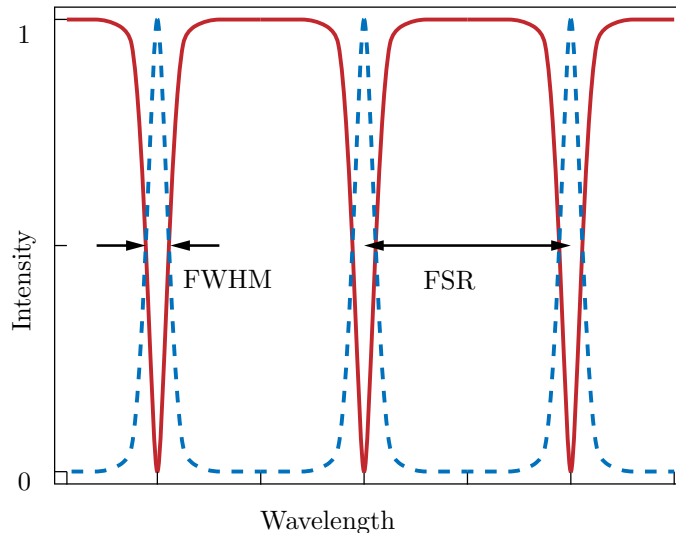


Figure 2.13: The transmission response of an add-drop ring resonator under critical coupling. The solid line denotes the through-port transmission, and the dashed line denotes the drop-port transmission. The free spectral range (FSR) is the separation between resonant wavelengths, and the full-width at half-maximum (FWHM) describes the sharpness of the resonance peaks.

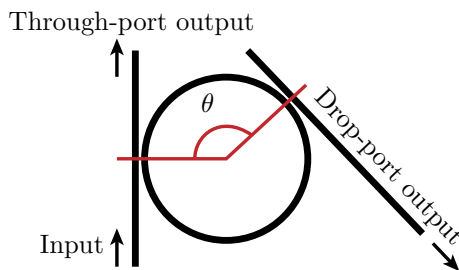


Figure 2.14: Schematic showing the angular separation θ between through-port and drop-port. This figure is adapted from [3].

θ . In relation to their round-trip counterparts, α and ϕ , we have

$$\alpha_\theta = \alpha^{\theta/360^\circ}, \quad \text{and} \quad \phi_\theta = \phi \cdot \frac{\theta}{360^\circ}, \quad (2.67)$$

where θ is in degrees.

While the transmission response of the ring resonator is not affected by the angular separation θ , the drop-port phase response is. In fact, the accumulated phase between resonances is equal to the angular separation[3], meaning that for a parallel add-drop resonator (with angular separation of 180° , or π radians) the phase accumulated at the drop port between resonances is π . A smaller angular separation results in less phase accumulation, and vice versa, and this phase response plays a key role in the so-called MARC sensor.

2.5 MARC Devices

Mach-Zehnder interferometer-assisted ring resonator configuration (MARC) devices are comprised of a balanced MZI and one (or more) add-drop ring resonators[3]. The drop-port of the ring(s) might be placed at an arbitrary angular separation, and this angle will strongly affect the transmission spectrum of the device. Carefully selecting the angular separations of each ring, along

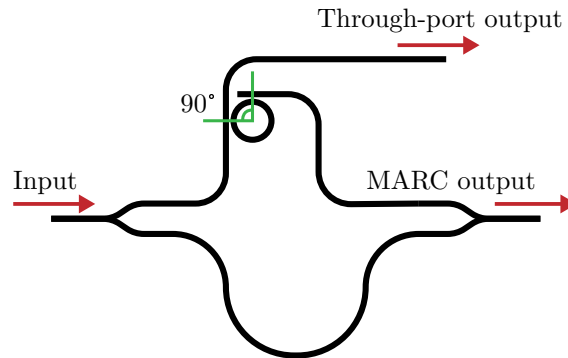


Figure 2.15: Simple schematic of a single-ring MARC sensor with 90° angular separation.

with the size of each ring, allows for the output transmission spectrum from the device to be of a certain shape, thereby effectively increasing the sensor range and/or allowing for multiplexing of the signals from the individual rings.

The simplest MARC devices are comprised of a balanced Mach-Zehnder interferometer, in which one of the interferometer arms are connected to an add-drop ring resonator, see fig. 2.15. The drop-port signal is then recombined with the other interferometer arm at the output of the device. The task of the Mach-Zehnder interferometer itself is to convert any phase differences introduced by the ring resonator into a detectable intensity response.

This enables a particularly useful feature, which is the concept of the **effective free spectral range**, FSR_e . The free spectral range is determined by the range of wavelengths over which the accumulated phase from the ring resonator sums up to 2π , so by carefully choosing angular separations and ring sizes, the *effective* free spectral range can be several times larger than the FSR of the individual ring resonator. This is well described in [3], and the key takeaway is that the effective FSR is given as

$$\text{FSR}_e = N \cdot \text{FSR}, \quad (2.68)$$

where N is given by the angular separation θ as

$$\theta = 2\pi \frac{M}{N}, \quad (2.69)$$

where N, M are integers. The fraction M/N must be an irreducible fraction, and the value M does not have any impact on the effective FSR. A few examples may help with the understanding:

- 90° angular separation: $\theta = \pi/2 = 2\pi M/N \implies 1/4 = M/N \implies N = 4$
- 135° angular separation: $\theta = 3\pi/4 = 2\pi M/N \implies 3/8 = M/N \implies N = 8$
- 180° angular separation: $\theta = \pi = 2\pi M/N \implies 1/2 = M/N \implies N = 2$
- 270° angular separation: $\theta = 3\pi/2 = 2\pi M/N \implies 3/4 = M/N \implies N = 4$

The MARC sensor requires that the MZI is *balanced*, i.e. both interferometer arms must be equal in optical path length. This length does however *not* include any path lengths related to the ring resonator itself, so special care must be taken when balancing the interferometer of the MARC. This balancing is not necessarily reflected in the schematics in figs. 2.15 and 2.16.

2.5.1 Resonance Lineshapes

Two resonance lineshapes are common in the transmission spectra of MARC devices, namely Lorentzian and Fano lineshapes. Only the qualitative principles of the two lineshapes will be presented in this section.

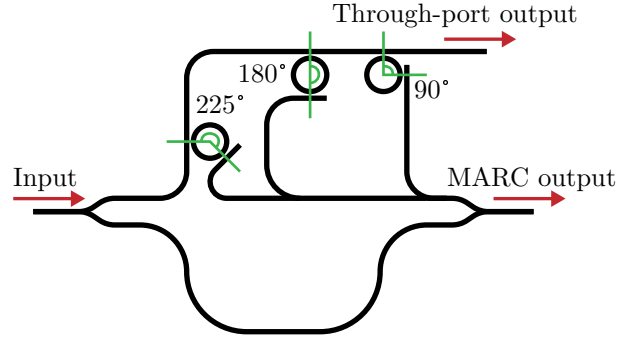


Figure 2.16: Schematic of a three-ring MARC device (multiplexed MARC) with angular separations of 225, 180 and 90 degrees. The through-port of one ring filter acts as the input port to the next ring, and the drop port signals are finally combined before being mixed with the signal from the other arm of the interferometer.

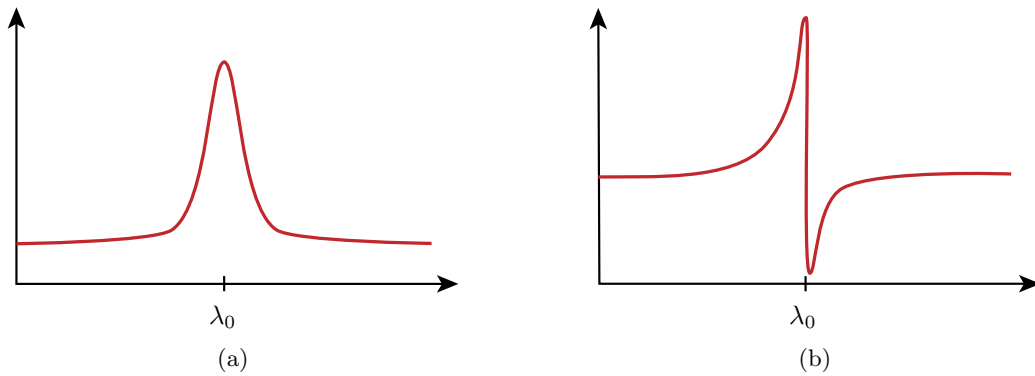


Figure 2.17: a) The Lorentzian lineshape is symmetrical around the resonant wavelength. b) Fano lineshapes are highly non-symmetrical around the resonant wavelength

The Lorentzian lineshape is a resonance response that is symmetric around the resonance wavelength, see fig. 2.17a. The Lorentzian lineshape commonly appears in situations related to photon absorption/emission and resonant behavior[10]. Fig. 2.18 illustrates inverse Lorentzian lineshapes.

The Fano lineshape is on the other hand highly asymmetric around the resonance wavelength, as is seen in fig. 2.17b. This behavior originates due to interference effects between a resonant signal and a background signal[38].

2.6 Multiplexing MARC Sensors

The standard MARC devices feature a single add-drop ring resonator, but more rings may be added to the device. This enables the multiplexing of the individual rings in the multi-ring MARC (multiplexed MARC), which in turn allows for applications in which different measurements may take place simultaneously. The number of rings as well as their individual sizes and angular separations all determine the final output spectrum of the multiplexed MARC, so care must be taken when designing the multiplexed MARC sensor for real world usage in terms of noise, signal loss as well as the ability to de-multiplex the signal from the MARC sensor. This aspect is indeed the main focus of this project, and will be discussed later.

An example of a three-ring multiplexed MARC is shown in fig. 2.16. In multiplexed MARC sensors, the through-port of the first ring acts as the input-port to the second ring (and so on), and all drop-port responses are combined at the output. This allows for the properties of all rings

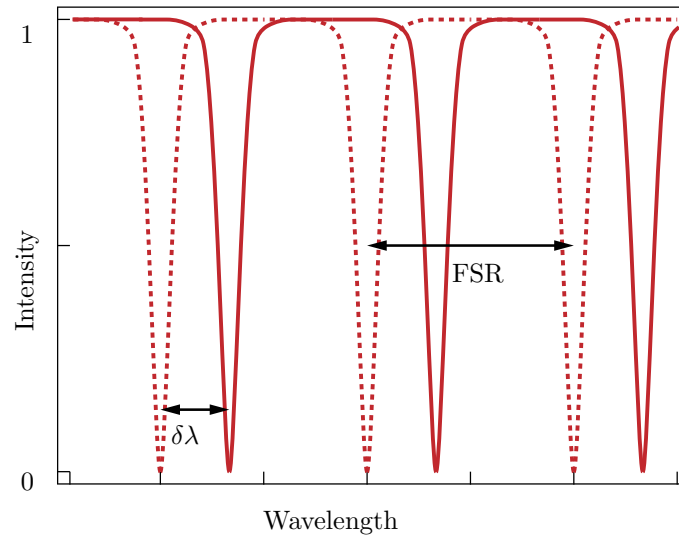


Figure 2.18: All-pass ring resonator transmission response before (dotted line) and after (solid line) an external factor has affected the effective refractive index of the ring waveguide. Shifts $\delta\lambda$ that are greater than the FSR cannot be resolved.

to contribute to the transmission spectrum of the entire device.

2.7 Ring Resonators as Sensors

As previously stated, the optical path length of a waveguide depends on the (effective) refractive index of the medium, and thus any change in refractive index represents a change in the optical path length. For a ring resonator subjected to a change in its effective refractive index, the resonant wavelength will thus shift, as the criterion for resonance also changes (as was briefly explained in section 2.4.2.1). The shift in resonant wavelength can be denoted $\delta\lambda$, and the principle is illustrated in fig. 2.18. There are several external factors that can change the effective refractive index of such a ring resonator, including temperature[39], externally applied electric fields[40] and adsorption of molecules to the ring waveguide itself[41]. The MARC sensor is intended to utilize this latter phenomenon for its label-free biosensing applications.

From fig. 2.18 it is also imminent that shifts in wavelength surpassing the FSR of the ring cannot be properly resolved, as the transmission spectrum repeats itself. The effective FSR of a single-ring MARC sensor works to extend this range, resulting in the capability of measuring over a larger dynamic range, which is one of the most important benefits of the MARC sensor.

Chapter 3

Methods

This chapter will cover the main methods used for the simulation work and data processing, as well as the experimental work performed in this thesis. The simulation work has been conducted using the simulation software *COMSOL Multiphysics 5.4 / 6.0* (COMSOL)¹, which is a commercially available finite-elements method (FEM) based software. COMSOL provides a wide variety of physics modules, which can be coupled together for powerful multiphysics simulations capable of modeling and solving complex physical problems.

The *Python 3.9* (Python) programming language² has been used for providing theoretical, idealized calculations of the transmission responses of the waveguide structures, as well as being used for writing several scripts for processing and plotting the simulation data from COMSOL.

For the experimental methods, descriptions of the working principles of the relevant fabrication and characterization tools will be presented. These descriptions will however be kept rather brief, as the techniques are well documented in the literature and not the main focus of this thesis.

Parts of this chapter are greatly based on the similar sections in chapter 3 of [1], as the simulation work in that project was similar to the work done in this thesis.

3.1 Python Programming

The main use of Python programming has been to process and present the data from the COMSOL simulations. COMSOL does in fact come with some tools of its own for plotting the simulation data, however these methods are not very flexible or customizable, as well as being rather computationally heavy. Instead, the Python package *Matplotlib*³ was used to present the data as seen in this thesis.

Moreover, theoretical and highly idealized calculations ("simulations") of the sensor structures have been performed. The main benefit of these simulations is their calculation speeds (in the order of only a few seconds), as they can quickly provide insight into e.g. possible MARC configurations for multiplexing, or for comparing simulation results with their ideal counterparts.

The ideal simulations are rather straightforward: An input signal of amplitude $E_{i1} = 1 \text{ V/m}$ and phase $\varphi = 0$ is used to calculate the through-port and drop-port transmission responses of the ring resonator using eqns. 2.65 and 2.66, respectively. The complex through-port output from one ring can then simply be used as the input for the next ring, allowing for the cascading of virtually infinitely many rings, while the complex drop-port responses are summed before finally being put into the interference equation (eqn. 2.24), where a phase difference may be added to see the effects of an unbalanced interferometer. Thus, the transmission response of the entire MARC structure is calculated. The model is quick to compute, and all relevant sensor parameters can be adjusted (including ring radius, wavelength range, effective refractive index, ring angular separation, self-coupling coefficient of the waveguides, and loss coefficient in the ring), however it does only replicate "perfect conditions", i.e. a perfectly balanced interferometer with critical coupling and no undesired waveguide reflections present. Furthermore, all wavelength dependencies and phase delays of the 3dB couplers at the input and output of the interferometer are assumed to be zero,

¹<https://www.comsol.com/comsol-multiphysics>

²<https://www.python.org/>

³<https://matplotlib.org>

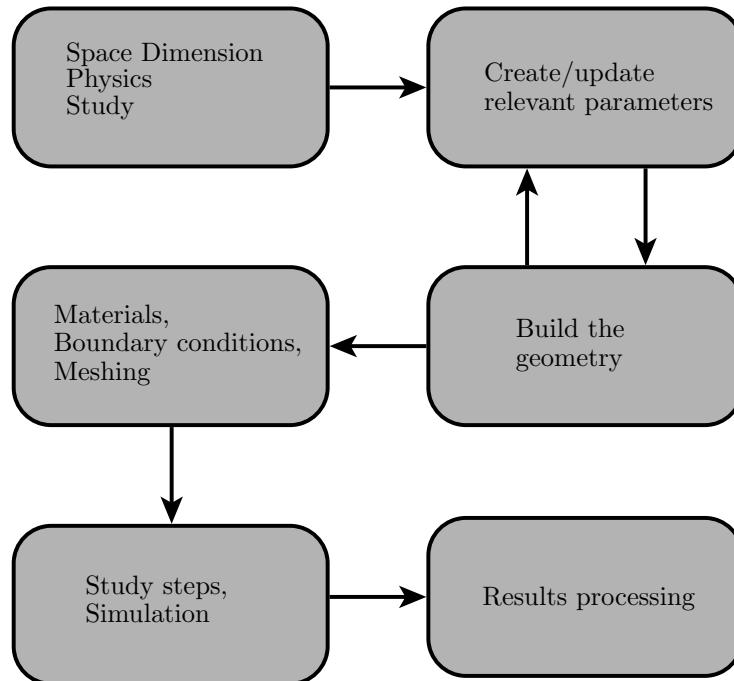


Figure 3.1: Illustration of a typical COMSOL workflow. The dimensionality, physics, and the study are set initially, before parameters are defined. Then the geometry may be defined, and once finished, the domains may be assigned proper materials, boundary conditions, and mesh settings. Then the simulation is run by going through the study steps, and once complete, the results may be exported for further processing and plotting. It may be helpful to alternate between creating/updating parameters while building the geometry, as this can simplify the design process.

as is the refractive index wavelength dependence of the waveguide material.

The foundation for the model is a MATLAB⁴ script written by co-supervisor Mukesh Yadav. This script was translated into Python code and expanded upon by the author, and is presented in its entirety in Appendix B.

3.2 COMSOL Simulations

The user interface of COMSOL encourages a certain workflow to be followed when creating a model, which is illustrated in fig. 3.1. The first step is selecting the *Space Dimension*, i.e. how many dimensions the model should consider. Here there are possibilities from zero through three dimensions, as well as axisymmetric 1D and 2D spaces.

The next step is to define the *Physics* of the model. COMSOL provides a variety of different modules covering a wide field of physics, including electricity, acoustics, heat transfer, optics, and many more. Once (one or more) physics modules have been selected, a *Study* is chosen, which determines the set of equations to be solved in the system.

Once the physics and the study has been set up, *parameters* for the system may be added. These parameters are fully in the hands of the user, meaning that as many parameters as needed can be made, and they can take any numerical value. The parameters are also able to be used and manipulated in various steps in the solving process, for example if sweeping a certain parameter, or when defining the geometry of the model.

After the parameters have been defined, the *geometry* may be built, using a computer-aided

⁴<https://se.mathworks.com/products/matlab.html>

design (CAD) based approach⁵. This is typically a process where it is convenient to jump back and forth between creating relevant parameters for e.g. object sizes or coordinates, and actually creating new geometry objects. This keeps the design "modular", and makes for easy implementation of small adjustments to model parameters.

Next, the completed geometry may have different materials assigned to its constituent domains. COMSOL provides an extensive library of common materials, which includes several physical parameters, e.g. refractive indices, heat capacities, conductances, etc., however it is also trivial to implement custom, user-defined materials.

In order for the model equations to be solved, the correct boundary conditions need to be defined. This can be done in several ways, depending on the exact *Physics* and *Study*. Boundary conditions may also include input- and output ports to the system. If applied correctly, the proper boundary conditions may also aid in reducing the computation time of the system.

Prior to the actual solving of the model, the model geometry needs to be discretized (tessellated). COMSOL uses a finite-elements method (FEM) based approach, which works by dividing the model geometry into (finitely) small elements, in which the relevant physics are calculated. If a sufficiently fine tessellation is reached, the physics in each element may be assumed to behave linearly, which significantly simplifies the calculations. This process of tessellation is called *Meshing* in COMSOL, and is a highly critical step which requires a lot of attention. In general, more complex geometries require a finer mesh than simple structures.

The solution to the model itself is created according to the *Study steps* defined by the *Study* and the user. Automatic sweeps of parameters may be set up, and the results processing may be adjusted. Once the computation is finished, the results are by default presented in various plots, however the numerical results are easily exported from COMSOL, if external data processing is required or desirable.

3.2.1 Effective Mode Index Approximations

Simulations of proper three-dimensional structures can be extremely demanding in terms of computational requirements, however an approximation can be made by performing a so-called *effective mode index* analysis. This approach firstly considers the waveguide structure as a vertical slab system consisting of the substrate, waveguide core and top cladding, as if being a side view of the 3D model (under the assumption that the waveguide width is "infinite"). The substrate, core and top cladding layers are then assigned the proper refractive indices, and the system is solved for the effective refractive index of the lowest order mode supported in the structure. This effective refractive index may then be used consequently in 2D "top-down-view"-simulations of the complete system. The effective mode index is a very popular method for the analysis of rectangular dielectric waveguides[42]. The validity of the approximation is very good for low index-contrast structures, and while the method also is applicable for higher-contrast structures, the valid wavelength range is much smaller in this case[43].

3.3 Fabrication Tools

In a typical fabrication process, a multitude of various tools and procedures are used, some simpler than others. This section will present and briefly discuss the main tools used for the fabrication of the SOI waveguide structures used in this project, while skipping the details of the more trivial tools like hotplates, spin coaters, ultrasonic baths and wafer cleaver pliers. Do note that the fabrication procedure itself is not the primary focus of this thesis, and a detailed discussion of each tool is therefore beyond the scope of this thesis.

⁵For the advanced CAD user, COMSOL is in fact capable of importing various formats of CAD drawings. Using an external CAD software is recommended for complex designs.

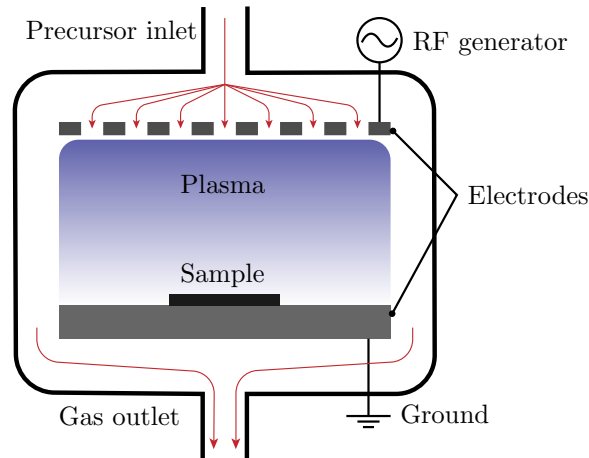


Figure 3.2: Schematic of a general PECVD chamber. Precursor gases are introduced to the chamber, and a plasma is formed due to an applied RF field. Chemical reactions take place near or on the sample surface as the thin film is deposited. This figure is adapted from [44] and [46].

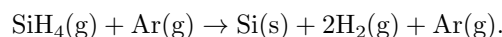
3.3.1 Plasma-Enhanced Chemical Vapor Deposition

Chemical vapor deposition (CVD) is the process of depositing a thin film on a wafer substrate through a chemical reaction of a gas mixture, while the wafer or its immediate vicinity is heated in order to drive the reactions at a faster rate. The precursor material is provided in a gas phase from an external source, and a chemical reaction at the surface of the substrate forms the thin film itself. Plasma-enhanced chemical vapor deposition (PECVD) is an extension of the CVD technique, in which plasma is used to create and sustain the CVD reaction. This lowers the required substrate temperature to 300-400°C, whereas a CVD typically operates at much higher temperatures[44, Ch. 11]. The precursor plasma is generated by an applied RF field (typically in the range 100 kHz - 40 MHz), and the process chamber (reactor) is kept at a low pressure (in the range of mtorr - torr)[45]. Although PECVD chambers exist in various forms, a general schematic is shown in fig. 3.2.

The properties of a PECVD-deposited film are highly dependent on several factors, including substrate temperature, power and frequency settings, gas composition, pressure, and flow rate. In general, PECVD provides high deposition rates, high film densities and good film adhesion to the substrate[44].

3.3.1.1 PECVD for Silicon Thin Film Deposition

In this project, PECVD is used to deposit amorphous silicon (a-Si). This process might use different combinations of precursor gases, however due to the availability of gases in the PECVD at NTNU NanoLab, the precursors were selected to be silane (SiH_4) and argon (Ar). While the chemical reactions occurring at a wafer surface in a PECVD are very complex[44], the key takeaway can be described by the net chemical reaction between the precursor gases for the process, namely



While a-Si inherently suffers from dangling bonds, the incorporation of hydrogen during the growth results in the passivation of the dangling bonds[47], in turn enabling waveguiding structures with lower losses. The reaction shown above gives gaseous hydrogen as a byproduct, which acts to hydrogenate the a-Si during the film deposition.

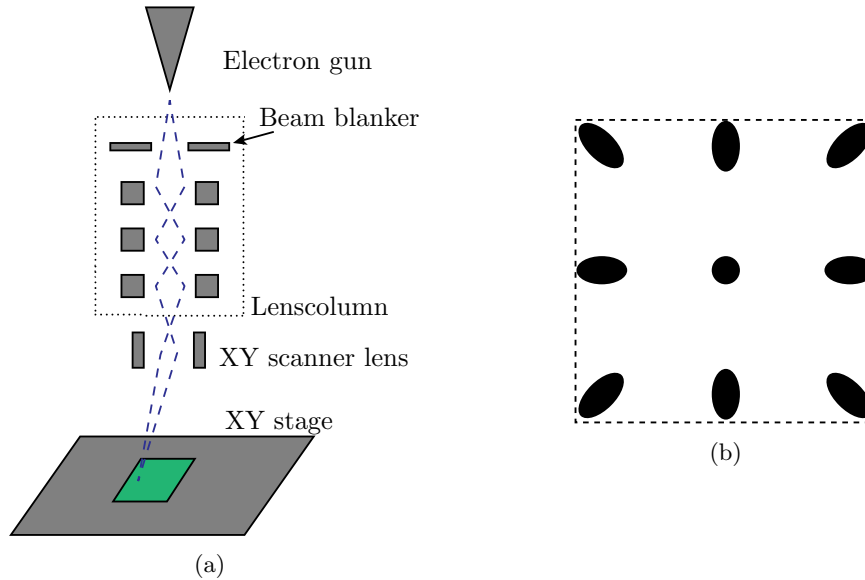


Figure 3.3: a) Schematic of an EBL. An electron gun generates a beam of electrons that is focused by various lenses in the lens column. A set of XY scanner lenses are used to deflect the beam in order to scan the write field (green area). The sample is secured to a repositionable XY stage, and a beam blaster is used to stop the electron beam from exposing the sample when the stage is moving. b) Beam cross-section at write field boundaries. In the center of the write field, the beam is focused and circular. Towards the edges of the write field, the beam shape is deformed and loses its focus.

3.3.2 Electron Beam Lithography

Electron Beam Lithography (EBL) is a very powerful lithography technique where an electron beam is focused and scanned over a special type of resist material (e-beam resist). The solubility of the resist during the development step is heavily dependent on the exposure to the electron beam, and due to the highly focused electron beam, nanometer-scale lithographic structures are readily achieved using EBL. The scanning nature of the electron beam also eliminates the need for a physical mask, allowing for arbitrary mask patterns. The immediate downside of EBL is the low throughput, as large, complex patterns require a significant total exposure time [48, Ch. 2].

A (highly simplified) schematic of an EBL is shown in fig. 3.3a. Note that the scanning of the electron beam is not achieved by movements of the XY stage, but rather by the XY scanner lens deflecting the beam itself. An EBL-pattern is therefore divided into so-called *write fields*, and the XY stage is only used to move the sample in between the exposure of each individual write field. The size of each write field is limited, however, as the beam bending causes aberrations in the shape of the beam as it hits the sample surface. This is illustrated in fig. 3.3b. Moreover, stochastic variations in XY stage movement, as well as rotations of the scanning field (due to sample surface height differences) [49] might contribute to errors in the alignment of each write field (*stitching errors*). The aberration effects towards the write field edges may be compensated for in software during exposure setup, and this is in some EBL systems referred to as *field correction*.

3.3.2.1 Pre-Exposure Preparation

A few steps of preparing the wafer substrate is required before an EBL exposure can be performed. Thorough cleaning of the wafer substrate is an essential first step, both to improve the resist-substrate adhesion, and to remove contaminants on the wafer surface. Various solvents may be used, including acetone and isopropanol (IPA). Solvent immersion may be paired with ultrasonic exposure in order to increase the cleansing effect.

Depending on the application and the mask design, either positive or negative (e-beam) resist may be used. Positive resist will turn soluble on exposure, meaning that the pattern of the mask will be the same as the pattern on the sample, whereas negative resist becomes insoluble after exposure, leaving a pattern on the sample that is opposite to the mask pattern[44].

To dispense the resist onto the wafer surface, a spin coater is used. Prior to the fabrication process, the proper spin coating parameters should be determined such that the desired resist layer thickness is achieved. These parameters depend on numerous factors, however for a given resist solution, the spin speed, spin speed acceleration (ramp), and the spin duration are the main influences on the resulting layer thickness.

Immediately following the spin coating, a soft bake is performed. The purpose of the soft bake is to drive off most of the solvent in the resist[44], however it also promotes the wafer-resist adhesion, and it is commonly done by the use of a contact hot plate.

3.3.2.2 EBL Exposure and development

After loading the sample into the EBL chamber, the desired EBL exposure is set up. This includes several parameters, including (but not necessarily limited to) beam current, beam size, beam stigmation and focus, exposure dosage, and write field size. Prior to the fabrication process, a dose test should be performed in order to find the process parameters that yield the desired resist film quality. The mask design is then loaded into the EBL controller software, and exposure can be commenced.

Using appropriate chemicals, depending on the exact brand and type of photoresist, the sample is after exposure developed, and lastly inspected in an optical microscope. The main role of the inspection is to verify that the exposed structures are as expected. In case of an unsuccessful exposure, any further fabrication should be terminated and adjustments to the process should be made.

3.3.3 Inductively Coupled Plasma-Reactive Ion Etching

Reactive ion etching (RIE) is a plasma-assisted dry etching technique that provides anisotropic etching action[50], using a combination of physical ion bombardment as well as chemical processes[51] in a low-pressure process chamber (reactor).

Inductively coupled plasma-reactive ion etching (ICP-RIE) is a certain flavor of RIE in which an inductive coil is connected to an RF generator (different from the electrode RF generator), see fig. 3.4. The inlet gases are excited into plasma by the magnetic field induced by the coil, and the bias set up between the electrodes transports the plasma towards the sample. Increasing the ICP power (i.e. power of the coil RF generator) increases the plasma density, and as a consequence, ICP-RIE is capable of achieving high etch rates[50]. Various process gases may be used in an ICP-RIE, however fluorine chemistry (e.g. SF_6 and CHF_3) is commonly used for etching shallow silicon structures[44].

The so-called *loading effect* needs to be considered when performing an ICP-RIE process, as the etching rate and depth may vary with the total surface area exposed to etching[52, 53]. This is because a larger sample (and thus a larger etch surface) will deplete the reactants faster than a smaller one[50]. The effects of loading can be alleviated by keeping the etch surface at a fixed area between each etch process, e.g. by using a 4" carrier wafer (of an etchable material) on which the smaller sample is secured.

3.3.4 Photolithography

Photolithography is the predecessor to EBL, and is naturally conceptually similar. The main difference is that photolithography, as the name implies, uses (typically near-UV) photons to

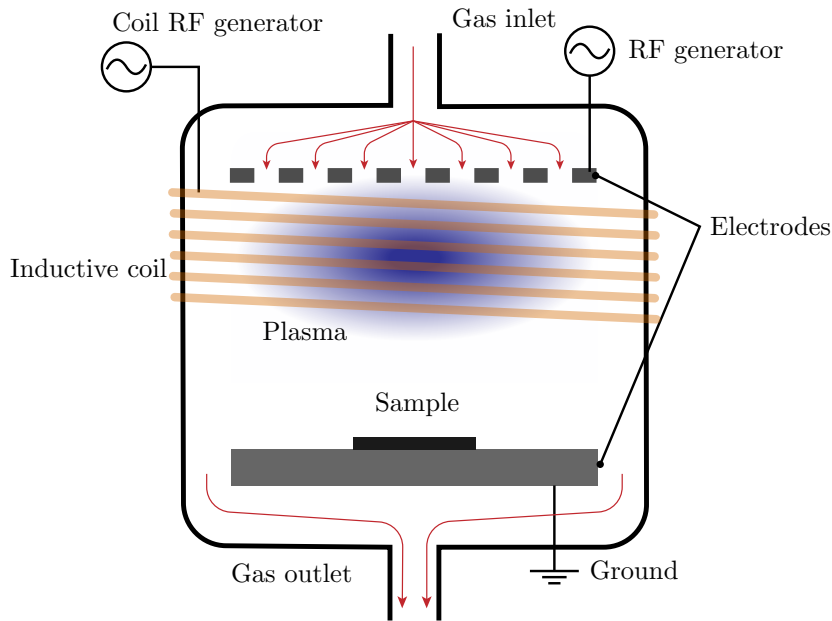


Figure 3.4: Schematic of a generic ICP-RIE. The inductive coil creates a plasma of the reactant gases, which is then used to anisotropically etch the sample on the bottom electrode.

expose the (photo)resist. The use of photons places larger limitations to the lithographic resolution than electrons (as with EBL), as the wavelength is much larger. For i-line lithography ($\lambda = 365 \text{ nm}$), for example, the resolution is limited to dimensions no smaller than $0.35 \mu\text{m}$ [44].

Photolithography does however have the advantage of much higher processing speeds than EBL, as the exposure may be done by illumination of the entire wafer, not being limited to a narrow, scanning beam[54].

3.4 Characterization Tools

During and after a fabrication process, it is common practice (and also highly useful) to inspect and characterize the sample, to verify that the process has been successful. For the type of fabrication described previously, optical microscopy and scanning electron microscopy are useful tools, and in the following subsections, these techniques will be briefly described.

3.4.1 Optical Microscope

Optical microscopes are useful for quick visual inspections after certain fabrication steps, particularly after development. Any major defects or deviations in the resist pattern can be discovered, and the further processing may be terminated. The resolution of such microscopes are limited, however, and during waveguide fabrication, they cannot be used to verify whether nanometer-range critical dimensions/features are within specification or not.

3.4.2 Scanning Electron Microscope

A scanning electron microscope (SEM) works very much like the electron beam system in an EBL does (or, rather, an EBL is a "modified" SEM): An electron gun provides a beam of electrons in a vacuum chamber, which is focused, formed and scanned over the sample surface by the use of several magnetic lenses[44]. A typical SEM is capable of magnifications of up to $300\,000\times$ [55],

and an experienced SEM operator is readily able to acquire images with resolution down to a few nanometers.

As the electron beam interacts with the sample, two types of signals may be read from the sample, namely *backscattered electrons* (BSE) or *secondary electrons* (SE). Backscattered electrons arise from elastic interactions between the sample and the beam, while secondary electrons arise from the atoms of the sample itself, as a result of inelastic interactions between the sample and the beam[56]. The former signal provides information about the atomic composition of the sample surface, with heavier atoms (relative to the other atoms in the sample) appearing brighter in the image. The latter signal, on the other hand, provides information about the topography of the sample surface[55].

Chapter 4

Experimental Procedures

This chapter will present the concrete procedures used in both the simulation work and the laboratory work in this thesis. The first sections will present the strategy behind the COMSOL simulation work, before the formation of the lithography mask design is briefly discussed. In the last sections, the experimental procedures used for fabricating the MARC sensor and the use of characterization tools are discussed. The main goal of the fabrication is to realize the sensor design from the simulation work in order to compare the results, as well as to be able to assess the feasibility of the sensor design.

4.1 COMSOL Simulation Work

In this section, the key rationales and ideas behind the COMSOL MARC model will be discussed. Moreover, the preliminary simulation work, such as the effective mode analysis, and the waveguide loss implementation procedures will be described. For the sake of brevity, the results from these preliminaries will also be presented immediately; they are not particularly interesting in themselves, however they play a large part in setting the parameters for the rest of the COMSOL simulations to follow.

The overall principles behind the COMSOL simulations are briefly described in section 3.2 and in the flow chart in fig. 3.1.

4.1.1 Physics and Study

For this project, the physics module *Wave Optics > Electromagnetic Waves, Frequency Domain* has been used, coupled with the *Wavelength Domain* study, to enable the calculation of propagating electromagnetic waves for different wavelengths. This was the module that met the requirements with the simplest configuration, for this particular project.

4.1.2 Effective Mode Index Analysis

Before the modeling and simulations of MARC devices, an effective mode index analysis was performed in COMSOL (see fig. 4.1 for an overview of the model geometry). A 1 μm layer of SiO_2 was modeled with 220 nm of Si on top, lastly with 2 μm of air as the top cladding. The refractive indices used were 3.4784 for Si, and 1.4443 for SiO_2 [57]. The refractive indices of each material is given in Table 4.1.

The analysis returned an effective refractive index of $n_{\text{eff}} = 2.8331$, which was used in the simulations to follow.

Table 4.1: Refractive indices of air, Si and SiO_2 as used in the effective mode analysis.

Material	Refractive index
Air	1
Si	3.4784
SiO_2	1.4443



Figure 4.1: The effective mode index method COMSOL model. The model consists of a $10\ \mu\text{m}$ long structure, with a $1\ \mu\text{m}$ bottom SiO_2 layer, in turn with a $220\ \text{nm}$ thick layer of Si on top, representing the waveguide structure. The top air layer has a thickness of $2\ \mu\text{m}$.

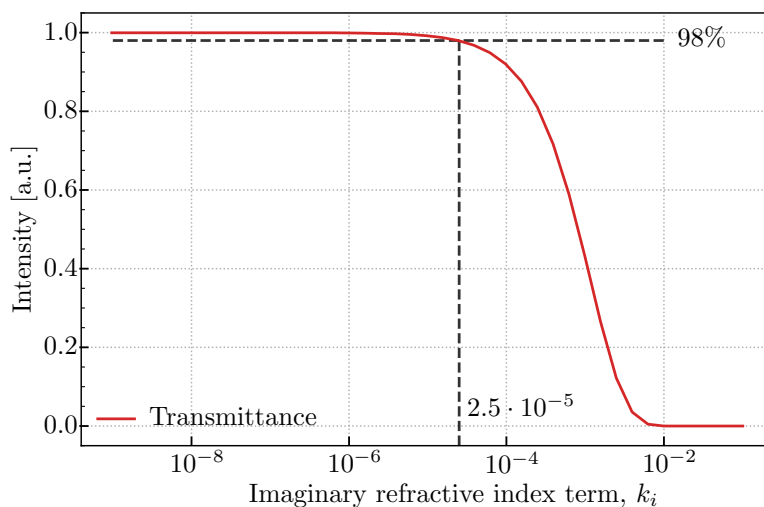


Figure 4.2: Transmittance through $100\ \mu\text{m}$ waveguide core, as a function of the imaginary refractive index term, k_i . A transmittance of 98% was desired, which gives $k_i = 2.5 \cdot 10^{-5}$.

4.1.3 Implementing Waveguide Losses

In order to make the COMSOL model more realistic, the waveguides were given a non-zero absorption coefficient, by introducing a non-zero imaginary component k_i to the refractive index of the waveguide material. The desired value for k_i was found by modeling a straight waveguide of a certain length ($100\ \mu\text{m}$), while sweeping over several orders of magnitude for k_i , and plotting the transmittance of the waveguide section. The desired total absorption was set to 2%/ $100\ \mu\text{m}$, which translates to approximately 9.1 dB/cm, a realistic value for an SOI waveguide[34].

The sweep is plotted in fig. 4.2, and by the requirements put forth, the imaginary term of the core refractive index was determined to be $k_i = 2.5 \cdot 10^{-5}$.

4.1.3.1 Bending Loss Evaluation

An evaluation of the bending losses for different bend radii was performed, in order to find a suitable bend radius that would still allow for a compact device with low bending losses. A short, straight waveguide section was connected to a 180° turn, connected to another straight waveguide section. Multiple bend radii were simulated and tested in terms of their effect on transmission loss, with radii ranging from approximately $6\ \mu\text{m}$ to $40\ \mu\text{m}$. The wavelength was fixed at $1550\ \text{nm}$ for this analysis.

The results from the evaluation are shown in fig. 4.3, along with an exponential fit of the form $A(r) = ae^{-br}$, $a = 2.11 \cdot 10^{-5}$, $b = 0.197\ \mu\text{m}^{-1}$, where r is the bend radius in μm . These

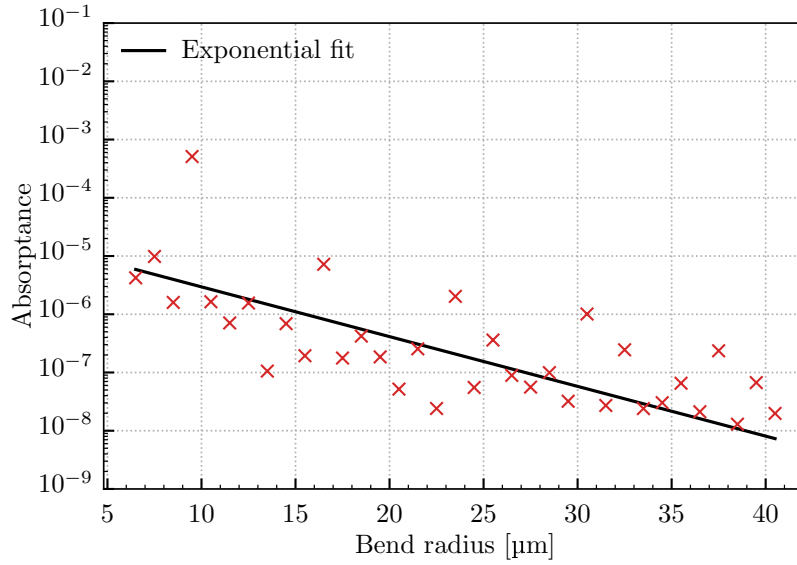


Figure 4.3: Waveguide loss as a function of the bending radius of the waveguide. The exponential fit is of the form $A(r) = ae^{-br}$, $a = 2.11 \cdot 10^{-5}$, $b = 0.197 \mu\text{m}^{-1}$, with r being the bend radius in μm .

tests were performed with no inherent material absorption (i.e. $k_i = 0$), and, as is expected, a decrease in the bending radius yields an increase in the bending losses. It is however worth noting that even for the smaller bend radii tested, the absorption is still low (in the order of 10^{-5}), and is thus deemed negligible. The actual bend radius used in the MARC models was therefore set to be $8.5 \mu\text{m}$, in order to keep the entire MARC structure relatively compact.

4.1.4 Key Parameters

A large set of parameters were created during the modeling of the MARC structures, to aid the process of aligning waveguide sections properly. Many of these parameters are solely acting as coordinates for the various components, and are as such of little interest and will not be discussed any further. The remaining parameters are however more relevant, and the most important values are presented in Table 4.2, along with the findings of the analyses and tests described previously in this chapter (namely `n_core`, `k_core` and `bend_radius`).

Table 4.2: General parameters used in the COMSOL simulation of the MARC sensors.

Name	Values	Description
<code>n_core</code>	2.8331	Core refractive index, real term
<code>k_core</code>	2.5×10^{-5}	Core refractive index, imaginary term
<code>n_clad</code>	1	Cladding (air) refractive index, real term
<code>k_clad</code>	0	Cladding (air) refractive index, imaginary term
<code>wg_width</code>	500 nm	Waveguide width
<code>clad_width</code>	$3.5 \mu\text{m}$	Cladding width
<code>bend_radius</code>	$8.5 \mu\text{m}$	Waveguide center bend radius
<code>cd</code>	161.5 nm	Waveguide separation in 3dB coupler
<code>resolution</code>	20 pm	Wavelength resolution

Table 4.3: COMSOL mesh size parameters used in the simulations.

Material	Parameter	Value
Core	Maximum element size	0.0498 μm
	Minimum element size	0.00149 μm
	Maximum element growth rate	1.3
	Curvature factor	0.3
	Resolution of narrow regions	1
Cladding	Predefined setting, general physics	Normal
PML	Maximum element size	0.225 μm
	Minimum element size	0.0575 μm
	Maximum element growth rate	1.3
	Curvature factor	0.3
	Resolution of narrow regions	1

4.1.5 Mesh Setup

The model geometry was discretized using a mesh as specified in Table 4.3. A *free triangular* mesh was used in the core and the cladding, as well as for the PML layers of non-rectangular geometry. For long, straight domains, the PML layers were tessellated using a *mapped* mesh. See fig. 4.4 for a view of the different mesh types and granularities used.

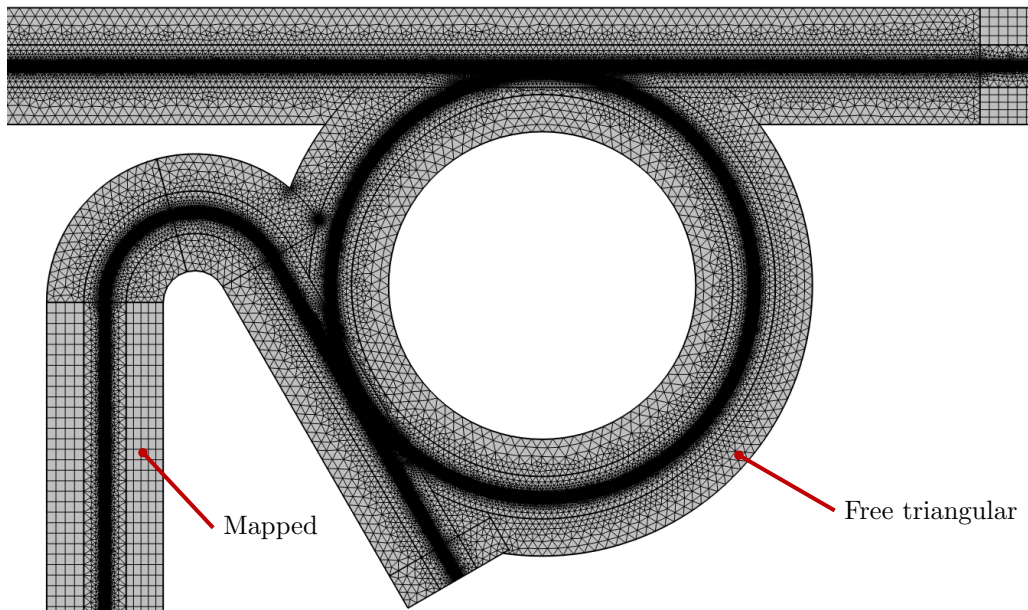


Figure 4.4: Overview of the mesh applied to the COMSOL model. Notice how the granularity of the mesh increases significantly towards the waveguide core, as well as for the more complex geometries, like bends and coupling regions. The two mesh types are indicated.

4.1.6 Component Design and Optimization

Before proceeding with building the complete MARC structures, the individual constituents were firstly designed and optimized. These structures include the input- and output 3dB coupler, the add-drop ring resonators, as well as the Mach-Zehnder interferometer. This optimization was performed to ensure the proper operation of said structures, in addition to acquiring useful insight into the behavior of the components during wavelength sweeps. The next subsections will briefly

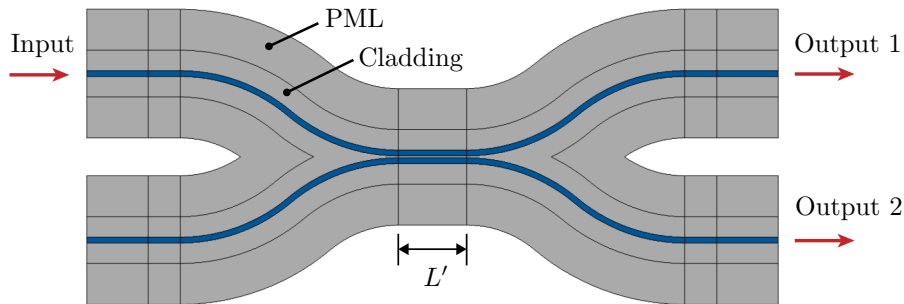


Figure 4.5: COMSOL model of the 3dB (input) coupler. The core is colored dark blue, and the cladding and perfectly matched layers (PML) are indicated. The same layered design of the waveguide is used for the other models as well. The coupling length is $L' = 5.86 \mu\text{m}$.

explain the procedures behind these optimizations.

4.1.6.1 3dB Coupler

The input and output from the MARC device is designed as a conventional directional 3dB coupler, with a waveguide separation of 161.5 nm in the coupling region. The coupler was simulated with different coupling lengths L' in order to give equal splitting of the input power, and for $L' = 5.86 \mu\text{m}$, this was achieved. The coupling region length was therefore set to this value, and a wavelength sweep over $\lambda_0 \in [1500, 1560] \text{ nm}$ was performed, in order to map the wavelength dependence of the 3dB coupler. Additionally, the phase shift of this coupling was measured by comparing the phase of the waves in both outputs of the coupler. See fig. 4.5 for a view of the COMSOL model geometry for the 3dB coupler.

4.1.6.2 Ring Resonator Optimizations

The add-drop ring resonators themselves were simulated independently, with the intention of optimizing the coupling distance between the ring and the input/output waveguides. A simple model of an add-drop ring resonator was therefore designed, and the coupling distance was varied in small increments, in order to find the distance that would yield the highest extinction ratio (i.e. critical coupling, see section 2.4.2.1), and as narrow full-width half-maximum (FWHM) at resonance as possible. The acquired values for the coupling distances were then used in the further implementation of the ring resonators in the models.

4.1.6.3 Mach-Zehnder Interferometer

The Mach-Zehnder interferometer (MZI) was also simulated independently, in order to gain insight into any inherent wavelength dependent behavior. The optimized 3dB couplers were used as the input- and output couplers, and two identical interferometer arms were placed between the couplers. A wavelength sweep over $\lambda_0 \in [1510, 1550] \text{ nm}$ was performed.

4.1.7 Balancing of Individual MARCs

The multiplexed MARC was designed to consist of three individual ring resonators. These rings have angular separations of 135° , 90° , and 240° , and will from this point therefore be referred to by their angular separation, e.g. "135° MARC". These angular separations were selected due to their significantly different transmission spectra (see Appendix A), which makes their signatures simpler to discern.

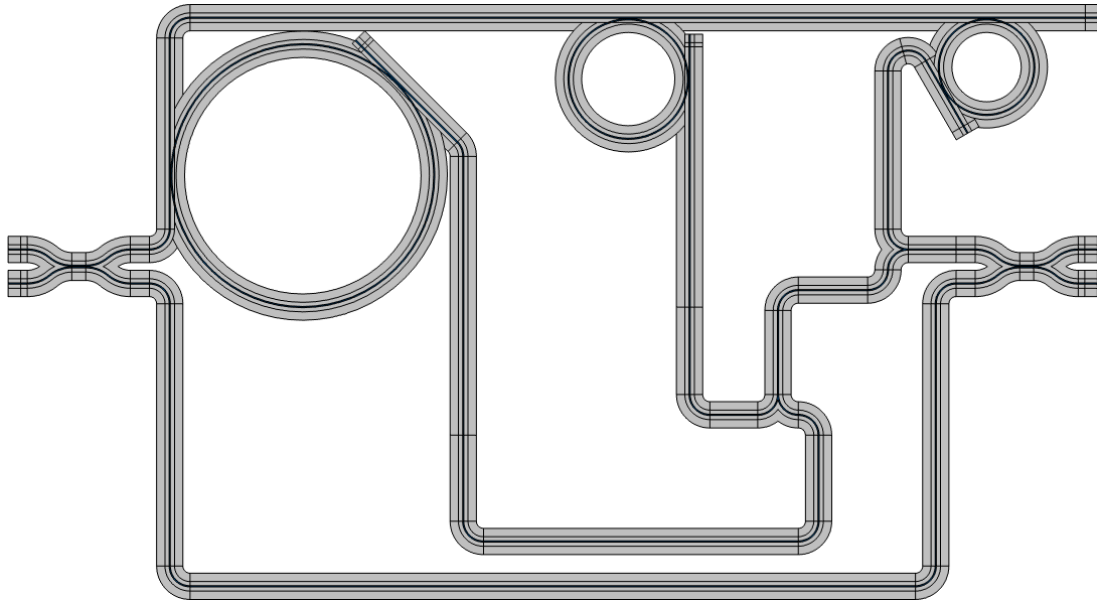


Figure 4.6: COMSOL model of the multiplexed, 3-ring MARC.

To ensure the proper balancing of each individual MARC, multiple simulation runs were performed of each single-ring MARC. This procedure started with the last ring in the sensor cascade, namely the 240° MARC: The two interferometer arms were firstly made to be identical in length, not including the optical path length of the ring. A wavelength sweep was then simulated, and the transmission spectrum was compared to the corresponding ideal MARC transmission spectrum of the same sensor configuration. If any discrepancies were discovered, the corresponding phase imbalance φ of this discrepancy was determined, and subsequently the main balance arm of the MZI was shortened/extended by a distance $d = \frac{\varphi \lambda_0}{2\pi n_{\text{eff}}}$. Here $\lambda_0 = 1530$ nm (the center of the wavelength sweep), and n_{eff} is the effective refractive index of the lowest order mode, as calculated by COMSOL during the boundary mode analyses at the ports in and out of the MARC structure. A new wavelength sweep was then run, and ideally the MARC would show a better balance.

Once the 240° MARC was balanced, the next-to-last sensor, i.e. the 90° MARC, was optimized similarly. However, in this case the main balance arm of the MZI was not changed, but rather the "ring-arm" of the interferometer instead. Lastly, the 135° MARC was optimized, as parts of the "ring-arm" length of this MARC coincides with that of the 90° MARC. See fig. 4.6 for an overview of the finalized multiplexed MARC device.

4.2 Lithography Mask Design

The lithography masks were designed from the parameters of the COMSOL CAD models, using a Python module called *Nazca*¹ (see Appendix C for additional details). As positive resist was to be used in the patterning process, the waveguide masks were designed as two parallel bands of $2.25 \mu\text{m}$ width, separated by the waveguide width (i.e. 500 nm). This would, after etching, result in $2.25 \mu\text{m}$ wide trenches on either side of the waveguide core, thus physically isolating the waveguide from the surrounding Si slab². See fig. 4.7a for the mask design of the 3dB directional coupler used in the MARC design.

To make input- and output-coupling of light from the MARC device simpler, waveguide extensions of approximately 4 mm in length were added to the COMSOL design, in both ends

¹<https://nazca-design.org/>

²The width of these trenches were selected based on lithography masks used for the fabrication of the MARCs described in [3, 4]

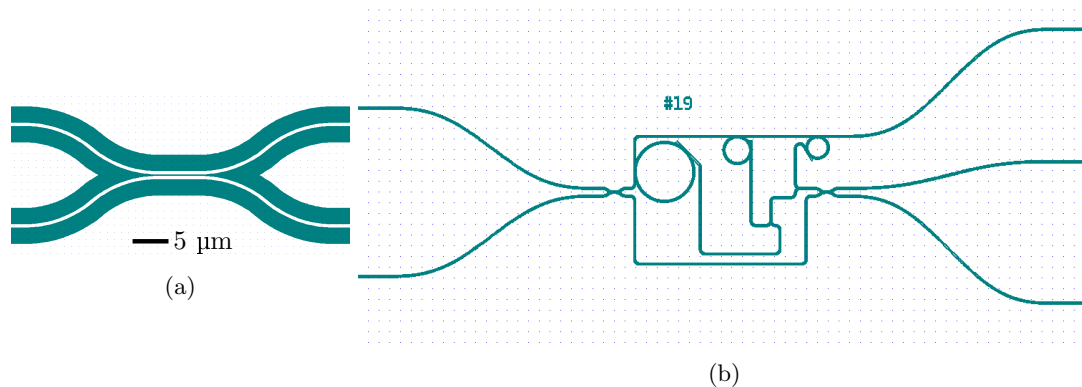


Figure 4.7: Overview of the lithography mask used in the fabrication of the MARCs. a) The 3dB coupler region. The colored areas are exposed to the electron beam, and since positive resist is used, these areas will thus be exposed for etching in the later stages. In order to reduce the exposure time, only an area of $2.25\ \mu\text{m}$ outside the waveguide is exposed. b) Overview of the MARC structure with input and output waveguides separated. Images are screenshots from the CleWin 4 layout editor software.

of the sensor. Moreover, large bends were added to these input- and output ports, in order to separate them by approximately $300\ \mu\text{m}$. This allows for coupling in and out of single waveguides only, see fig. 4.7b.

Both inputs and outputs to the MARC structures are also extended, even though only one of each is required for the operation of the MARC. This is done for redundancy reasons, in case of a partially failed fabrication process. This way, the risk of waveguide defects rendering the entire sensor useless is greatly reduced.

The inverted tapers were added to the ends of the input and output waveguides, and were designed to gradually reduce the $500\ \text{nm}$ wide waveguide into a narrow, $75\ \text{nm}$ wide waveguide, over a length of $300\ \mu\text{m}$. The polymer waveguide covers for the inverted tapers were designed as $2\ \mu\text{m}$ wide waveguides, covering the entire tapered region. These parameters for the inverted tapers were an "initial guess" based on [3, 4].

4.3 Fabrication

A general overview of the processing steps used in the fabrication of the waveguide structures is provided in fig. 4.8. In essence, amorphous Si (a-Si) is firstly deposited onto the sample by plasma-enhanced chemical vapor deposition (PECVD), before electron beam lithography (EBL) patterning is done. Following this, the sample is etched using inductively coupled plasma-reactive ion etching (ICP-RIE). Lastly, polymer waveguides are deposited to create the inverted taper in-coupling structures.

4.3.1 Wafer Preparation

A 4" silicon wafer was used as the foundation for the laboratory work. This wafer was delivered from the factory with $1\ \mu\text{m}$ of silicon oxide (SiO_2), deposited thermally, i.e. the wafer has undergone a heat treatment in a humid environment to allow for the oxidation of the surface Si. This process maintains the surface roughness of the original wafer, which is beneficial to waveguide operation.

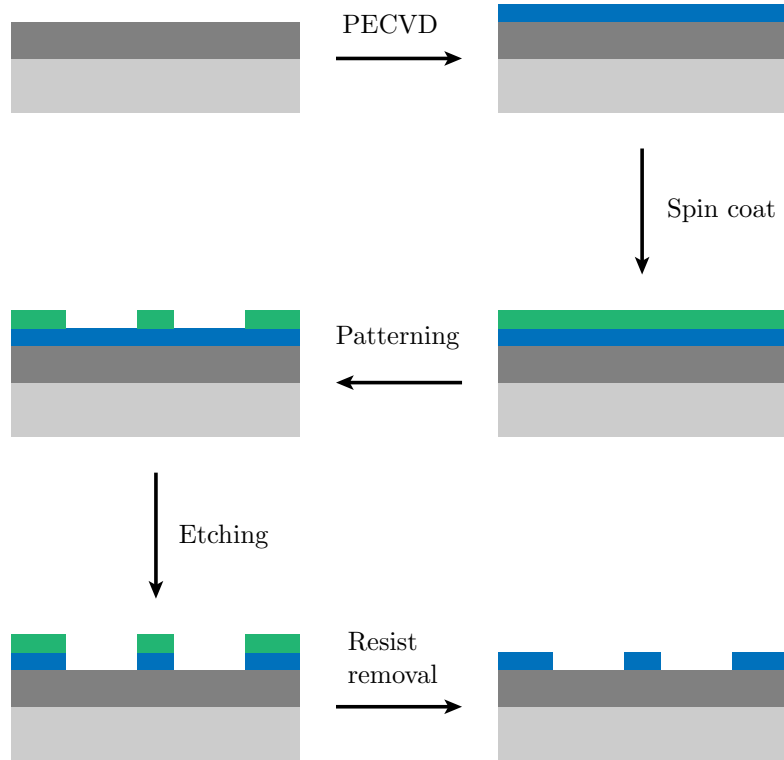


Figure 4.8: Waveguide fabrication process overview. The figures represent the wafer cross-section at the different steps in the fabrication process. The wafer substrate is indicated in light gray, along with the thermally deposited silicon dioxide layer, denoted by a darker gray color. The blue layer is the Si waveguide layer, and the resist has been colored green. The thickness of each layer relative to the others are not to scale.

4.3.2 Silicon Deposition

An (*Oxford Instruments PlasmaLab System 100*) PECVD was used to deposit 220 nm of a-Si onto the wafer substrate. Precursor gas flows of 50 sccm (standard cubic centimeters per minute) of silane (SiH_4), and 150 sccm of argon (Ar) were maintained for 2 minutes and 50 seconds. See Table 4.4 for additional process parameters.

Table 4.4: Process parameters for the PECVD deposition of a-Si.

Parameter	Value
SiH_4	50 sccm
Ar	150 sccm
LF power	200 W
Pressure	500 mtorr
Temperature	300 °C
Deposition time	2 min 50 sec

4.3.3 Wafer Dicing

After PECVD deposition, the SOI wafer was manually diced into smaller rectangular samples with dimensions of approximately $2\text{ cm} \times 3\text{ cm}$, using a diamond scribe pen and a set of wafer cleaving pliers.

Table 4.5: Spin coat deposition and EBL operating parameters used for waveguide patterning.

Process	Parameter	Value
Spin coat	Spin speed	3200 RPM
	Acceleration	1000 RPM/S
	Duration	62 seconds
Soft bake	Temperature	150 °C (hotplate)
	Duration	60 s
EBL	Acceleration voltage	100 kV
	Beam current	1 nA
	Objective Lens Aperture	120 μm
	Beam diameter	2.3 nm
	Write field (size)	1 000 $\mu\text{m} \times 1\ 000\ \mu\text{m}$
	Write field (dots)	500 000 dots
	Area dose	315 $\mu\text{C}/\text{cm}^2$
	Dose time	0.014 $\mu\text{s}/\text{dot}$
	Feed pitch	1 nm
	Scan pitch	1 nm

4.3.4 Waveguide Patterning

An (*Elionix ELS-G100*) EBL system was used to pattern an etch mask on the SOI samples, using (*Allresist AR-P 6200* (CSAR 62)) positive electron beam resist. An initial spin coat deposition and EBL dose test was performed to establish proper process parameters, and the resulting parameters from this test are presented in Table 4.5. These parameters were used in the further processing of the samples. The spin coat parameters were optimized to yield a resist layer thickness of 180 nm, using a diluted CSAR 62 solution (6.14 g Anisole, 12.23 g CSAR 62).

Prior to the spin coating of the resist, the samples were cleaned. The samples were immersed in an ultrasonic acetone bath for 1 minute, before they were immersed in an ultrasonic isopropanol (IPA) bath, again for a duration of 1 minute. The samples were then spin coated with CSAR 62, and a subsequent 60-second hotplate soft bake at 150 °C was done.

In the EBL software, the electron beam was firstly set up and adjusted. The sample tilt was then measured to verify proper mounting of the sample in the sample holder, and *field correction* was performed in order to reduce write field stitching errors.

After exposure, the samples were developed by immersion and gentle agitation in (*Allresist AR 600-546*) developer for 60 seconds, followed by a short immersion and agitation in IPA, to stop the development. Finally, the sample is immersed in a second beaker of IPA for 60 seconds, and a gentle N_2 blow-dry is done to dry the sample. A quick plasma cleanse (descum) was also performed, using a (*Diener Electronics Femto*) plasma cleaner, set to 50/50 O_2 flow/power for a duration of 12 seconds.

4.3.5 Etching

The patterned samples were then etched (using an *Oxford Instruments PlasmaLab System 100 ICP-RIE 180*), and the relevant process parameters are presented in Table 4.6.

Before etching the sample, a "dummy-etch" procedure was performed. This involves running the etching procedure once, however without any samples in the process chamber. This is done to reduce any traces of the etching chemistry caused by the previous user of the instrument. For the actual etching, the sample was placed on a 4" silicon carrier wafer, using Fomblin oil to ensure both that the sample remains stationary on the carrier wafer, and to provide better heat conduction between the temperature-regulated sample holder and the sample itself. The sample was etched for a duration of 40 seconds.

After etching, the remaining resist was removed from the sample by using an O₂ plasma cleanse. 10 minutes of 50/50 flow/power, followed by 2 minutes at 100/100 was deemed sufficient.

Table 4.6: ICP-RIE parameters for etching a-Si.

Parameter	Value
SF ₆	7.5 sccm
CHF ₃	50 sccm
Pressure	15 mtorr
Temperature	20 °C
Duration	40 s

4.3.6 Inverted Taper Fabrication

The final fabrication step was to deposit polymer waveguides on top of the tapered waveguide sections at the input- and output ends of the waveguide structures. The wafer with waveguides on top was cleaned in an IPA bath, before a 2-minute 50/50 O₂ plasma cleanse was performed. 2 μm of negative, near-UV photoresist (*MicroChem SU-8 2000*)(SU-8) was spin deposited onto the sample, followed by a 3-step soft bake. Due to its thermal expansion, SU-8 benefits from a gradual warming up and cooling down, and thus the baking steps are divided into three steps: 1) intermediate warm-up to 50 °C, 2) baking at 95 °C, and 3) intermediate cool-down to 50 °C, before letting the wafer cool to room temperature. A cold-plate was not used, in order to let the samples cool down more slowly.

The samples were placed in a (*Heidelberg MLA150*) maskless aligner and aligned properly (alignment marks were placed in the mask design prior to the EBL exposure), before exposure was performed. Following the exposure and before the development, a post-exposure bake (PEB) was performed to enhance the cross-linking of the resist. See Table 4.7 for the complete list of parameters at each step.

Development was done using immersion (in *Micro Resist Technology mr-Dev 600*) and gentle agitation for 60 seconds, stopped by a 60-second immersion in IPA. The sample was gently blow-dried using pressurized N₂, and an optical inspection using a microscope confirmed the proper processing of the inverted taper polymer waveguides.

4.4 Characterization

During and after the fabrication procedure, the samples were characterized and investigated in order to verify that the fabrication was indeed successful. This includes visual inspections using an optical microscope and a scanning electron microscope (SEM).

4.4.1 Optical Microscopy

A (*Carl Zeiss Axio Scope A1*) optical microscope was used to verify the development and etching process during the fabrication. This was only qualitative, as the resolution and magnification of this microscope is insufficient for any quantitative analysis of critical features and dimensions.

4.4.2 Scanning Electron Microscopy

An (*FEI APREO*) SEM has been used to take images of relevant structures and features, particularly cross-sectional profiles and coupling regions between ring resonators and waveguides. This SEM was also used during the EBL dose test procedure, in order to determine the proper dosage

Table 4.7: Spin coat and photolithography processing parameters used for inverted taper patterning.

Process	Parameter	Value
Spin coat	Spin speed	5000 RPM
	Acceleration	1000 RPM/S
	Duration	35 s
Soft bake	Warm-up	50 °C @ 120 s
	Bake	95 °C @ 120 s
	Cool-down	50 °C @ 120 s
Exposure	Dose	3 500 mJ/cm ²
	Wavelength	375 nm
Post-exposure bake	Warm-up	50 °C @ 120 s
	Bake	95 °C @ 180 s
	Cool-down	50 °C @ 120 s

for the fabrication. Images were taken both using the secondary electron (SE) signal, as well as using the backscattered electron (BSE) signal.

4.5 Transmission Characterization Setup

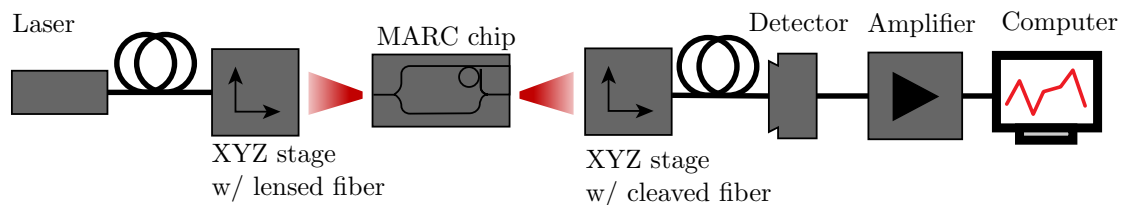


Figure 4.9: Schematic of the transmission characterization setup used in the lab. This setup is used to characterize the optical transmission of waveguide devices.

The laboratory setup used to perform transmission measurements on MARC structures is schematically shown in fig. 4.9. A tunable (1500-1580 nm) (*Thorlabs TLK-L1550M*) laser is input to a single-mode fiber, terminated in a lensed fiber. The lensed fiber is mounted on an (*Elliot*) precision XYZ stage with the lensed fiber focusing the output light onto the input port of the MARC chip. At the MARC output, on a similar XYZ stage, a straight-cleaved fiber is mounted and connected to a (*Thorlabs DET10C2*) detector. The signal from the detector is amplified through a (*Thorlabs PDA200C*) photodiode amplifier. Lastly, the amplifier output is connected to a (*National Instruments PCI-6024E*) data acquisition device (DAQ) in the laboratory computer. A custom-made LabView³ program has been written to help automate wavelength sweeps and storage of the acquired sensor measurements.

Not shown in the schematic is an (*Olympus BXFM*) optical microscope mounted above the MARC chip stage, with an add-on near-IR capable (*Hamamatsu C14041-10U*) microscope camera. In addition, the laser is driven by a (*Newport Model 505*) laser diode driver, and kept at a proper operation temperature by a (*Newport Model 325*) temperature controller.

³<https://www.ni.com/en-no/shop/labview.html>

Chapter 5

Results and Discussion

The results from the COMSOL simulations as well as the fabricated devices will be presented in this chapter. The first sections will consider the simulations of the individual components, namely the 3dB directional coupler, add-drop ring resonators, and the Mach-Zehnder interferometer (MZI). Following, the simulations of the single-ring MARCs will be discussed, before taking a look at the results from the multiplexed MARC. Lastly, the resulting transmission spectra from the fabricated MARC sensors will be presented for comparison with their simulated counterparts. The discussions will follow each result directly.

5.1 Individual Component Simulations

5.1.1 3dB Coupler

The simulated intensity transmission of the 3dB coupler over wavelengths $\lambda_0 \in [1500, 1560]$ nm is shown in fig. 5.1. The 50/50 splitting point is located at approximately 1534 nm, however the wavelength dependence of the coupler gives a non-uniform power splitting over the wavelength range, spanning from 55/45 splitting in the lower wavelengths, to 45/55 splitting for the higher wavelengths, for port 1 and 2, respectively. This was not considered to be problematic for the simulations in this project, as the resonant behavior of the rings is not severely affected by uneven splitting. However, for future versions of the MARC models, there are techniques available that could aid in reducing the wavelength dependence of the coupler[58, 59].

The phase shift of the 3db coupler was measured to be $\varphi_{\text{coupler}} \approx -\pi/2$ radians. This was particularly useful to be aware of when balancing the individual single-ring MARC sensors.

5.1.2 Ring Resonators

Each add-drop ring resonator was simulated as a stand-alone structure, in order to find the optimal coupling distance between the waveguide buses and the ring waveguide. The optimized parameters for all three rings, as well as the calculated Q-factor (Q) (using eqn. 2.60), are presented in Table 5.1. These coupling distances gave good extinction at resonance, as well as having narrow full-width at half-maximum (FWHM) dips at resonance. Unsurprisingly, a decrease in Q is apparent as the ring radius decreases (the curvature of the ring waveguide thus increases, and so does the bending losses).

5.1.3 Mach-Zehnder Interferometer

The absorption spectrum from the stand-alone MZI simulations is shown in fig. 5.2a. From this point on forwards, an absorption loss of 2%/100 μm was implemented in the waveguide material, see section. 4.1.3. A few important observations can be made by looking at the spectrum, the first one being the general non-uniformity of the absorption over the wavelength range, while the second one is the finely spaced narrow absorption peaks.

As for the first observation, the reason for the non-uniformity is not clear. However, if keeping the 3dB coupler performance in mind (fig. 5.1), there might be indications of some correlation

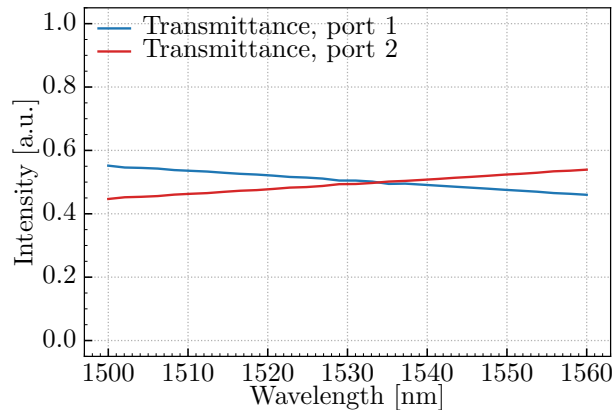


Figure 5.1: Intensity transmission of the 3dB directional coupler. The power splitting shows the linear wavelength dependence of the directional coupler, as is visible from the slope of the curves in the plot. No waveguide absorption losses were implemented in this simulation.

Table 5.1: Optimized ring parameters used in single-ring and multiplexed MARCs. No waveguide absorption losses were implemented in these simulations.

Ring	Parameter	Value
135°	Ring radius	55 μm
	Coupling distance	195 nm
	FWHM	0.134 nm
	Q-factor	≈ 11000
90°	Ring radius	25 μm
	Coupling distance	183.5 nm
	FWHM	0.153 nm
	Q-factor	≈ 10000
240°	Ring radius	20 μm
	Coupling distance	178 nm
	FWHM	0.202 nm
	Q-factor	≈ 7600

between the increasing imbalance in the power splitting of the input coupler of the interferometer, and the increasing absorption of the MZI. Conversely, in the wavelength region around 1534 nm, where the power splitting is close to 50/50, the absorption profile is rather uniform. This does indicate that at least one of the reasons for the non-uniformity is the non-ideal behavior of the 3dB coupler.

The other observation regards the "ripples" that are visible in the spectrum. These ripples are likely a consequence of reflections of light at the input and output ports of the MZI, in essence turning the entire structure into a Fabry-Perot (FP) resonator. Measuring the free spectral range of these ripples ($\text{FSR} = 0.51 \text{ nm}$), and using eqn. 2.46 to solve for d , one acquires the mirror separation for an FP-equivalent resonator of $d \approx 882 \mu\text{m}$. The length of each interferometer arm (including the input- and output couplers) in the simulated MZI is approximately $700 \mu\text{m}$, so d does not directly correspond to this distance, however it is possible that the 3dB coupler phase shifts have an effect on the apparent distance between the points of reflection.

As with the first observation, the amplitude of these ripples are significantly lower in the area of near-ideal 50/50 power splitting, and they also generally increase with the increasing power splitting imbalance. Attempts were made to shift the 50/50 splitting point of the 3dB coupler (by shortening or elongating the coupling length L'), in order to see whether the uniform, low-ripple

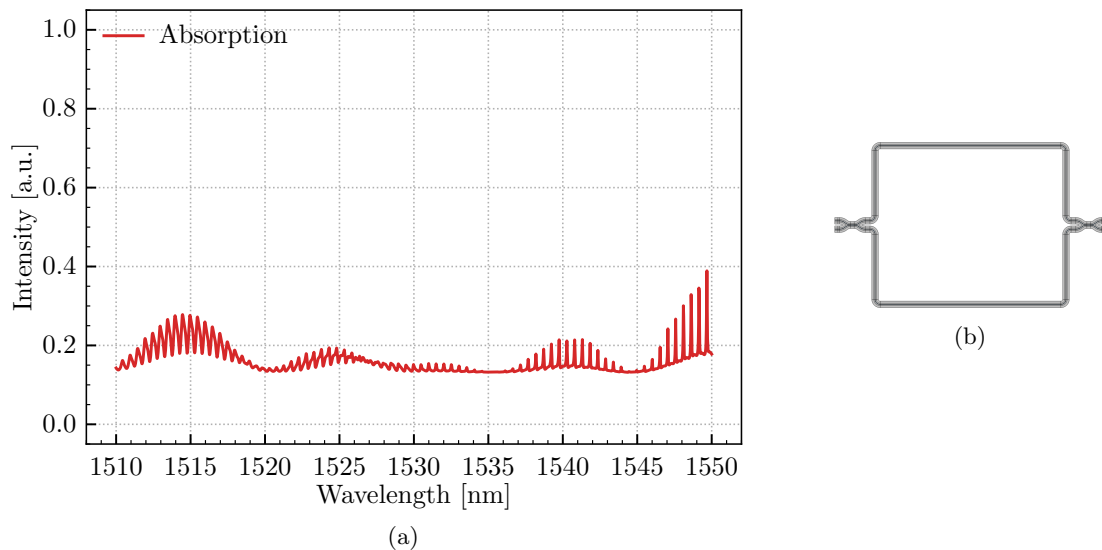


Figure 5.2: a) Absorption for different wavelengths in the MZI of the COMSOL MARC model. Notice the non-uniformity of the overall absorption, as well as the periodic ripples present in the signal. b) COMSOL model of the MZI.

regions would shift similarly in wavelength space. This did however not yield any significant changes in neither the non-uniform absorption, nor the low-ripple-noise area around the 50/50 power splitting point.

The ripples, being periodical signals, may be reduced using signal analysis filtering techniques on the transmission spectrum data, but this has not been done in this thesis. The ripple patterns discussed will therefore be visible in the simulated MARC structures to be presented in the later sections. They do not, however, significantly distort the features of the transmission spectra.

5.2 MARC Simulations

After the initial component optimizations, the MARC structures were designed and simulated. Any signs of imbalance were addressed (see section 4.1.7), and the resulting transmission spectra from each single-ring MARC, as well as the multiplexed MARC, will be presented below. The presentation will follow the order in which the simulations were performed, starting with the 240° MARC.

The COMSOL MARC simulations also calculated the effective refractive indices of each system, and in all configurations, COMSOL reported an effective refractive index of $n_{\text{eff}} = 2.6036$.

The transmission spectra of the theoretical counterparts to the simulated single-ring MARCs are presented in Appendix A for reference.

5.2.1 Individual MARC simulations

The simulated transmission responses of each individual MARC sensor will be presented and briefly discussed in the next sections. Each transmission spectrum will be presented along with a figure of the relevant COMSOL model geometry. For each sensor, the FWHM, FSR, FSR_e and Q-factor will be determined and discussed (the underlying theory and equations are found in sections 2.4.2 and 2.5). For the FWHM and FSR, the MARC drop port transmission responses were plotted, and the dip widths and separations were measured.

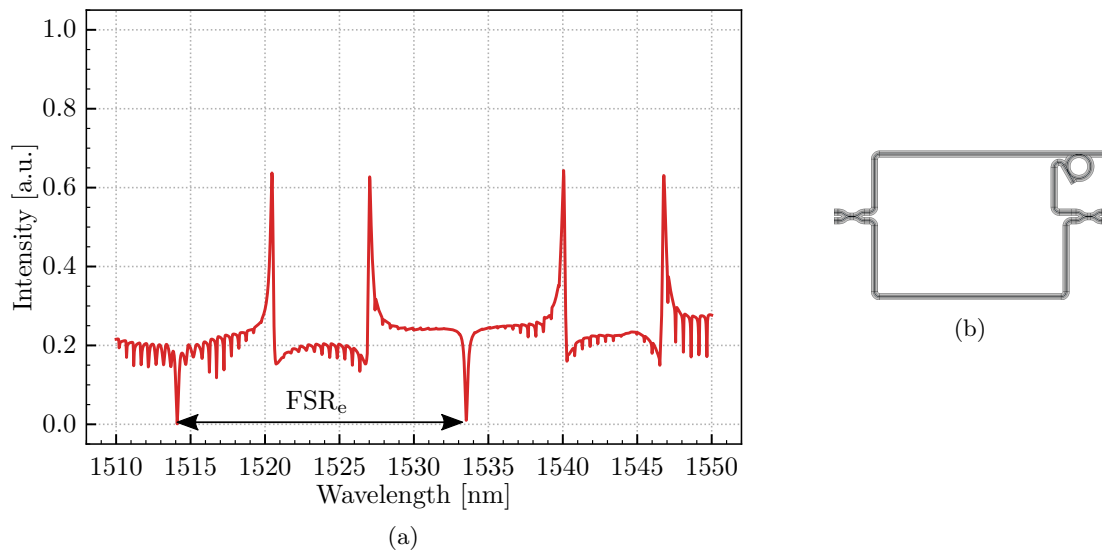


Figure 5.3: a) Simulated transmission spectrum of the 240° MARC sensor. The MARC is very well balanced across the wavelength sweep, and the wavelength region 1520-1547 nm shows very little ripples. $\text{FSR}_e \approx 19.6$ nm. b) COMSOL model of the 240° MARC sensor.

5.2.1.1 240° MARC

The simulated transmission response of the 240° MARC is shown in fig. 5.3. Disregarding the FP ripples, the signal is balanced well and has only minor asymmetries in the Lorentzian feature at approximately 1534 nm. The wavelength region 1520-1547 nm shows little ripples, and in general the spectrum is very recognizable (compare with fig. A.3 in Appendix A). The peaks are narrow and well-defined, and good extinction is achieved. Balancing this MARC was done by adjusting the lower arm of the interferometer until any interferometer imbalance was reduced.

From the through-port response of the MARC, the sensor displays fairly similar qualities to that of the stand-alone 240° ring resonator, with $\text{FWHM} = 0.221$ nm and $Q \approx 6900$. The ring-FSR is 6.53 nm, while the effective FSR of the MARC was measured to be $\text{FSR}_e = 19.6$ nm.

5.2.1.2 90° MARC

The simulated transmission response of the 90° MARC is shown in fig. 5.4. The wavelength region 1522-1545 nm shows relatively little ripples, however there are significant asymmetries in the Lorentzian features at e.g. 1532 nm. The peaks are nonetheless narrow, and adequate extinction is achieved at e.g. 1512 and 1527 nm.

The through-port response reveals $\text{FWHM} = 0.200$ nm, yielding $Q \approx 7700$. This Q-factor is greatly reduced for this MARC compared to the corresponding stand-alone ring resonator, as presented in Table 5.1. This is not unexpected, however, as the implementation of lossy waveguides will have the effect of broadening the resonant lineshapes of optical resonators.

The ring-FSR is 5.22 nm, and thus the four-fold improvement to the FSR from the 90° angular separation gives $\text{FSR}_e = 20.9$ nm. The FSR_e is indicated in fig. 5.4, however the imbalance of the MARC significantly deteriorates the spectrum, almost completely removing any indications of a periodical signal.

This particular MARC device was very difficult to balance, and the spectrum shown in the figure clearly reveals that the MARC is not properly balanced. Several attempts were made, unfortunately with no particular success. This MARC was nonetheless kept as-is, on the grounds

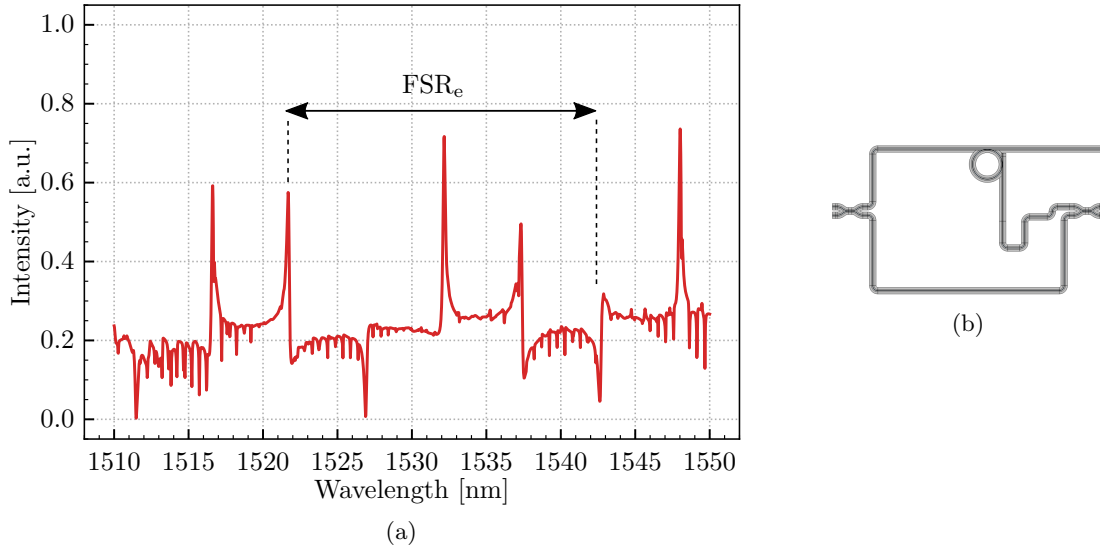


Figure 5.4: a) Simulated transmission spectrum of the 90° MARC sensor. Unfortunately, the signal suffers from poor balance and "random" ripples across the wavelength sweep, and the spectrum is not really recognizable as a 90° MARC spectrum. The peaks are however narrow and fairly well defined. $\text{FSR}_e \approx 20.9$ nm. b) COMSOL model of the 90° MARC sensor.

that the spectrum is still distinct and recognizable, even though it is strictly not similar to the spectrum of a 90° MARC.

In addition, the FP ripples are significantly different to those for the 240° MARC, particularly in their greatly varying amplitudes over the wavelength range; in short, the transmission spectrum of the 90° MARC appears rather noisy. This is likely due to the layout of the ring-side interferometer arm: For this MARC, the waveguide is significantly more curvy than for the 240° MARC, with 5 bends compared to 2. Although the waveguide bend radius was selected due to its relatively low loss, the bends might still give rise to undesired reflections, i.e. adding more FP ripples of different periodicity.

5.2.1.3 135° MARC

The simulated transmission response of the third and final single-ring MARC, the 135° MARC, is shown in fig. 5.5. This spectrum shows a fairly good balance across the entire wavelength range, with the region 1525-1541 nm being the least affected by FP ripples. As with the 90° MARC, the signal appears more noisy than that of the 240° MARC, and it is likely that the main reason for this is the more curvy nature of the waveguide in the ring-side interferometer arm. However, the balance of the interferometer is still kept remarkably well across the entire wavelength sweep, indicating that the number of waveguide bends not necessarily affects the balancing of the interferometer. This might suggest that the imbalance issues of the 90° MARC is more likely (partly) a result of the narrow "U-turn" shape of the waveguide, which the 135° MARC does not have.

The spectrum peaks are in general very narrow and the Lorentzian features are highly symmetrical. This claim is reinforced by the measured $\text{FWHM} = 0.162$ nm at the MARC through-port, which gives $Q \approx 9500$, a number that is relatively close to the performance of the stand-alone ring resonator. This is also the highest Q for all the single-ring MARCs simulated.

The ring-FSR was found to be 2.37 nm. The 135° angular separation of the ring resonator gives an increase in the effective FSR of 8x, meaning that $\text{FSR}_e = 18.9$ nm. The short FSR of this

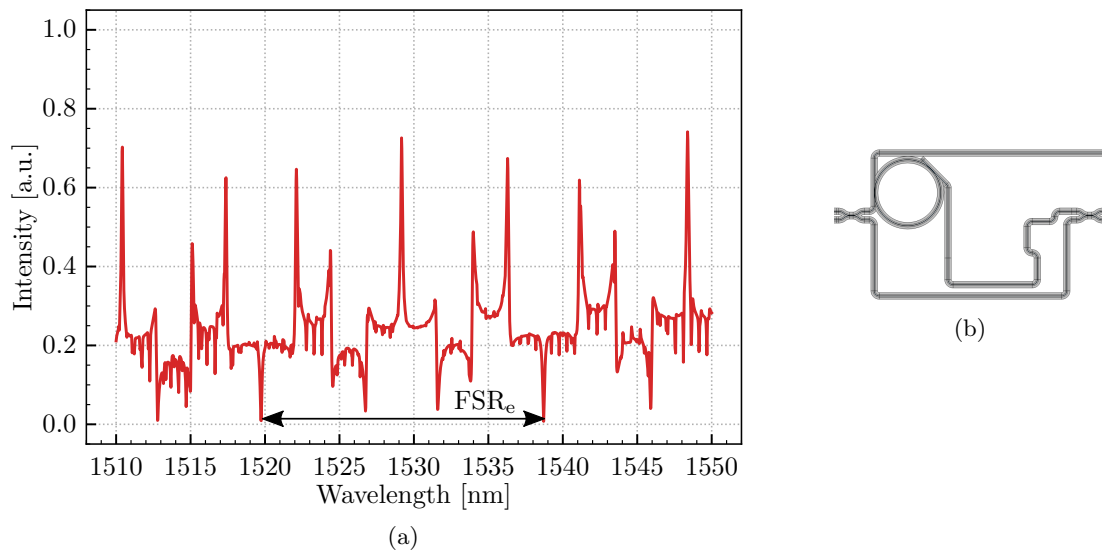


Figure 5.5: a) Simulated transmission spectrum of the 135° MARC sensor. The spectrum shows great balance over the wavelength sweep, however ripples are more significant near the wavelength range edges. $\text{FSR}_e \approx 18.9$ nm. b) COMSOL model of the 135° MARC sensor.

MARC means that the features are more densely packed, meaning that the spectrum is simple to discern from the other two MARC structures, which have more sparsely packed transmission spectra.

5.2.2 Multiplexed MARC Simulations

After all single-ring MARCs were balanced and simulated, a multiplexed MARC was modeled in COMSOL by including all three rings into one MZI, see fig. 4.6. As all individual MARCs by this stage were balanced (except the 90° MARC), the simulation was run, and the resulting transmission spectrum is shown in red in fig. 5.6. Note that this signal has been offset to increase the readability of the graph. The single-ring MARC transmission spectra are also shown.

From the transmission spectrum, it is clear that the signal does not look like a simple superposition of the constituent signals, which is what one would expect. In fact, very few peaks of the original signals are identifiable in the multiplexed signal, with the exception of the peaks at approximately 1521, 1522, 1540, and 1543 nm. However, by looking at the through-port response of the multiplexed MARC, the through-port behavior of all the constituent ring resonators are present in the multiplexed signal, meaning that the issue lies in the ring-side waveguide sections.

This opens up a multitude of possibilities regarding the sources of the chaotic spectrum. The first and probably most likely explanation is several sources of undesired reflections. The drop-ports of both the 135° ring and the 90° ring combine at one junction, before the drop-port from the 240° ring in turn combines with that signal at another, similar junction. Again, although the bends themselves should not result in much loss, the complex geometries at the junctions might induce multiple reflections, leading to increased amounts of FP ripples.

At the junctions, the COMSOL plots of the E-field distribution also indicate higher-order modes propagating in the system. These modes may interfere with the lower-order modes, possibly contributing to the poor quality of the spectrum.

For illustrative purposes, the multiplexed MARC model was also simulated after the introduction of a fictitious measurand on the 240° ring resonator. This was done by increasing the

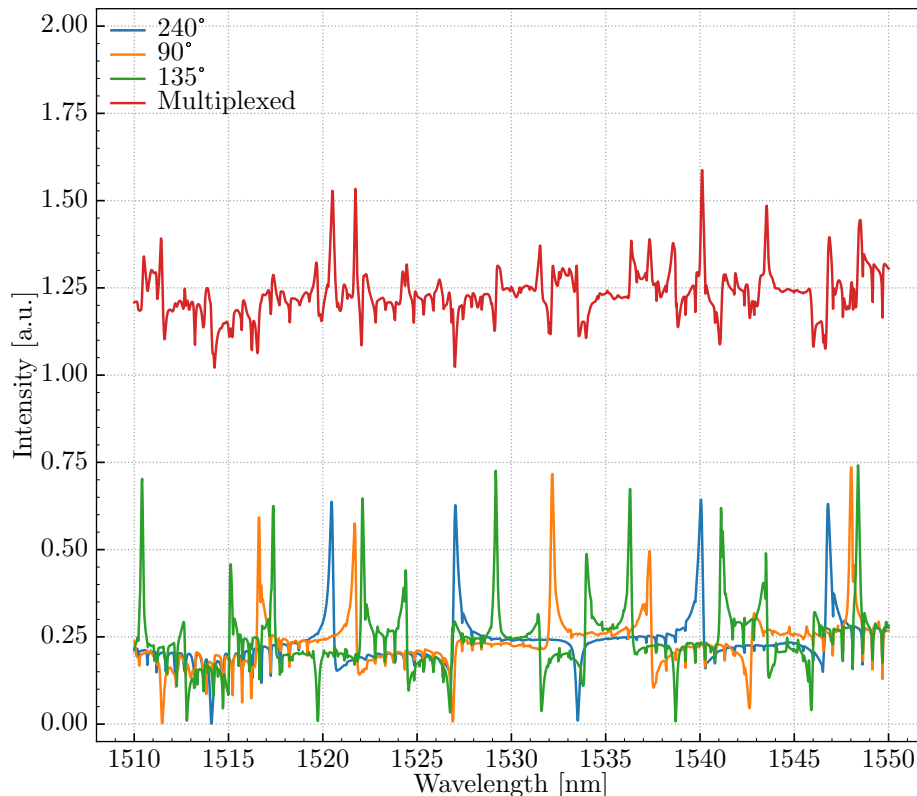


Figure 5.6: Simulated transmission response of the multiplexed MARC sensor. The multiplexed signal (red) has been offset to increase the readability of the plot. The transmission responses of the single-ring MARCs have been inserted in the graph as well, to indicate what the multiplexed signal should have looked more similar to. Only a few features (peaks) are very clearly originating from the individual MARC spectra, most notably the peaks at approximately 1521, 1522, 1540 and 1543 nm.

refractive index of the ring waveguide by $\Delta n = 0.010$, and the simulated transmission response is shown in fig. 5.7. From the spectrum it is clear that some peaks have shifted by a distance $\Delta\lambda \approx 5.3$ nm; these are the peaks corresponding to the 240° ring. Note that not all peaks of the individual 240° ring spectrum are seen to shift; this is because of "quenching" effects that occur when e.g. a peak in the signal of one MARC overlaps with a dip in the signal of another MARC in the same multiplexed device. In these cases, peaks might be concealed in the multiplexed signal, making de-multiplexing the signal more difficult. The key to alleviating this issue is to ensure that the ring resonators used in the multiplexed device have a sufficient number of peaks/dips within the MARC operating wavelength range. If enough features from one ring sensor are available in the multiplexed spectrum at any given time, the relative shift of this signal is much simpler to identify.

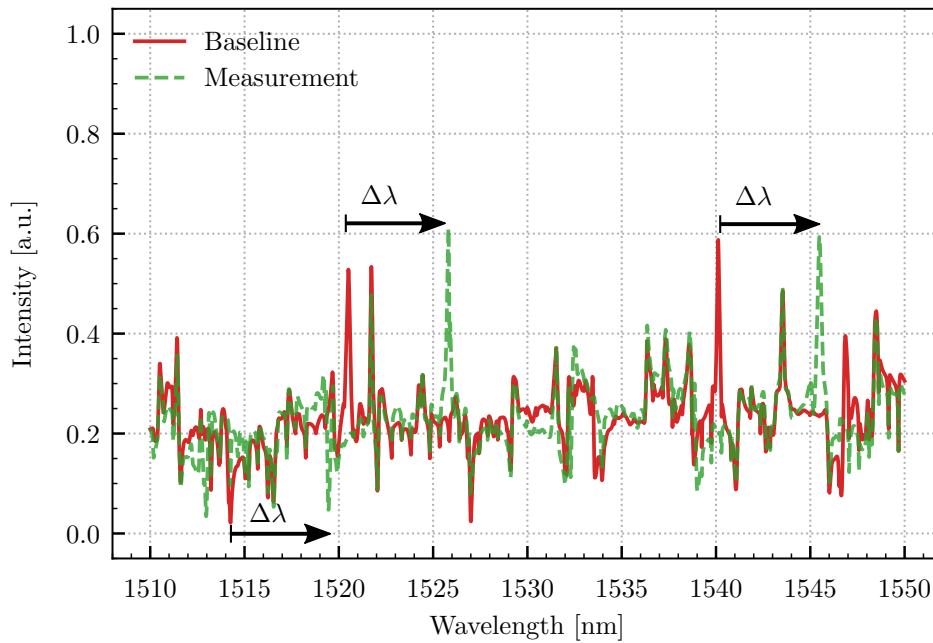


Figure 5.7: Simulated transmission response before (solid red) and after (dashed green) the fictitious measurand. The refractive index of the 240° ring was increased by $\Delta n = 0.010$, which resulted in a wavelength shift of $\Delta\lambda \approx 5.3$ nm of the peaks corresponding to the 240° ring, as indicated by the arrows. The other features of the spectrum remain unchanged.

5.3 Fabrication Results

For the sake of redundancy, a total of 20 MARC structures were fabricated on the same wafer chip: 5 identical versions of all three single-ring MARCs (i.e. 135°, 90°, and 240°), as well as 5 multiplexed 3-ring MARCs, in this particular order. The structures were lithographically labeled #1 - #20 for convenience, and the structures will be referred to by these numbers in the following sections.

A selection of the MARCs were investigated in the scanning electron microscope (SEM), and control measurements of the critical dimensions and features were taken. These parameters include ring radii and coupling distances, both for the rings and the 3dB couplers. These measurements of MARC #16 are presented in Table 5.2 and compared to the nominal design parameters. The fabricated structures are all within acceptable tolerances.

During the preliminary electron beam lithography (EBL) dose testing, different nominal waveguide widths were patterned and subsequently measured after etching. This was done in order to reveal any inaccuracies between the mask design and the fabricated structures, such that these errors could be corrected by compensating with the mask design. It was discovered that the fabricated narrow waveguides tended to be somewhat smaller than their nominal width. It was therefore decided to increase the mask width of the narrow waveguides from 75 nm, to 80 nm, to compensate for the smaller width of the realized structures.

The fabricated MARCs (#8 and #9) were inspected in the SEM, and the measurements of the narrowest point of the waveguide taper indicate an actual width of approximately 80 nm. This discrepancy (compared to the desired 75 nm) is not critical for the function of the waveguide tapers, but the width increase that was done in the mask design, thus turned out to be unnecessary. The widths of the wider waveguides were also measured, but these measurements show no significant deviation from the nominal value of 500 nm.

An overview SEM image of MARC #16 is provided in fig. 5.8. This image is taken using the signal from the backscattered electrons (BSE), as this gives information about the topography of the sample. At only 350x magnification, the waveguide core itself is difficult to distinguish from the etched trench surrounding it.

Fig. 5.9 shows SEM images of the wafer cross-section on the dose test sample. The sidewall profiles are very vertical, and the etch has successfully gone through the amorphous silicon (a-Si) layer. The top a-Si layer was measured to be approximately 220 nm, and the factory-delivered SiO₂ layer was confirmed to be 1 μm in thickness. The sidewall edge roughness is difficult to evaluate, however from the cross-sectional images the waveguide walls appear rather smooth.

SEM images of the fabricated 3dB input coupler of MARC #9, along with each drop-port coupling region of MARC #16 are shown in fig. 5.10. For fig. 5.10a, the BSE signal was used, while for the others, the secondary electron (SE) signal is used. These images further reinforce the claim that the sidewalls are relatively smooth, however there are in fact imperfections visible in the ring resonator waveguide in fig. 5.10c.

Table 5.2: Dimensional measurements of the fabricated MARC #16, compared to the nominal (designed) values.

Component	Parameter	Nominal	Actual
3dB couplers	Coupling distance	161.5 nm	0.16 μm
135° ring	Ring radius	55 μm	54.9 μm
	Coupling distance	195 nm	0.20 μm
90° ring	Ring radius	25 μm	24.9 μm
	Coupling distance	183.5 nm	0.18 μm
240° ring	Ring radius	20 μm	19.6 μm
	Coupling distance	178 nm	0.17 μm

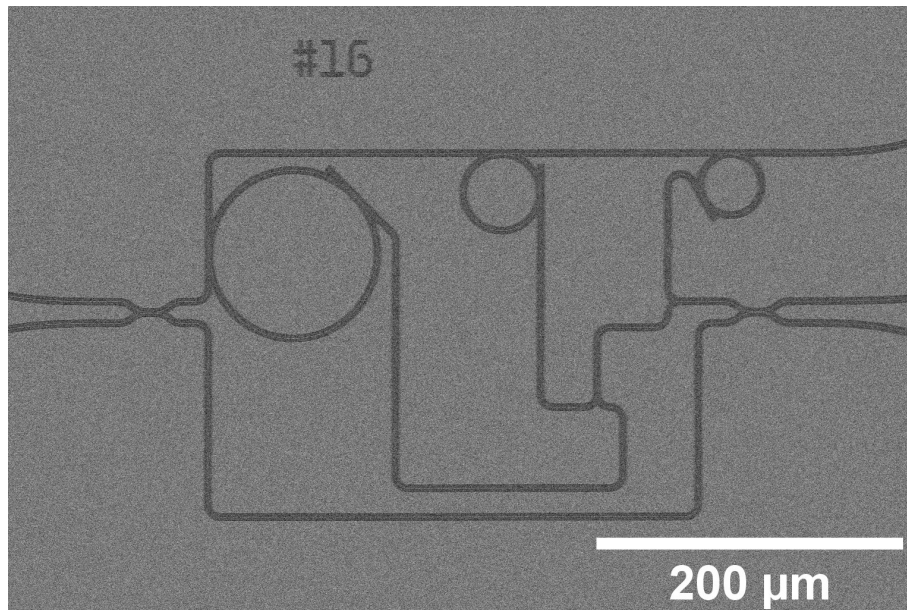
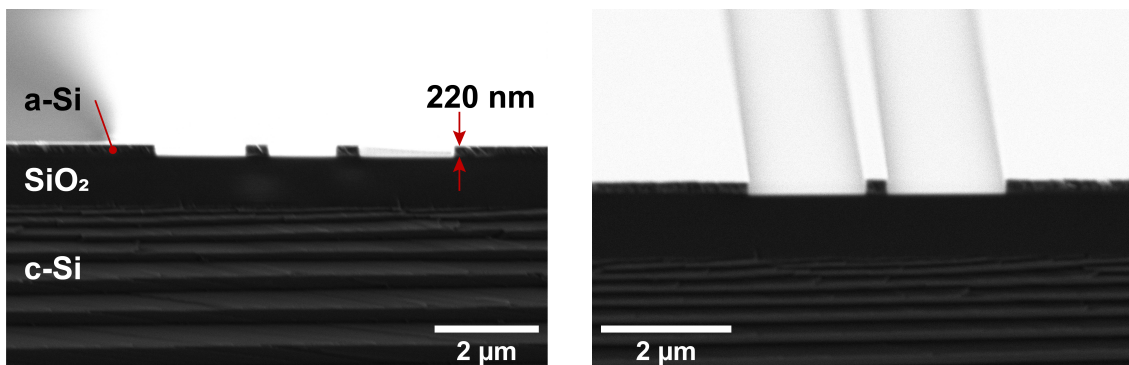


Figure 5.8: SEM overview of MARC #16. BSE signal, 350x magnification, 10kV acceleration. Image courtesy of Thorstein Wang.



(a) BSE signal, 20 000x magnification, 2kV acceleration.

(b) BSE signal, 25 000x magnification, 2kV acceleration.

Figure 5.9: Cross-sectional SEM images of waveguide structures. a) Waveguide cross-section close to the coupling region between a bus waveguide and a ring. The curving of the ring is faintly visible in the rightmost waveguide. The image shows the layered structure of the SOI wafer, and the sidewall profiles appear highly vertical. b) Angled view of a straight waveguide section. Both images courtesy of Thorstein Wang.

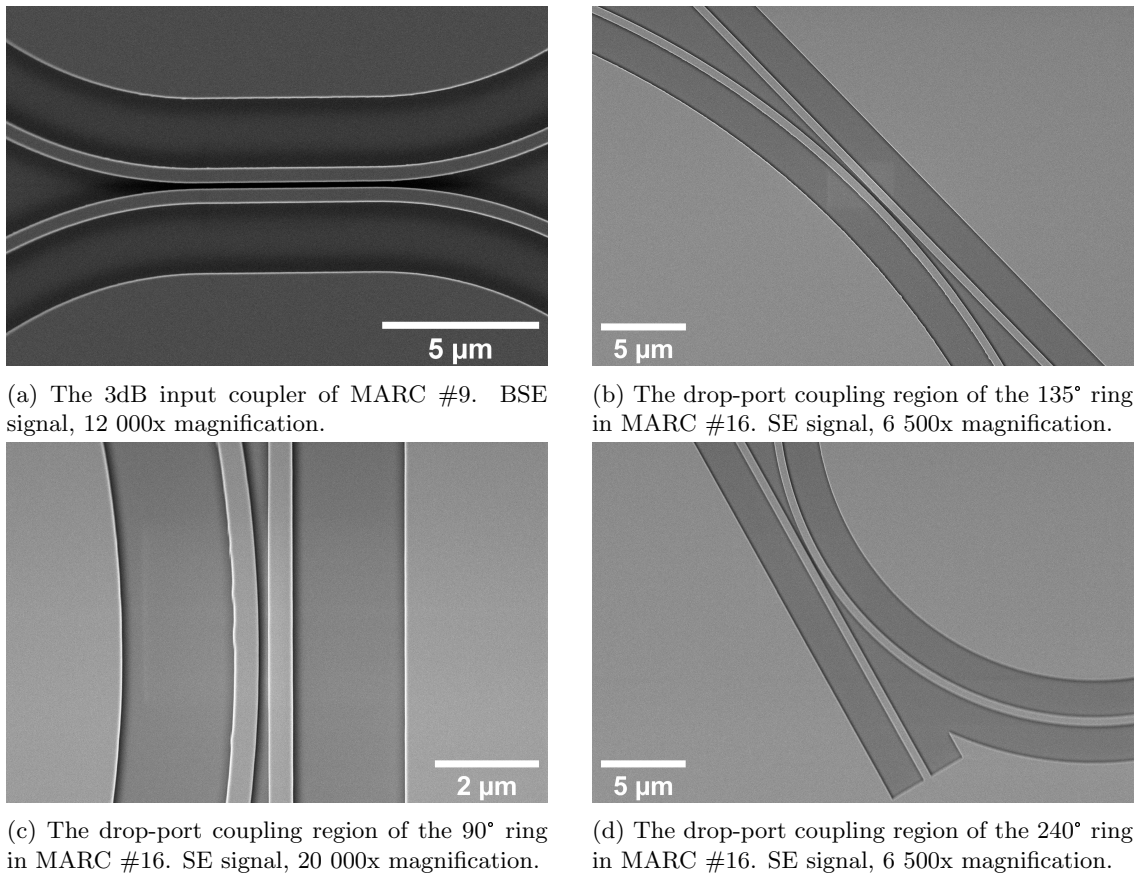


Figure 5.10: Top-down view SEM images of the various coupling regions of the fabricated MARCs. Notice the slight bulges on the inner wall of the ring resonator in (c). All images taken at 2kV acceleration. All images courtesy of Thorstein Wang.

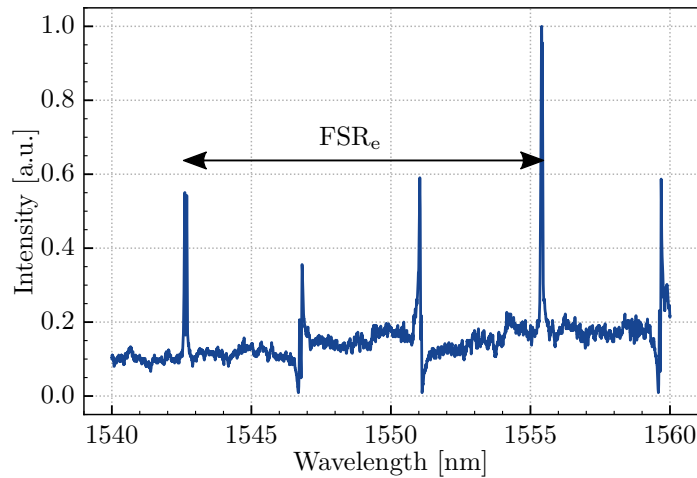


Figure 5.11: Transmission spectrum from the fabricated 240° MARC. The peaks are very narrow and the noise level is acceptable. The spectrum is unfortunately not properly balanced, but the response is still recognizable and well defined. $\text{FSR}_e \approx 12.8$ nm.

5.4 MARC Measurements

The following sections will present the measurements of the fabricated MARC devices, in the same order as they were presented in section 5.2. The fabricated devices will not be discussed in as much technical detail (i.e. Q-factor, FWHM, etc.) as the simulated devices were, as time did not allow for thorough testing and characterization of these MARCs. General comments on the transmission spectra will naturally be included, and estimations of FSR and FSR_e will be provided, along with brief comparisons with the simulated counterparts of each device.

The intensity of the laser in the transmission measurement setup is wavelength dependent, and although the laser is tunable over the range of 1500-1580 nm, the most uniform intensity profile was found to be the wavelength range of 1540-1560 nm. The wavelength sweeps of the fabricated MARCs were therefore performed over this range. Measurements were also performed over the same range as the simulated MARCs (1510-1550 nm), and these are (for completeness) presented with no further explanation in Appendix F, in figs. F.1-F.4. These graphs also demonstrate the wavelength dependent intensity profile of the laser source.

All transmission plots have been normalized.

5.4.1 240° MARC

The transmission measurement of MARC #15, a single-ring 240° sensor, is provided in fig. 5.11. The transmission spectrum shows very sharp peaks and relatively low noise. However, the spectrum is not properly balanced, and by visual inspection, the imbalance of the interferometer is determined to be approximately $\pi/3$ radians. The result of this imbalance is that the transmission spectrum features are in essence "inverted"; consider the theoretical spectrum for a 240° MARC (see Appendix A, fig. A.3), and simply invert the peaks into dips, and vice versa. Despite this imbalance, the spectrum is still very much unique and recognizable (as long as the imbalance is known to the user).

The FSR is measured to be approximately 4.2 nm, with $\text{FSR}_e \approx 12.8$ nm, which is consistent with the three-fold FSR increase of a 240° MARC. However, the measured FSR is significantly different to that of the corresponding simulated MARC, with the measured FSR being only 64% of the simulated value (6.53 nm). This deserves extra attention: Using eqn. 2.57, the effective

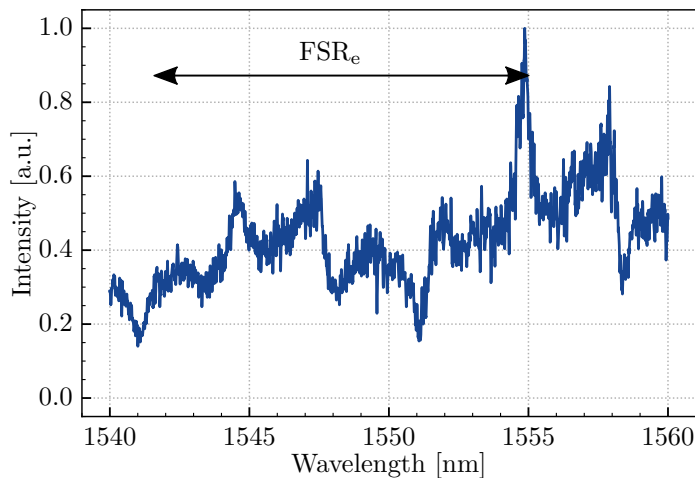


Figure 5.12: Transmission spectrum from the fabricated 90° MARC. This signal is characterized by high noise, and the features are poorly defined. A similar kind of imbalance to the simulated 90° MARC is visible. $\text{FSR}_e \approx 13.4 \text{ nm}$.

refractive index of the ring waveguide may be estimated. However, since the refractive index of a-Si is wavelength dependent in reality[60], the underlying assumption behind this formula becomes invalid. The formula cannot therefore be used to calculate n_{eff} directly, however it can be used to derive the *group* refractive index n_g instead. For $\text{FSR} = 4.2 \text{ nm}$, $r = 19.6 \mu\text{m}$, and $\lambda_0 = 1551 \text{ nm}$, we thus get $n_g = 4.65$, which in fact is a realistic value for a silicon-based waveguide of approximately $500 \times 220 \text{ nm}^2$ dimensions[61].

This difference between the simulated spectrum and the realized spectrum illuminates one of the major issues with the COMSOL simulations¹ as they have been performed in this project, namely that they assume a constant refractive index. The implementation of a wavelength dependent refractive index is rather straightforward in COMSOL, and this should be improved for future simulations of the MARC models.

Another feature of interest in the transmission spectrum shown, is the splitting of some peaks in the spectrum, most notably the Lorentzian features at approximately 1542.5 nm and 1555.5 nm. This is caused by resonance splitting, which is the result of a *backward propagating* mode in the ring waveguide[62]. These back-reflections can be induced by surface roughness in the ring waveguide[63], and these modes are able to couple with the forward propagating mode in the resonator, leading to deleterious effects[64]. In fact, even the presence of the bus waveguides themselves (which couple light into and out of the ring resonator), causes some degree of resonance splitting [65]. However, the resonance splitting present in this MARC spectrum does not significantly deteriorate the quality of the signal, and is therefore not considered problematic.

5.4.2 90° MARC

The transmission spectrum of the 90° MARC #10 is provided in fig. 5.12. This spectrum is unfortunately severely affected by noise, and the spectral characteristics of a 90° MARC are not immediately recognizable, although there are indications of Lorentzian and Fano-like features in the data. However, the peaks are not particularly narrow, and the signal is in general of very low quality.

The noise seen in the spectrum might be caused by several factors. First and foremost, it proved difficult to get a high-quality signal from any of the five fabricated 90° MARCs. Whether

¹And also the theoretical Python MARC script

this is due to a systematic flaw in the fabrication of these MARCs, or simply due to poorly designed MARCs, is not known. Some devices did show imperfections in and around the waveguide core during the SEM inspection. The most likely cause of noise in MARC #10, however, is noise from the laser source, detector noise, or a combination of these; the detected output signal was significantly lower for this MARC than for the other fabricated MARCs, and although the spectrum seems to have fairly defined peaks, this is most likely a result of the data normalization that has been performed.

Despite the noise, compared to the transmission spectrum of the simulated MARC shown in fig. 5.4, there are in fact similarities between the two spectra, in that they show more or less the same kind of imbalances. This particularly applies to the simulated wavelength region of 1520-1540 nm, which is very similar to the 1546-1560 nm region of the fabricated MARC spectrum. Although these regions do not overlap (ideally they would be identical, if the simulations implemented a wavelength-dependent refractive index), this does not make much of a practical difference, as the most important aspect of the sensor operation is to detect any relative shifts in the peaks of the spectrum.

Similarly to the case for the previous fabricated MARC, the measured FSR is approximately 3.2 nm, only 61% of the simulated FSR (5.22 nm). FSR_e was measured as 13.4 nm, but due to the badly defined features, the FSR and FSR_e are difficult to determine accurately.

The group refractive index can be determined using the procedure described in the previous section, and using $\text{FSR} = 3.2$ nm, $r = 24.9$ μm , and $\lambda_0 = 1551.38$ nm, we get $n_g = 4.81$, which is fairly in agreement with the group index reported for the fabricated 240° MARC.

The fact that the same imbalance is present in both the simulated and the fabricated MARC, might indicate that it is the design (i.e. the waveguide layout) of the 90° MARC itself that is not ideal. Simulations did show that this MARC was particularly difficult to balance properly, and a revision of the design process is needed before this particular MARC can see any real use.

5.4.3 135° MARC

The measured transmission spectrum of the 135° MARC #2 is shown in fig. 5.13. Of the three single-ring MARCs that were fabricated, this provided the highest-quality spectrum, particularly in terms of detector noise. Although the interferometer is not perfectly balanced²(the balance gradually deteriorates towards lower wavelengths), the overall pattern is highly distinguishable from the other two MARC spectra discussed. The peaks are narrow and very well defined, however there is a larger degree of resonance splitting in this spectrum, compared to that of the 240° MARC. Again, as the splitting itself is rather small, this is not considered to be problematic for the function of the MARC device.

The spectrum reveals an FSR of 1.5 nm, and an $\text{FSR}_e = 12.4$ nm, in adequate agreement with the theoretical 8x extension of the FSR provided by a 135° MARC. In terms of FSR, this MARC is no exception from the previous MARCs, and the measured FSR is approximately 63% of the simulated value (2.37 nm). Once again, using $\text{FSR} = 1.5$ nm, $r = 54.9$ μm , and $\lambda_0 = 1549.9$ nm, we get the group refractive index $n_g = 4.64$, in good agreement with the previous estimates for the other MARC devices.

5.4.4 Multiplexed MARC

During the post-fabrication SEM inspection, MARC #20 was deemed to be of the highest fabrication quality of the multiplexed MARCs. That structure was therefore tested in the transmission measurement setup, and its measured transmission response is shown in fig. 5.14. In this figure, the multiplexed signal has been offset and is shown side-by-side with the signals from its constituent rings (these are the same spectra as in figs. 5.11, 5.12 and 5.13, and do not neces-

²The feature at 1548.5 nm should ideally be a Lorentzian dip, not a Fano-like shape

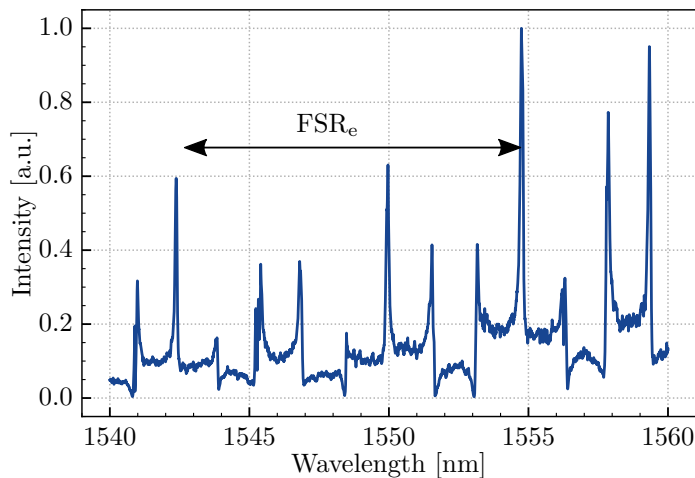


Figure 5.13: Transmission spectrum from the fabricated 135° MARC. The signal is very well defined, and features are sharp. Some resonance splitting is visible in some peaks and Fano-like features. $\text{FSR}_e \approx 12.4$ nm.

sarily accurately reflect the individual behavior of the actual rings in the *multiplexed* MARC). The single-ring MARC signals have been shifted in x to align with the peaks in the multiplexed spectrum.

The multiplexed MARC spectrum shows very clearly defined peaks across the wavelength sweep, significantly better than what the simulated spectrum shows in fig. 5.6. The peaks originating from the 135° and 240° rings are easily determined, however due to the poor quality signal acquired from the single-ring 90° MARC, the peaks from the 90° ring are more difficult to discern. A process of elimination may however be used, and the overlaid signal from the 90° MARC in fig. 5.14 is somewhat helpful for locating the corresponding peaks.

Fig. 5.15 shows IR photos of MARC #20 at three different resonant wavelengths, showing the behavior of the rings at resonance. What is immediately obvious, is the high intensity of light propagating in the through-port. This might indicate that the directional coupler into (and thus also out of) the MARC, does not in fact split the incident light equally into the interferometer. This should ideally be improved upon in future revisions of this MARC design.

Unfortunately, as (bio-)functionalization of the fabricated device falls outside the scope of this thesis, an actual measurement using the MARC as a sensor (similar to the simulated measurement provided in fig. 5.7) has not been done. However, the high-quality spectrum measured from the multiplexed MARC is very promising for any future investigations looking to prove the multiplexability of this particular MARC design.

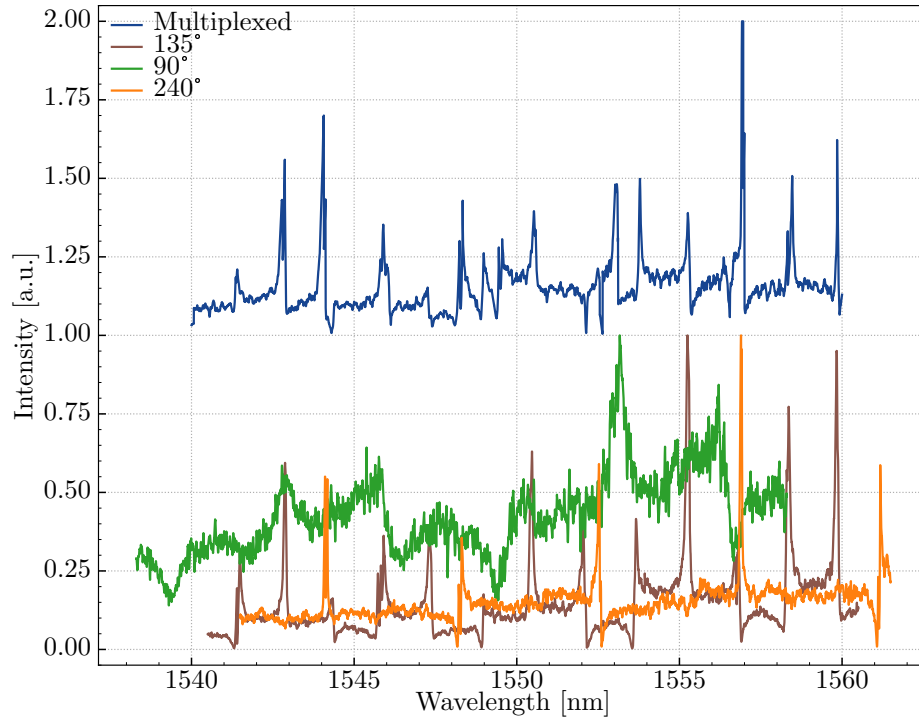


Figure 5.14: Transmission spectrum from the fabricated 3-ring MARC. The multiplexed signal shows narrow peaks and low background noise. The single-ring MARC transmission data is superposed to give an insight to each ring's contribution to the multiplexed spectrum. Note that each individual spectrum has been normalized; the amplitude of the 90° MARC is therefore not necessarily to scale with the other, more defined spectra. Spectra from the single-ring MARCs have been shifted in x to align with the multiplexed spectrum.

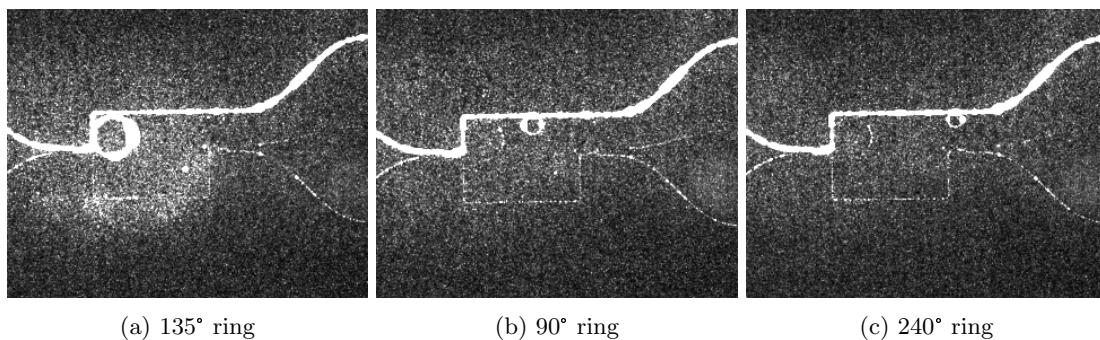


Figure 5.15: IR photography of MARC #20 at three resonant wavelengths. Notice the significantly increased brightness in the through-port waveguides, indicative of the 3dB coupler not splitting the incident light evenly between its two outputs.

5.5 Simulations vs. Fabricated MARCs

As discussed previously, two of the fabricated MARCs have shown signs of significant imbalance in their interferometers, and there might be several reasons for these issues. Unfortunately, time did not allow for a more thorough fabrication process, meaning that testing of individually fabricated structures and components (similar to what was done in the COMSOL simulations) could not be done. Although the design has been thoroughly simulated and optimized in COMSOL, there are still many factors at play when such devices are fabricated: The fabrication process itself might introduce impurities and defects of various sorts, affecting the waveguiding properties due to increased scattering loss or inefficient in-coupling. The deposition techniques used to deposit a-Si might result in a slightly different refractive index of the waveguide, which in turn might affect the power splitting of the directional couplers, as well as the coupling in and out of the ring resonators. Moreover, these coupling regions might not even be physically separated, if the EBL exposure was unsuccessful – although inspection using e.g. an SEM would allow for the detection of these issues early in the fabrication process.

Keeping this in mind, the balancing issues of the fabricated MARCs were not unexpected. However, as both the 240° and the 135° single-ring MARCs, as well as the multiplexed MARC, yielded fairly high-quality transmission spectra, there is no doubt that the simulations have been helpful in the design of the realized MARC, despite the minor adjustments required for optimal operation in the future. The agreements between the simulated and the fabricated 90° MARC spectra further reinforce the value and significance of the simulations as well.

The discrepancies reported in the FSR of the MARCs have, in this thesis, not led to any significant consequences. While the effects of n_{eff} vs. n_{g} in the expression for FSR (eqn. 2.57) have been discussed, another possible reason for the narrow FSRs measured, lies within the fabrication of the rings. If the fabricated rings turn out larger than what they were designed for, the FSR will also be reduced. However, for an FSR-reduction of approximately 38%, the rings would need to be approximately 75% larger than designed, using the calculated $nn_{\text{eff}} = 2.6036$ from COMSOL as the effective refractive index of the fabricated waveguides (combined with eqn. 2.57). This large increase in ring size was not seen in any of the fabricated MARCs, so ring fabrication deviations are not likely to be the cause of the reduced FSRs.

For future simulations, it is nonetheless of great interest to improve upon the COMSOL model, such that the value of the simulations is increased even further.

Chapter 6

Conclusion

The main goal of this work has been to design and optimize a multiplexed Mach-Zehnder interferometer-assisted ring resonator configuration (MARC) photonic sensor. The sensor was firstly designed and optimized using simulation software, before it was fabricated and accordingly characterized. The overlying motivation for this particular MARC sensor has been to develop a silicon-on-insulator (SOI) photonic integrated circuit (PIC) that would be applicable to future biosensor lab-on-chip (LOC) applications.

6.1 Simulations

The MARC devices were designed and simulated using COMSOL Multiphysics 5.4 / 6.0 (COMSOL), which is a commercially available simulation software based on the finite-elements method (FEM). The individual components of the sensors (i.e. the directional couplers, add-drop ring resonators and Mach-Zehnder interferometers (MZIs)) were simulated and optimized to ensure their proper function, preceding the design and simulation of complete single-ring MARC structures. The single-ring MARC structures differs in the angular separation of their add-drop ring resonators, and their configurations are 135°, 90°, and 240° angular separations. After the optimizations of individual single-ring MARCs, a multiplexed three-ring MARC was modeled and simulated, and its function as a sensor was briefly explored by introducing a fictitious measurand on the simulated model.

The simulations show that the single-ring MARC devices all provide an extended dynamic measurement range, due to their large effective free spectral range (FSR_e) of approximately 19 nm. While balancing the interferometers of the MARCs proved particularly difficult for the 90° MARC, the transmission spectra are all distinguishable and of fairly high quality. Deleterious reflections within the waveguide structures did have an effect on the simulated results, however the ripples caused by these reflections do not significantly deteriorate the signals from the sensors. These reflections were found to occur in the MZI of the MARC itself, and are suggestive of reflections occurring between the input- and output ports of the COMSOL model. The quality factors (Q) of each single-ring MARC were calculated to be approximately 9500, 7700, and 6900, for the 135°, 90° and 240° MARCs, respectively. The effects of these Q on their respective transmission responses were discussed.

When multiplexing the three rings into a single, multiplexed MARC, the resulting simulated transmission spectrum was of surprisingly low quality, suffering greatly from ripples making the interpretation of the spectrum difficult. Nonetheless, a fictitious measurand was introduced in the 240° ring by increasing the refractive index of the ring waveguide by $\Delta n = 0.010$. A resonant wavelength shift of $\Delta\lambda \approx 5.3$ nm was measured, illustrating the principles of a multiplexed MARC.

6.2 Fabrication

After simulations and optimizations were performed, the MARC devices were fabricated using NTNU NanoLab's facilities, tools and equipment. A 4" Si wafer with thermally pre-deposited SiO_2 was used as the substrate, on which amorphous silicon (a-Si) was deposited using plasma-enhanced

chemical vapor deposition (PECVD). The MARC design was patterned onto the sample using electron beam lithography (EBL) and etched using inductively coupled plasma-reactive ion etching (ICP-RIE). Inverted taper waveguide structures for in-coupling were patterned using near-UV photolithography. Following the fabrication, the transmission characteristics of the MARC devices were experimentally measured using a photonic waveguide transmission measurement setup.

The realized MARCs, of the same four configurations as described above, were all characterized using scanning electron microscopy (SEM), to verify their successful fabrication. The waveguide structures show good sidewall profiles and critical tolerances, although time did not allow for more rigorous analysis and testing of waveguide properties, like loss and the optimization of individual MARC components. In terms of their transmission responses, the 135° and 240° MARCs show indications of very low noise and very sharp peaks, indicative of good performance suitable for multiplexing. Although the single-ring 90° MARC was characterized by significant noise and imbalance, the multiplexed MARC showed excellent transmission response for all constituent rings. Time did unfortunately not allow for an actual refractive index change-measurement using this MARC device.

Although the shape of the transmission responses of the fabricated MARCs were in good agreement with the simulated devices, the measured free spectral range (FSR) (and as a consequence, the effective FSR, FSR_e as well) of the fabricated devices were consistently smaller than the simulated counterparts (measured FSRs were approximately 62% of the simulated FSRs). This has been discussed, and a likely reason for the discrepancy lies within the simulation models, as these have assumed wavelength-independent refractive indices for the materials used. All fabricated single-ring MARCs were measured to have effective FSRs (FSR_e) of approximately 12-13 nm.

Possible explanations for the interferometer imbalances seen in the fabricated MARCs were discussed as well, even though the fabricated MARCs in general have shown very similar behavior to that of their simulated counterparts.

6.3 Future Work

There are several aspects that can be improved upon if the work on this project should continue. The first of which revolves around the COMSOL model. Firstly, the 90° MARC proved to be difficult to balance properly, and a design revision is required to find a layout that results in less ripples and noise. This was backed up by the experimental findings, which showed that the fabricated 90° MARC also struggled with the same kind of imbalances as the simulated model (although fabrication defects may also have played a role in this case; in [3, 4], 90° MARCs have been fabricated successfully, although using a different geometry). Secondly, a wavelength dependent refractive index should be implemented, to enhance the realism of the model. This could also help with the FSR discrepancies discussed earlier.

Due to significant downtime of the electron beam lithography (EBL) equipment, the allotted time for the fabrication of the MARCs was short and did unfortunately not allow for thorough testing and optimizations of the fabricated MARCs. A natural next step is therefore to do some of the same optimizations to the fabricated MARCs, as was done in the COMSOL models. This includes testing and optimization of the directional 3dB couplers, the ring resonators and the interferometers, to name a few examples. Moreover, (bio-)functionalization of the fabricated sensor is also desirable, such that the measurement capabilities of the fabricated multiplexed MARC can be investigated.

Appendix A

Theoretical MARC Spectra

The theoretical MARC transmission spectra for the three different angular separation MARCs will be presented in this appendix. The spectra are calculated using the Python script presented in Appendix B. To allow for simpler comparison with the simulated results, the spectra are given assuming a ring radius that is identical to the simulated rings. The effective refractive index for all plots is set to $n_{\text{eff}} = 2.6036$, and the effective free spectral ranges (FSRs) are calculated using eqns. 2.68 and 2.69. The effective FSR(FSR_e) is also indicated in each plot.

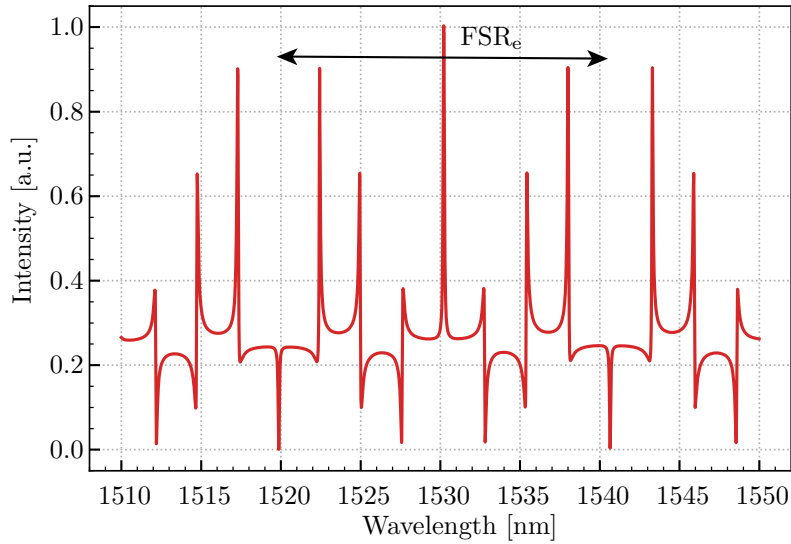


Figure A.1: Theoretical transmission spectrum of a single-ring 135° MARC. Ring radius is 55 μm , and $\text{FSR}_e = 20.8 \text{ nm}$.

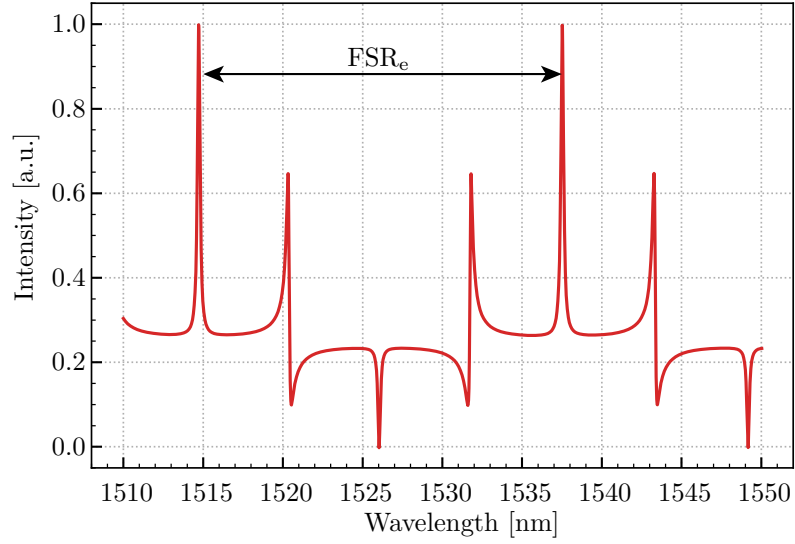


Figure A.2: Theoretical transmission spectrum of a single-ring 90° MARC. Ring radius is 25 μm , and $FSR_e = 22.9$ nm.

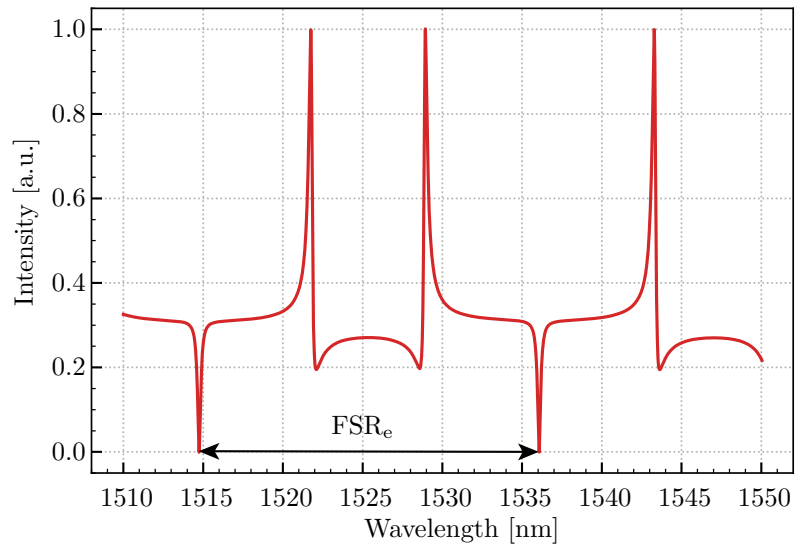


Figure A.3: Theoretical transmission spectrum of a single-ring 240° MARC. Ring radius is 20 μm , and $FSR_e = 21.5$ nm.

Appendix B

Python Code

Python¹ is a high-level interpreted programming language that provides a wide variety of powerful tools (packages and libraries) for scripting as well as numerical computations, making it a popular programming language across multiple fields. The syntax is simple to learn and highly human-readable, making it an ideal language for beginners.

In this section, the Python script used for modelling multiplexed MARCs will be presented with no further comments other than those already included in the script. In addition to this script, numerous other scripts have been written as well, mainly for processing and presenting the data from the COMSOL simulations. These will not be added, as they simply read data files and plot their contents, and as such are of little interest.

The Python code can also be found online, in the author's private GitHub² repository located at https://github.com/espehov1/MARC_Simulation/blob/main/MARC.py.

¹www.python.org

²<https://github.com/>

```

1 # This package is converted from a Matlab script provided by Mukesh Yadav.
2 # Translated and expanded upon by Espen Hovland, 2021,
3 # as part of my specialization project at NTNU.
4
5 import numpy as np
6 from fractions import Fraction
7
8 class Ring:
9     """
10    Add-drop ring resonator class. Calculates all relevant data when an instance is created.
11
12    Parameters:
13        wavelengths      (np.array): Wavelength sweep
14        radius            (float): Ring radius
15        angular_separation (float): Angular separation of drop- and through-port waveguides
16        coupling_coefficient (float): Self-coupling coefficient of the input waveguide
17        loss_coefficient   (float): Round-trip loss coefficient of the ring
18        n_eff             (float): Effective refractive index of the ring waveguide
19
20    Static methods:
21        FSR(ring_radius, n_eff, lambda_0) -> FSR in [m]
22
23    Available data (member variables):
24        .r                (float): Radius of ring
25        .ang_sep          (float): Angular sep. of through- and drop-port
26        .a                (float): Round-trip loss coefficient of the ring
27        .n_eff            (float): Effective refractive index
28        .t1               (float): Self-coupling coefficient of input waveguide
29        .t2               (float): Self-coupling coefficient of drop-port waveguide
30        .fsr              (float): Free spectral range
31        .fsr_eff          (float): Effective FSR (single-ring MARC)
32        .dp_amplitude     (np.array): Drop-port amplitude response
33        .tp_amplitude     (np.array): Through-port amplitude response
34        .dp_intensity     (np.array): Drop-port intensity response
35        .tp_intensity     (np.array): Through-port intensity response
36        .dp_phase         (np.array): Drop-port phase response
37        .tp_phase         (np.array): Through-port phase response
38    """
39    def __init__(self,
40                wavelengths,
41                radius: float,
42                angular_separation: float,
43                coupling_coefficient: float = 0.95,
44                loss_coefficient: float = 1,
45                n_eff: float = 3.9 ):
46        self.r = radius # [m] Radius of ring
47        self.ang_sep = angular_separation # [deg] Angular sep. of drop- and through-port
48        self.a = loss_coefficient # [1] Round-trip loss coefficient
49        self.n_eff = n_eff # [1] Effective refractive index
50        self.t1 = coupling_coefficient # [1] Self-coupling coeff. of input waveguide
51        self.t2 = self.t1 / self.a # [1] Self-coupling coeff. of drop waveguide
52
53        phi = 2 * np.pi * self.n_eff * 2 * np.pi * self.r / wavelengths # Round-trip phase shifts
54        traversed = self.ang_sep / 360 # Proportion of ring travelled
55        act_shift = phi * traversed # Actual phase shift
56
57        # Amplitude response at drop-port
58        self.dp_amplitude = np.asarray(
59            (-(np.sqrt(1-self.t1**2) * np.sqrt(1-self.t2**2) * np.power(self.a, traversed)
60             * np.exp(1j*act_shift)) / ( 1 - (self.t1 * self.t2 * self.a * np.exp(1j * phi)))),
61            dtype=complex
62        )
63        # Amplitude response at through-port
64        self.tp_amplitude = np.asarray(
65            (self.t1 - self.t2 * self.a * np.exp(1j * phi))
66            / (1 - self.t1 * self.t2 * self.a * np.exp(1j * phi)),
67            dtype=complex
68        )
69
70        # Intensity response
71        self.dp_intensity = np.asarray(np.abs(self.dp_amplitude)**2, dtype=float) # Drop-port
72        self.tp_intensity = np.asarray(np.abs(self.tp_amplitude)**2, dtype=float) # Through-port
73
74        # Phase response
75        self.dp_phase = np.unwrap(np.angle(self.dp_amplitude)) # Drop-port
76        self.tp_phase = np.unwrap(np.angle(self.tp_amplitude)) # Through-port
77
78        # Get the FSR, as if the center frequency is resonant frequency (approximation)
79        self.fsr = self.get_FSR(self.r, self.n_eff, wavelengths[len(wavelengths)//2])
80
81        # Calculate effective FSR (for single-ring MARCs)
82        L = 1 / traversed
83        frac = Fraction.from_float(L).limit_denominator() # Find the reduced fraction N/M
84        N = frac.numerator
85        self.fsr_eff: float = N * self.fsr # [nm]
86
87        return
88
89    @staticmethod
90    def get_FSR(ring_radius: float, n_eff: float, lambda_0: float = 1550e-9) -> float:

```

```

91     """
92     Calculate the (approximate) FSR.
93     Parameters:
94         ring_radius (float): [m] Radius of ring
95         n_eff       (float): [1] Effective refractive index of ring
96         lambda_0    (float): [m] Resonance wavelength of ring.
97                             Defaults to 1550 nm
98     Returns:
99         Calculated FSR [m]
100    """
101    return lambda_0**2 / (n_eff**2*np.pi*ring_radius)
102
103
104    #####
105    #####
106
107
108    class MZI:
109        """ Mach-Zehnder interferometer base class """
110        def __init__(self, initial_phase: float = 0):
111            self.initial_phase = initial_phase # Phase imbalance of MZI
112
113        @staticmethod
114        def get_trans(amplitude, phi_1, phi_2) -> np.array:
115            """
116            The interference equation, for calculating the amplitude transmittance.
117
118            Parameters:
119                amplitude (np.array): The complex amplitude of the signal from the affected arm.
120                phi_1      (np.array): The phase of the affected arm.
121                phi_2      (np.array): The phase of the unaffected arm.
122
123            Returns:
124                t          (np.array): The transmittance of the MZ interferometer.
125            """
126            t = 0.5*np.exp(0.5j*(phi_1+phi_2+np.pi))*(np.abs(amplitude)*np.exp(0.5j*(phi_1-phi_2))
127                + np.exp(-0.5j*(phi_1-phi_2)))
128            return t
129
130    #####
131    #####
132
133
134    class MARC(MZI):
135        """
136        Multi-ring MARC class. Calculates all data upon creating an instance.
137
138        Parameters:
139            wavelengths (np.array): Wavelength sweep
140            rings        (Ring):     Rings to include in the MARC
141            initial_phase (float):   Phase imbalance from MZI
142
143        Available data (member variables):
144            .num_rings (int):     number of rings in MARC
145            .rings     (list):    list of rings in device
146            .amplitude (np.array): output amplitude response of device
147            .intensity (np.array): output intensity response of device
148            .tp_intensity (np.array): through-port intensity response of device
149            .phase_output (np.array): output phase response of device
150        """
151        def __init__(self, wavelengths, *rings: Ring, initial_phase: float = 0):
152            super().__init__(initial_phase=initial_phase)
153
154            self.num_rings = len(rings)
155            self.rings     = [r for r in rings]
156
157            amp_post_rings = np.zeros(len(wavelengths), dtype="complex") # Amplitude resp. of all rings
158            amp_tp         = np.ones(len(wavelengths), dtype="complex") # Amplitude resp. of through-port
159
160            for idx, ring in enumerate(self.rings):
161                amp_ring = ring.dp_amplitude # Drop-port amplitude transmission of last ring
162                for i in range(0, idx):
163                    amp_ring *= self.rings[i].tp_amplitude
164                amp_post_rings += amp_ring
165
166            for ring in self.rings:
167                amp_tp *= ring.tp_amplitude
168
169            amplitude = self.get_trans(amp_post_rings, np.unwrap(np.angle(amp_post_rings)), self.initial_phase)
170
171            self.amplitude = amplitude / np.max(np.abs(amplitude)) # Normalize the amplitude
172            self.intensity = np.asarray(np.abs(self.amplitude)**2, dtype=float)
173            self.tp_intensity = np.asarray(np.abs(amp_tp)**2, dtype=float)
174            self.phase_output = np.unwrap(np.angle(self.amplitude))
175
176            return
177
178    #####
179    #####

```


Appendix C

Lithography Mask Design

For creating the lithography mask design, the COMSOL model design was used as a starting point. The model parameters were extracted from COMSOL, and the Nazca¹ Python package was used to create the mask layout.

C.1 Extracting Model Parameters

The COMSOL model geometry consists of simple shapes like rectangles and circles, each having parameters for their size (width, height, radius) and their location (x and y coordinates). Using these parameters makes it simple to recreate the model in a suitable lithography mask file (e.g. in the .GDS-format).

COMSOL provides the option to save parameter lists to external files, which stores the parameter names along with their values and their comments as a comma-separated .txt file. This file can then either be read programmatically (using e.g. a custom Python script), or, as was done in this work, the parameters and their values were manually entered as global variables in a Python script. This makes the script itself appear rather complex, however it remains flexible, and changing parameters is simple.

One thing to do keep in mind, however, is that any COMSOL specific function, e.g. `sin()`, `cos()` and `floor()` needs to be replaced with Python-compatible counterparts, e.g. from the Python modules `math` or `numpy`². Moreover, COMSOL also allows for units to be specified inside mathematical expressions (such as $a = 5[\text{nm}] + 19[\text{um}]$, or $b = \sin(45[\text{deg}])$, including many more), which are not supported by the Python syntax. In this work, all length units were therefore converted into micrometers, and all angular units were converted into radians, eliminating the need for specifying units in the expressions.

C.2 Building the Mask Layout

Creating the mask layout was very simple using the Nazca package, and the procedure will be briefly described in this section. The notion is that each waveguide element is placed sequentially, with the new section's "input" being connected to the "output" of the previous section. For continuous waveguide structures, this virtually eliminates the need for absolute or relative coordinates of each individual element, significantly simplifying the design process.

For MARC structures, where the ring resonators are physically isolated from the rest of the waveguide structures, the rings themselves may be placed at absolute coordinates (e.g. from the parameter list from COMSOL). Aligning the remaining structures to the rings is then as simple as placing *one* of the elements of the interferometer waveguide at the correct coordinate, and consecutively building the rest of the geometry as described above.

¹<https://nazca-design.org/>

²<https://numpy.org/>

Appendix D

Notes on COMSOL Resource Usage

Numerical computations can be very computationally demanding, and for large simulations/systems, the required computer capabilities may be significant. In this project, the resource usage of COMSOL's simulations were reduced significantly by adjusting the parameters linked to two resources, namely computer storage and memory.

D.1 Storage Usage

By default, all results are stored at all steps of a parametric sweep in COMSOL, and as a result, the model files quickly reach very large file sizes. A few gigabytes of storage are needed for a relatively simple 100-step simulation of a single-ring MARC, however reductions in file size can be made quite easily. These improvements mainly come in two areas: 1) the physics aspects of the model, and 2) the storage settings of COMSOL itself.

First and foremost, for a problem where only the fundamental TE mode is being simulated, COMSOL can be set up to only solve for the out-of-plane vector components. The other vector components are negligible, and this reduces the degrees of freedom needed to be solved by two thirds.

The granularity of the mesh is also an important factor, so larger and less intricate parts of the geometry can be segmented into larger sections, whereas smaller features are assigned a finer mesh. As long as the mesh is of adequate quality, the computations can be additionally sped up by using linear discretization instead of the more demanding quadratic variant.

The main challenge with a parametric sweep, in terms of storage, is that the solution at each step requires a certain storage space, as a lot of data is stored in each solution. As the number of sweep steps increases, so too does the required storage space. However, it is rarely the case that *all* aspects of all solutions are interesting; in this project, for example, only the transmittance at the ports as well as the phase response of the MARCs were of interest. In other words, only a fraction of the available data was useful. This challenge can be circumvented by instead using the *probe* feature built in to COMSOL. Each probe is set to "listen" to one variable only, and the data is stored in an accumulative table in an external file as the parameter sweep progresses. This also provides the additional benefit in the event of an unexpected simulation-/computer crash; the data is stored continuously and the results from the entire computation up to the point of failure is safe. Additionally, COMSOL is also set to only store the last solution – contrary to the default of *all* solutions, and this significantly reduces the storage usage of the model.

D.2 Memory Usage

The default solver for COMSOL is MUMPS¹, however the PARDISO² solver was tested as well, as it is arguably more effective in lower RAM computers and for problems with a large number of degrees of freedom. MUMPS was however experienced to be the fastest of the two, and was

¹<http://mumps.enseeiht.fr/>

²<https://www.pardiso-project.org/>

therefore used. Both MUMPS and PARDISO come pre-installed in COMSOL, and changing solvers is done via a simple drop-down menu in the solver configurations.

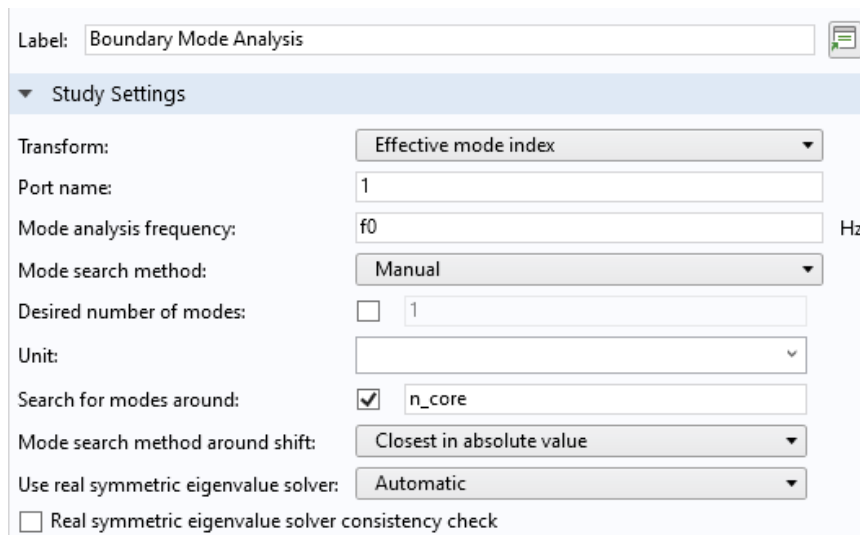
If the computer has sufficient memory (RAM) available, computation speed may be increased slightly by unchecking the *out-of-core* setting for each individual solver in the study step. This requires all computations to be performed in the processor core using the available RAM, which is significantly faster than storing and handling the data in the disk storage. This was done in this project.

Appendix E

Additional COMSOL Parameters

E.1 Boundary Mode Analyses

The settings for the boundary mode analysis of Port 1 are shown in fig. E.1. The parameter for the mode analysis frequency, f_0 , is given by $f_0 = c_const/wl_0$, where wl_0 is the wavelength and c_const is the built-in variable for the speed of light in free space (in COMSOL, $c_const = 2.9979 \cdot 10^8 \text{m/s}$). The settings for the other boundary mode analyses (i.e. ports) are identical, except for the "Port name" parameter.



The image shows a software interface for configuring a Boundary Mode Analysis. The label is "Boundary Mode Analysis". Under "Study Settings", the following parameters are set:

- Transform: Effective mode index
- Port name: 1
- Mode analysis frequency: f_0 Hz
- Mode search method: Manual
- Desired number of modes: 1
- Unit: (empty)
- Search for modes around: n_core
- Mode search method around shift: Closest in absolute value
- Use real symmetric eigenvalue solver: Automatic
- Real symmetric eigenvalue solver consistency check

Figure E.1: Applied settings for the boundary mode analysis of Port 1.

Appendix F

Additional MARC Measurements

Lab measurements of the three single-ring MARCs and the multiplexed MARC, in the wavelength range 1510-1550 nm, are presented below. The non-uniform intensity profile of the laser is clear from these plots.

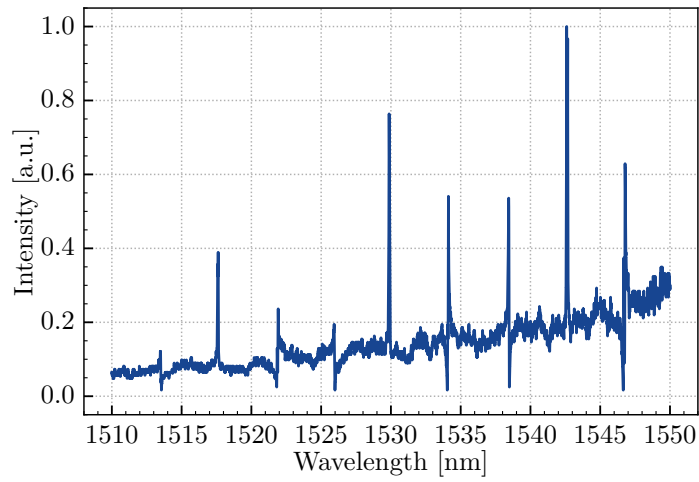


Figure F.1: Wide transmission spectrum of the fabricated 240° single-ring MARC.

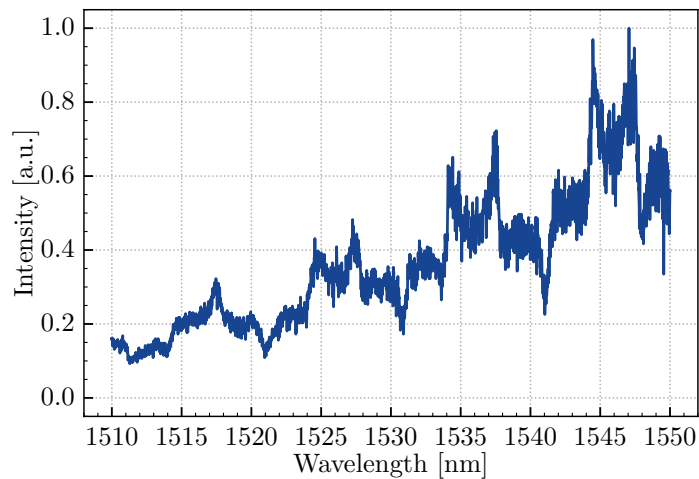


Figure F.2: Wide transmission spectrum of the fabricated 90° single-ring MARC.

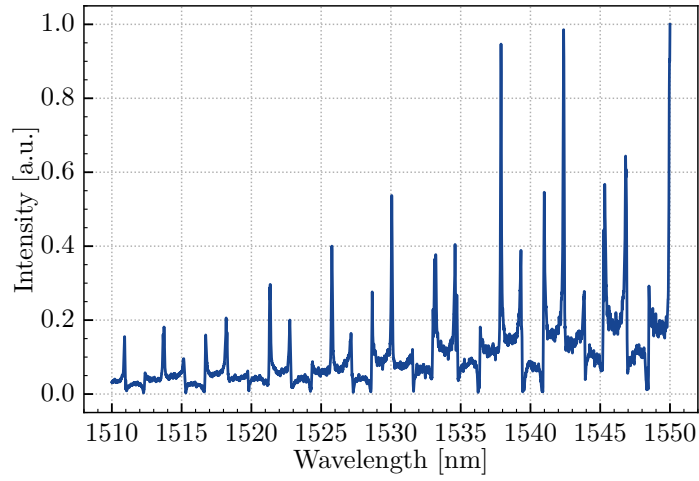


Figure F.3: Wide transmission spectrum of the fabricated 135° single-ring MARC.

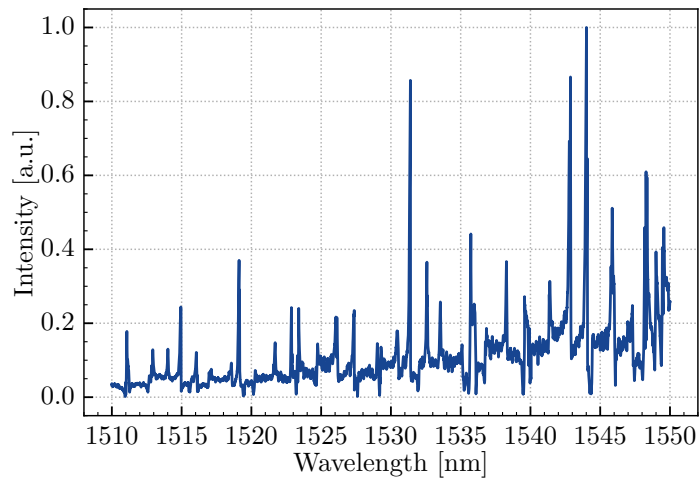


Figure F.4: Wide transmission spectrum of the fabricated multiplexed MARC.

References

- [1] Espen Hovland. “Multiplexing Mach-Zehnder Interferometer-Assisted Ring Resonator Configuration (MARC) Photonic Sensors”. Project thesis. Norwegian University of Science and Technology, 2022.
- [2] Centre For Digital Life Norway. *Lab-on-a-chip - Centre for Digital Life Norway*. 2021. URL: <https://www.digitallifenorway.org/research/lab-on-a-chip/>.
- [3] Mukesh Yadav et al. “Spectral shaping of ring resonator transmission response”. In: *Optics Express* 29.3 (Feb. 2021), p. 3764. ISSN: 1094-4087. DOI: 10.1364/oe.415683. URL: <https://www.osapublishing.org/abstract.cfm?URI=oe-29-3-3764>.
- [4] Mukesh Yadav and Astrid Aksnes. “Multiplexed Mach-Zehnder interferometer assisted ring resonator sensor”. In: (2021).
- [5] Syril D Pettit et al. “‘All In’: a pragmatic framework for COVID-19 testing and action on a global scale”. In: *EMBO Molecular Medicine* 12.6 (June 2020). ISSN: 1757-4676. DOI: 10.15252/emmm.202012634. URL: <https://onlinelibrary.wiley.com/doi/10.15252/emmm.202012634>.
- [6] Yukari C. Manabe, Joshua S. Sharfstein, and Katrina Armstrong. “The Need for More and Better Testing for COVID-19”. In: *JAMA* 324.21 (Dec. 2020), p. 2153. ISSN: 0098-7484. DOI: 10.1001/jama.2020.21694. URL: <https://jamanetwork.com/journals/jama/fullarticle/2773129>.
- [7] Patrick Steglich et al. “Optical Biosensors Based on Silicon-On-Insulator Ring Resonators: A Review”. In: *Molecules* 24.3 (Jan. 2019), p. 519. ISSN: 1420-3049. DOI: 10.3390/molecules24030519. URL: <http://www.mdpi.com/1420-3049/24/3/519>.
- [8] Koji Yamada et al. “High-performance silicon photonics technology for telecommunications applications”. In: *Science and Technology of Advanced Materials* 15.2 (Apr. 2014), p. 024603. ISSN: 1468-6996. DOI: 10.1088/1468-6996/15/2/024603. URL: <https://www.tandfonline.com/doi/full/10.1088/1468-6996/15/2/024603>.
- [9] W. Bogaerts et al. “Basic structures for photonic integrated circuits in Silicon-on-insulator”. In: *Optics Express* 12.8 (Apr. 2004), p. 1583. ISSN: 1094-4087. DOI: 10.1364/OPEX.12.001583. URL: <https://www.osapublishing.org/abstract.cfm?URI=oe-12-8-1583>.
- [10] Bahaa E.A. Saleh and Malvin Carl Teich. *Fundamentals of Photonics*. 3rd. John Wiley & Sons, Inc, 2019, p. 1370. ISBN: 9781119506874.
- [11] David K Cheng. *Field and Wave Electromagnetics*. 2nd. Essex: Pearson Education Limited, 2014, p. 704. ISBN: 9781292026565.
- [12] Mildred Dresselhaus. *Solid State Physics Part II Optical Properties of Solids*. 1999. URL: <http://web.mit.edu/course/6/6.732/www/6.732-pt2.pdf>.
- [13] Kensuke Ogawa et al. “Silicon Mach-Zehnder modulator of extinction ratio beyond 10 dB at 100-125 Gbps”. In: *Optics Express* 19.26 (Dec. 2011), B26. ISSN: 1094-4087. DOI: 10.1364/OE.19.000B26. URL: <https://www.osapublishing.org/oe/abstract.cfm?uri=oe-19-26-B26>.
- [14] B. P. Abbott et al. “Observation of Gravitational Waves from a Binary Black Hole Merger”. In: *Physical Review Letters* 116.6 (Feb. 2016), p. 061102. ISSN: 0031-9007. DOI: 10.1103/PhysRevLett.116.061102. URL: <https://link.aps.org/doi/10.1103/PhysRevLett.116.061102>.

- [15] Albrecht Brandenburg et al. “Interferometric sensor for detection of surface-bound bioreactions”. In: *Applied Optics* 39.34 (Dec. 2000), p. 6396. ISSN: 0003-6935. DOI: 10.1364/AO.39.006396. URL: <https://www.osapublishing.org/abstract.cfm?URI=ao-39-34-6396>.
- [16] Graham T. Reed and Andrew P. Knights. *Silicon Photonics*. Chichester, UK: John Wiley & Sons, Ltd, Jan. 2004. ISBN: 9780470014189. DOI: 10.1002/0470014180. URL: <http://doi.wiley.com/10.1002/0470014180>.
- [17] Kimmo Solehmainen et al. “Adiabatic and Multimode Interference Couplers on Silicon-on-Insulator”. In: *IEEE Photonics Technology Letters* 18.21 (Nov. 2006), pp. 2287–2289. ISSN: 1041-1135. DOI: 10.1109/LPT.2006.885305. URL: <http://ieeexplore.ieee.org/document/1715403/>.
- [18] A. I. Stanley et al. “Mach-Zehnder Interferometer: A Review of a Perfect All-Optical Switching Structure”. In: *Proceedings of the International Conference on Recent Cognizance in Wireless Communication & Image Processing*. New Delhi: Springer India, 2016, pp. 415–425. DOI: 10.1007/978-81-322-2638-3_48. URL: http://link.springer.com/10.1007/978-81-322-2638-3_{_}48.
- [19] Daniel K. Sparacin. “Process and Design Techniques for Low Loss Integrated Silicon Photonics”. PhD thesis. Massachusetts Institute of Technology, 2006, p. 260. URL: <https://dspace.mit.edu/handle/1721.1/37690>.
- [20] Wim Bogaerts. “Nanophotonic Waveguides and Photonic Crystals in Silicon-on-Insulator”. PhD thesis. Ghent University, 2004.
- [21] L. Vivien and L. Pavesi. *Handbook of Silicon Photonics*. Ed. by E. Roy Pike and Robert G. W. Brown. 1st ed. Taylor & Francis, 2013, p. 852. ISBN: 9781439836101.
- [22] Vilson R. Almeida, Roberto R. Panepucci, and Michal Lipson. “Nanotaper for compact mode conversion”. In: *Optics Letters* 28.15 (2003), pp. 1302–1304.
- [23] T. Shoji et al. “Low loss mode size converter from 0.3 μm square Si wire waveguides to singlemode fibres”. In: *Electronics Letters* 38.25 (2002), p. 1669. ISSN: 00135194. DOI: 10.1049/el:20021185. URL: https://digital-library.theiet.org/content/journals/10.1049/el_{_}20021185.
- [24] Minhao Pu et al. “Ultra-low-loss inverted taper coupler for silicon-on-insulator ridge waveguide”. In: *Optics Communications* 283.19 (Oct. 2010), pp. 3678–3682. ISSN: 00304018. DOI: 10.1016/j.optcom.2010.05.034. URL: <https://linkinghub.elsevier.com/retrieve/pii/S0030401810005018>.
- [25] Rong Sun. “Advanced materials, process, and designs for silicon photonic integration”. PhD thesis. 2009. URL: <http://hdl.handle.net/1721.1/46678>.
- [26] J. S. Foresi et al. “Losses in polycrystalline silicon waveguides”. In: *Applied Physics Letters* 68.15 (1996), pp. 2052–2054. ISSN: 0003-6951. DOI: 10.1063/1.116300. URL: <http://aip.scitation.org/doi/10.1063/1.116300>.
- [27] Anuradha M. Agarwal et al. “Low-loss polycrystalline silicon waveguides for silicon photonics”. In: *Journal of Applied Physics* 80.11 (1996), pp. 6120–6123. ISSN: 0021-8979. DOI: 10.1063/1.363686. URL: <http://aip.scitation.org/doi/10.1063/1.363686>.
- [28] A. Harke, M. Krause, and J. Mueller. “Low-loss singlemode amorphous silicon waveguides”. In: *Electronics Letters* 41.25 (2005), p. 1377. ISSN: 00135194. DOI: 10.1049/el:20052387. URL: https://digital-library.theiet.org/content/journals/10.1049/el_{_}20052387.
- [29] F. Grillot et al. “Propagation loss in single-mode ultrasmall square silicon-on-insulator optical waveguides”. In: *Journal of Lightwave Technology* 24.2 (Feb. 2006), pp. 891–896. ISSN: 0733-8724. DOI: 10.1109/JLT.2005.861939. URL: <http://ieeexplore.ieee.org/document/1593762/>.

- [30] Kevin K Lee. “Transmission and routing of optical signals in on-chip waveguides for silicon microphotronics”. PhD thesis. 2001. URL: <http://hdl.handle.net/1721.1/8768>.
- [31] Cyril Bellegarde et al. “Improvement of Sidewall Roughness of Submicron SOI Waveguides by Hydrogen Plasma and Annealing”. In: *IEEE Photonics Technology Letters* 30.7 (Apr. 2018), pp. 591–594. ISSN: 1041-1135. DOI: 10.1109/LPT.2018.2791631. URL: <http://ieeexplore.ieee.org/document/8253489/>.
- [32] F. Gao et al. “Improvement of sidewall surface roughness in silicon-on-insulator rib waveguides”. In: *Applied Physics B* 81.5 (Sept. 2005), pp. 691–694. ISSN: 0946-2171. DOI: 10.1007/s00340-005-1951-x. URL: <http://link.springer.com/10.1007/s00340-005-1951-x>.
- [33] P. Dumon et al. “Low-Loss SOI Photonic Wires and Ring Resonators Fabricated With Deep UV Lithography”. In: *IEEE Photonics Technology Letters* 16.5 (May 2004), pp. 1328–1330. ISSN: 1041-1135. DOI: 10.1109/LPT.2004.826025. URL: <http://ieeexplore.ieee.org/document/1291500/>.
- [34] Yurii A. Vlasov and Sharee J. McNab. “Losses in single-mode silicon-on-insulator strip waveguides and bends”. In: *Optics Express* 12.8 (2004), p. 1622. ISSN: 1094-4087. DOI: 10.1364/OPEX.12.001622. URL: <https://www.osapublishing.org/oe/abstract.cfm?uri=oe-12-8-1622>.
- [35] S. Feng et al. “Silicon photonics: from a microresonator perspective”. In: *Laser & Photonics Reviews* 6.2 (Apr. 2012), pp. 145–177. ISSN: 18638880. DOI: 10.1002/lpor.201100020. URL: <https://onlinelibrary.wiley.com/doi/10.1002/lpor.201100020>.
- [36] Dominik G. Rabus. “Integrated Ring Resonators”. In: vol. 127. Springer Series in Optical Sciences. Berlin, Heidelberg: Springer Berlin Heidelberg, 2007. Chap. 2. ISBN: 978-3-540-68786-3. DOI: 10.1007/978-3-540-68788-7. URL: <http://link.springer.com/10.1007/978-3-540-68788-7>.
- [37] Sarvagya Dwivedi et al. “Measurements of Effective Refractive Index of SOI Waveguides using Interferometers”. In: *Advanced Photonics 2015*. Washington, D.C.: OSA, 2015, IM2A.6. ISBN: 978-1-55752-000-5. DOI: 10.1364/IPRSN.2015.IM2A.6. URL: <https://opg.optica.org/abstract.cfm?URI=IPRSN-2015-IM2A.6>.
- [38] Linjie Zhou and Andrew W. Poon. “Fano resonance-based electrically reconfigurable add-drop filters in silicon microring resonator-coupled Mach-Zehnder interferometers”. In: *Optics Letters* 32.7 (Apr. 2007), p. 781. ISSN: 0146-9592. DOI: 10.1364/OL.32.000781. URL: <https://www.osapublishing.org/abstract.cfm?URI=ol-32-7-781>.
- [39] Bradley J. Frey, Douglas B. Leviton, and Timothy J. Madison. “Temperature-dependent refractive index of silicon and germanium”. In: ed. by Eli Atad-Ettedgui, Joseph Antebi, and Dietrich Lemke. June 2006, 62732J. DOI: 10.1117/12.672850. URL: <http://proceedings.spiedigitallibrary.org/proceeding.aspx?doi=10.1117/12.672850>.
- [40] R. Soref and B. Bennett. “Electrooptical effects in silicon”. In: *IEEE Journal of Quantum Electronics* 23.1 (Jan. 1987), pp. 123–129. ISSN: 0018-9197. DOI: 10.1109/JQE.1987.1073206. URL: <http://ieeexplore.ieee.org/document/1073206/>.
- [41] Xudong Fan et al. “Sensitive optical biosensors for unlabeled targets: A review”. In: *Analytica Chimica Acta* 620.1-2 (July 2008), pp. 8–26. ISSN: 00032670. DOI: 10.1016/j.aca.2008.05.022. URL: <https://linkinghub.elsevier.com/retrieve/pii/S0003267008009343>.
- [42] Kin S. Chiang. “Performance of the effective-index method for the analysis of dielectric waveguides”. In: *Optics Letters* 16.10 (May 1991), p. 714. ISSN: 0146-9592. DOI: 10.1364/OL.16.000714. URL: <https://opg.optica.org/abstract.cfm?URI=ol-16-10-714>.
- [43] Min Qiu. “Effective index method for heterostructure-slab-waveguide-based two-dimensional photonic crystals”. In: *Applied Physics Letters* 81.7 (Aug. 2002), pp. 1163–1165. ISSN: 0003-6951. DOI: 10.1063/1.1500774. URL: <http://aip.scitation.org/doi/10.1063/1.1500774>.

- [44] Michael Quirk and Julian Serda. *Semiconductor manufacturing technology*. Vol. 1. Prentice Hall Upper Saddle River, NJ, 2001.
- [45] Milton Ohring. *Materials Science of Thin Films*. Elsevier, 2002. ISBN: 9780125249751. DOI: 10.1016/B978-0-12-524975-1.X5000-9. URL: <https://linkinghub.elsevier.com/retrieve/pii/B9780125249751X50009>.
- [46] Lars Grønmark Holmen. “Simulation and Fabrication of a Photonic Crystal Mach-Zehnder Interferometer”. Master’s thesis. Norwegian University of Science and Technology, 2016.
- [47] Karthik Narayanan. “Hydrogenated Amorphous Silicon Photonics”. PhD thesis. Rochester Institute of Technology, 2011.
- [48] M Stepanova and S Dew. *Nanofabrication*. Ed. by Maria Stepanova and Steven Dew. Vienna: Springer Vienna, 2012. ISBN: 978-3-7091-0423-1. DOI: 10.1007/978-3-7091-0424-8. URL: <http://link.springer.com/10.1007/978-3-7091-0424-8>.
- [49] Alexei L. Bogdanov, Jean Lapointe, and Jens H. Schmid. “Electron-beam lithography for photonic waveguide fabrication: Measurement of the effect of field stitching errors on optical performance and evaluation of a new compensation method”. In: *Journal of Vacuum Science & Technology B, Nanotechnology and Microelectronics: Materials, Processing, Measurement, and Phenomena* 30.3 (May 2012), p. 031606. ISSN: 2166-2746. DOI: 10.1116/1.3700439. URL: <http://avs.scitation.org/doi/10.1116/1.3700439>.
- [50] Fouad Karouta. “A practical approach to reactive ion etching”. In: *Journal of Physics D: Applied Physics* 47.23 (June 2014), p. 233501. ISSN: 0022-3727. DOI: 10.1088/0022-3727/47/23/233501. URL: <https://iopscience.iop.org/article/10.1088/0022-3727/47/23/233501>.
- [51] P.H. Yih, V. Saxena, and A.J. Steckl. “A Review of SiC Reactive Ion Etching in Fluorinated Plasmas”. In: *physica status solidi (b)* 202.1 (July 1997), pp. 605–642. ISSN: 0370-1972. DOI: 10.1002/1521-3951(199707)202:1<605::AID-PSSB605>3.0.CO;2-Y. URL: [https://onlinelibrary.wiley.com/doi/10.1002/1521-3951\(199707\)202:1%7D3C605::AID-PSSB605%7D3E3.0.CO;2-Y](https://onlinelibrary.wiley.com/doi/10.1002/1521-3951(199707)202:1%7D3C605::AID-PSSB605%7D3E3.0.CO;2-Y).
- [52] C. J. Mogab. “The Loading Effect in Plasma Etching”. In: *Journal of The Electrochemical Society* 124.8 (Aug. 1977), pp. 1262–1268. ISSN: 0013-4651. DOI: 10.1149/1.2133542. URL: <https://iopscience.iop.org/article/10.1149/1.2133542>.
- [53] Rob Legtenberg et al. “Anisotropic Reactive Ion Etching of Silicon Using SF₆ / O₂ / CHF₃ Gas Mixtures”. In: *Journal of The Electrochemical Society* 142.6 (June 1995), pp. 2020–2028. ISSN: 0013-4651. DOI: 10.1149/1.2044234. URL: <https://iopscience.iop.org/article/10.1149/1.2044234>.
- [54] A.W. Bogalecki and M. du Plessis. “Design and Manufacture of Quantum-Confined SI Light Sources”. In: *SAIEE Africa Research Journal* 101.1 (2010), pp. 11–16. ISSN: 1991-1696. DOI: 10.23919/SAIEE.2010.8532214. URL: <https://ieeexplore.ieee.org/document/8532214/>.
- [55] Guozhong Cao and Ying Wang. *Nanostructures and Nanomaterials*. Vol. 2. World Scientific Series in Nanoscience and Nanotechnology. WORLD SCIENTIFIC, Jan. 2011. ISBN: 978-981-4322-50-8. DOI: 10.1142/7885. URL: <https://www.worldscientific.com/worldscibooks/10.1142/7885>.
- [56] Thermo Fisher. *Scanning Electron Microscopy — Electrons in SEM*. URL: <https://www.thermofisher.com/no/en/home/materials-science/learning-center/applications/sem-electrons.html>.
- [57] Edward D. Palik. *Handbook of Optical Constants of Solids*. Academic Press, 1998. ISBN: 0125444206.

- [58] Hisayasu Morino, Takeo Maruyama, and Koichi Iiyama. “Reduction of Wavelength Dependence of Coupling Characteristics Using Si Optical Waveguide Curved Directional Coupler”. In: *Journal of Lightwave Technology* 32.12 (June 2014), pp. 2188–2192. ISSN: 0733-8724. DOI: 10.1109/JLT.2014.2321660. URL: <http://ieeexplore.ieee.org/document/6809837/>.
- [59] Ramesh K. Gupta, Sujith Chandran, and Bijoy Krishna Das. “Wavelength-Independent Directional Couplers for Integrated Silicon Photonics”. In: *Journal of Lightwave Technology* 35.22 (2017), pp. 4916–4923. ISSN: 0733-8724. DOI: 10.1109/JLT.2017.2759162. URL: <http://ieeexplore.ieee.org/document/8055627/>.
- [60] D. T. Pierce and W. E. Spicer. “Electronic Structure of Amorphous Si from Photoemission and Optical Studies”. In: *Physical Review B* 5.8 (1972), pp. 3017–3029. ISSN: 0556-2805. DOI: 10.1103/PhysRevB.5.3017. URL: <https://link.aps.org/doi/10.1103/PhysRevB.5.3017>.
- [61] I-Wei Hsieh et al. “Cross-phase modulation-induced spectral and temporal effects on co-propagating femtosecond pulses in silicon photonic wires”. In: *Optics Express* 15.3 (2007), p. 1135. ISSN: 1094-4087. DOI: 10.1364/OE.15.001135. URL: <https://opg.optica.org/oe/abstract.cfm?uri=oe-15-3-1135>.
- [62] W. Bogaerts et al. “Silicon microring resonators”. In: *Laser & Photonics Reviews* 6.1 (Jan. 2012), pp. 47–73. ISSN: 18638880. DOI: 10.1002/lpor.201100017. URL: <https://onlinelibrary.wiley.com/doi/10.1002/lpor.201100017>.
- [63] Brent E. Little, Juha-Pekka Laine, and Sai T. Chu. “Surface-roughness-induced contradi-rectional coupling in ring and disk resonators”. In: *Optics Letters* 22.1 (1997), p. 4. ISSN: 0146-9592. DOI: 10.1364/OL.22.000004. URL: <https://opg.optica.org/abstract.cfm?URI=ol-22-1-4>.
- [64] T. J. Kippenberg, S. M. Spillane, and K. J. Vahala. “Modal coupling in traveling-wave resonators”. In: *Optics Letters* 27.19 (2002), p. 1669. ISSN: 0146-9592. DOI: 10.1364/OL.27.001669. URL: <https://opg.optica.org/abstract.cfm?URI=ol-27-19-1669>.
- [65] Miloš Popovic, Christina Manolatou, and Michael Watts. “Coupling-induced resonance frequency shifts in coupled dielectric multi-cavity filters”. In: *Optics Express* 14.3 (2006), p. 1208. ISSN: 1094-4087. DOI: 10.1364/OE.14.001208. URL: <https://opg.optica.org/oe/abstract.cfm?uri=oe-14-3-1208>.

